



Discrete Element Modelling of Railway Ballast

by

Mingfei Lu,

BEng., MSc. (Distinction)

*Thesis submitted to the University of Nottingham for
the degree of Doctor of Philosophy*

September 2008

To my parents

ABSTRACT

Discrete element modelling has been used to capture the essential mechanical features of railway ballast and gain a better understanding of the mechanical behaviour and mechanisms of degradation under monotonic and cyclic loading.

A simple procedure has been developed to generate clumps which resemble real ballast particles. The influence of clump shape on the heterogeneous stresses within an aggregate was investigated in box test simulations. More angular clumps lead to greater homogeneity and the interlocking provides a much more realistic load-deformation response. A simple two-ball clump was used with two additional small balls (asperities) bonded at the surface, to represent a single particle; it is shown that particle abrasion gives the correct settlement response.

A clump formed from ten balls in a tetrahedral shape was used in monotonic and cyclic triaxial test simulations and found to produce the correct response. The interlocking and breaking of very small asperities which find their way into the voids and carry no load was modelled using weak parallel bonds. The interlocking and fracture of larger asperities was modelled by bonding eight small balls to the ten-ball clump. Monotonic tests were performed on triaxial samples under different confining pressures and the results compared with existing experimental data. Tests were also simulated using uncrushable clumps to highlight the important role of asperity abrasion. Cyclic triaxial tests were then simulated on the same aggregates under a range of stress conditions and the results compared to existing experimental data for the same simulated ballast.

The clumps are able to capture the behaviour of ballast under different conditions, and asperity abrasion plays an important role in governing strength and volumetric strain under monotonic loading, and on permanent strains under cyclic loading. The contribution of this thesis is therefore to show that it is possible to model a real granular material under static and cyclic conditions, providing much micro mechanical insight.

ACKNOWLEDGEMENTS

This study would not have been completed without the help from many people. First and foremost, I would like to sincerely thank my supervisor, Professor Glenn McDowell, for his expert supervision, encouragement, patience and advice throughout this research project.

I would also like to thank everyone in the School of Civil Engineering. Special thanks are given to Dr. Wee Loon Lim, Dr. Jean-francois Ferellec, Dr. Xia Li and Dr. Bih Ling Lim who kindly spent hours proof-reading my thesis and gave me valuable comments.

In addition, I would like to acknowledge the financial support of the Rail Research UK (RRUK).

Finally, I would like to thank my parents and Xiumei Liang for their constant support, belief and encouragement.

TABLE OF CONTENTS

ABSTRACT I

ACKNOWLEDGEMENTS II

TABLE OF CONTENTS III

LIST OF FIGURES IX

LIST OF TABLES XXII

NOTATION XXIV

CHAPTER 1 INTRODUCTION 1

1.1 Background and Problem Definition 1

1.2 Aims and Objectives 3

1.3 Thesis Outline 4

CHAPTER 2 LITERATURE REVIEW: MECHANICAL BEHAVIOUR OF RAILWAY BALLAST 6

2.1	Introduction.....	6
2.2	Track Components and Ballast Functions	6
2.3	Track Forces	9
2.3.1	Vertical forces.....	9
2.3.2	Lateral forces	10
2.3.3	Longitudinal forces.....	11
2.4	Ballast Characteristics	11
2.4.1	Durability.....	12
2.4.2	Particle shape	13
2.4.3	Gradation	13
2.5	Mechanical Behaviour of Railway Ballast under Static Loading.....	15
2.5.1	Micromechanics of deformation during loading	15
2.5.2	Factors controlling stress-strain behaviour of granular material ...	16
2.6	Mechanical Behaviour of Railway Ballast under Repeated Loading.....	22
2.6.1	Shakedown theory	24
2.6.2	The cyclic triaxial test and the box test	26
2.6.3	Factors affecting resilient response	28
2.6.4	Factors affecting permanent strain response.....	31
2.7	Degradation of Granular Materials.....	35
2.7.1	Description of particle breakage.....	36
2.7.2	Single particle under compression.....	37

2.7.3	Factors affecting particle degradation	38
2.7.4	Ballast degradation under cyclic loading.....	40
2.8	Summary.....	43

CHAPTER 3 LITERATURE REVIEW: DISCRETE ELEMENT MODELLING OF GRANULAR MATERIAL 46

3.1	Introduction.....	46
3.2	Introduction to the Discrete Element Method and PFC ^{3D}	48
3.2.1	The discrete element method	48
3.2.2	The PFC ^{3D} Particle-Flow Model	49
3.2.3	Calculation cycle	51
3.2.4	Contact constitutive model	55
3.2.5	Clump logic	59
3.3	Influence of Particle Geometry in DEM.....	62
3.3.1	Restrain the rotation of individual particles	63
3.3.2	Using non-circular/spherical particles	65
3.4	Influence of Interparticle Friction Angle	71
3.5	Modelling of Particle Breakage	72
3.6	Modelling Mechanical Response of Railway Ballast Using DEM	74
3.7	Summary.....	78

CHAPTER 4 IMPORTANCE OF MODELLING BALLAST PARTICLE SHAPE..... 80

4.1	Introduction.....	80
4.2	Modelling Ballast Particle Shape.....	81
4.2.1	Modelling procedure.....	81
4.2.2	Results	87
4.3	Box Test Simulations Using Unbreakable Irregular Shaped Particles	91
4.3.1	Modelling procedure.....	91
4.3.2	Effect of particle shape on mechanical response.....	95
4.4	Conclusions	104

CHAPTER 5 DISCRETE ELEMENT MODELLING OF BALLAST ABRASION IN THE BOX TEST • 107

5.1	Introduction.....	107
5.2	Modelling Procedure	109
5.3	Effect of Particle Abrasion on Mechanical Response	112
5.4	Conclusions	118

CHAPTER 6 MONOTONIC TRIAXIAL TEST SIMULATIONS 120

6.1	Introduction.....	120
6.2	Modelling Procedure	123

6.3	Selecting Particle Shape	127
6.4	Modelling Particle Abrasion	132
6.4.1	Parallel bond contact law between clumps	132
6.4.2	Using asperities	139
6.5	Modelling Railway Ballast Behaviour under a Large Range of Confining Pressures	143
6.5.1	Axial and volumetric strain	144
6.5.2	Number of contacts	148
6.6	Conclusions	150

CHAPTER 7 CYCLIC TRIAXIAL TEST SIMULATIONS 151

7.1	Introduction	151
7.2	Modelling Procedure	152
7.3	Effect of Particle Abrasion under Cyclic Loading	156
7.4	Modelling Railway Ballast Behaviour under a Large Range of Confining Pressures	164
7.4.1	Axial and volumetric strain	164
7.4.2	Strain behaviour as a function of ψ	176
7.4.3	Number of contacts	177
7.4.4	Cyclic degradation behaviour	180
7.5	Effect of Parallel Bond between Clumps	188
7.6	Conclusions	192

CHAPTER 8 CONCLUSIONS AND SUGGESTIONS FOR FURTHER RESEARCH.....	194
8.1 Conclusions	194
8.2 Suggestions for Further Research	197
REFERENCES.....	199
APPENDIX.....	216

LIST OF FIGURES

Figure 1.1. Contributions to settlement in rail track (Selig and Waters, 1994)	·1
Figure 2.1. Track layout of a typical ballasted track – side view (Selig and Waters, 1994)	8
Figure 2.2. Track layout of a typical ballasted track – cross section (Selig and Waters, 1994)	8
Figure 2.3. Static and dynamic wheel loads for (a) Colorado test track and (b) mainline track between New York and Washington (Selig and Waters, 1994)	10
Figure 2.4. Pressure distribution (Shenton, 1974)	10
Figure 2.5. A simplified representation of form, roundness and surface texture by three linear dimensions to illustrate their independence (Barrett, 1980)	14
Figure 2.6. A particle outline (heavy solid line) with its component elements of form (light solid lines, two approximations shown), roundness (dashed circles) and texture (dotted circles) identified (Barrett, 1980)	14

Figure 2.7. Large-scale triaxial equipment: (a) schematic view of test frame with triaxial chamber and (b) detailed components of triaxial chamber (Indraratna <i>et al.</i> , 1998)	17
Figure 2.8. Experiment results of drained compression tests on ballast under different confining pressures (contraction positive) (Indraratna <i>et al.</i> , 1998).....	18
Figure 2.9. Influence of confining pressure on peak principal stress ratio for basalt in comparison with various granular media (Indraratna <i>et al.</i> , 1998).....	19
Figure 2.10. Mohr-Coulomb failure envelopes for Latite Ballast (Indraratna <i>et al.</i> , 1998).....	19
Figure 2.11. Influence of confining pressure on the peak angle of internal friction of Basalt at low to medium confining pressures (Indraratna <i>et al.</i> , 1998).....	20
Figure 2.12. Effect of particle characteristics on (a) peak internal friction angle and (b) deviator stress at failure (Selig and Waters, 1994).....	21
Figure 2.13. Ballast behaviour in the cyclic triaxial test (Selig and Waters, 1994)	23
Figure 2.14. Strains in granular materials during one cycle of load application (Lekarp <i>et al.</i> , 2000a).....	24
Figure 2.15. Four types of response of an elastic-plastic structure to repeated loading (Collins and Boulbibane, 2000).....	25
Figure 2.16. Plan of rail and sleepers showing section represented by the box test (Lim, 2004)	27

Figure 2.17. Box test set-up: (a) view from the top of the box and (b) front view (Lim, 2004)	27
Figure 2.18. Resilient modulus M_R response under various stress states after 500,000 cycles (Lackenby <i>et al.</i> , 2007)	29
Figure 2.19. Resilient modulus M_R response under various stress states: (a) effect of confining pressure σ'_3 and number of cycles N on M_R for $q_{max,cyc} = 500$ kPa and (b) effect of $q_{max,cyc}$ M_R for on $\sigma'_3 = 60$ and 240 kPa (Lackenby <i>et al.</i> , 2007)	30
Figure 2.20. Strain response under cyclic loading: (a) axial strain ε_a as a function of the number of cycles N ; (b) volumetric strain ε_v as a function of N ; (c) final ε_a after 500,000 cycles and (d) final ε_v after 500,000 cycles (Lackenby <i>et al.</i> , 2007)	32
Figure 2.21. Effect of loading frequency (Shenton, 1974)	34
Figure 2.22. Permanent deformation as a linear function of logarithm of number of load cycle (Shenton, 1974)	34
Figure 2.23. Effect of difference in sequence of loading on permanent strain (Selig and Waters, 1994)	36
Figure 2.24. Ballast breakage index (Indraratna <i>et al.</i> , 2005)	41
Figure 2.25. Effect of confining pressure σ'_3 and maximum deviator stress $q_{max,cyc}$ on ballast breakage index BBI, and effect of $q_{max,cyc}$ on DUDZ, ODZ and CSDZ breakage zones (Lackenby <i>et al.</i> , 2007)	42
Figure 3.1. Calculation cycle use in PFC ^{3D} (Itasca, 1999)	51

Figure 3.2. Constitutive behaviour for contact occurring at a point (Itasca, 1999).....	58
Figure 3.3. Parallel bond depicted as a cylinder of cementitious material (Itasca, 1999)	59
Figure 3.4. Contact model in MDEM (Iwashita and Oda, 1998).....	64
Figure 3.5. Effect of particle rolling resistance on stress-strain behaviour and volumetric change (contraction positive) (Iwashita and Oda, 1998)	64
Figure 3.6. Interparticle friction angle ϕ'_μ against friction angle ϕ' and dilatancy angle ψ at steady-state collapse (at deviator strain = 0.05) (Suiker and Fleck, 2004).....	65
Figure 3.7. Stress-strain behaviour during biaxial compression (Rothenburg and Bathurst, 1992).....	67
Figure 3.8. Coordination number plotted against shear strain (Rothenburg and Bathurst, 1992)	68
Figure 3.9. The position of the four spheres in the cluster (Vu-Quoc <i>et al.</i> , 2000).	68
Figure 3.10. (a) Stress-strain response and (b) average particle rotation in biaxial shear tests (Thomas and Bray, 1999).....	69
Figure 3.11. Axisymmetric sphere clusters (O'Sullivan and Bray, 2003)	70
Figure 3.12. Schematic illustration of a bonded particle. The diameter of the parallel bond is the same as the diameter of the smaller sphere (Powrie <i>et al.</i> , 2005)	70

Figure 3.13. Interparticle friction angle ϕ'_μ versus internal friction angle ϕ' for DEM and experimental results (Suiker and Fleck, 2004).....	72
Figure 3.14. Final fracture of a typical 0.5 mm diameter agglomerate, showing intact contact bonds (McDowell and Harireche, 2002a)	74
Figure 3.15. Idealisation of the induced tensile stress and arrangement of the produced fragments (Lobo-Guerrero and Vallejo, 2005).....	75
Figure 3.16. Details of the unloaded sample of crushable ballast after 200 cycles (Lobo-Guerrero and Vallejo, 2006).....	77
Figure 4.1. Typical full-sized ballast particle.....	82
Figure 4.2. Directions of ball generation for clumps	84
Figure 4.3. Ball generation along one direction.....	84
Figure 4.4. Definition of clump geometry	85
Figure 4.5. Effect of angle α on clump geometry	86
Figure 4.6. Formation of edge of clump	87
Figure 4.7. Typical clumps generated for Sample 4.1 (refer to Table 4.1 for parameters)	88
Figure 4.8. Typical clumps generated for Sample 4.2 (refer to Table 4.1 for parameters)	89
Figure 4.9. Typical clumps generated for Sample 4.3 (refer to Table 4.1 for parameters)	89
Figure 4.10. Typical clumps generated for Sample 4.4 (refer to Table 4.1 for parameters)	90
Figure 4.11. Typical clumps generated for Sample 4.5 (refer to Table 4.1 for parameters)	90

Figure 4.12. Box test on (a) spheres, (b) Sample 4.1 and (c) Sample 4.2.....92

Figure 4.13. Contact forces for (a) spheres, (b) Sample 4.1 and (c) Sample 4.2
prior to loading96

Figure 4.14. Contact forces for spheres (a) prior to loading (maximum contact
force = 482N, average contact force = 29.9N, number of contacts =
10,337); (b) at maximum load (maximum contact force = 4,050N,
average contact force = 336.2N, number of contacts = 10,323) and
(c) after unloading to 3kN (maximum contact force = 1,012N,
average contact force = 42.7N, number of contacts = 10,328).....97

Figure 4.15. Contact forces for Sample 4.1 (a) prior to loading (maximum
contact force = 374N, average contact force = 15.4N, number of
contacts = 282,955); (b) at maximum load (maximum contact force
= 4,233N, average contact force = 164.1N, number of contacts =
282,955) and (c) after unloading to 3kN (maximum contact force =
1,354N, average contact force = 34.4N, number of contacts =
282,955)98

Figure 4.16. Rotations of spheres (a) during loading (maximum rotation =
48.3°, average rotation = 5.18°; (b) during unloading (maximum
rotation = 26.5°, average rotation = 2.92°) and (c) after the
complete cycle of loading and unloading (maximum rotation =
63.2°, average rotation = 7.25°) 100

Figure 4.17. Rotations of clumps in Sample 4.1 (a) during loading (maximum
rotation = 8.89°, average rotation = 0.061°); (b) during unloading

(maximum rotation = 3.15° , average rotation = 0.033°) and (c)	
after the complete cycle of loading and unloading (maximum	
rotation = 3.31° , average rotation = 0.062°)	101
Figure 4.18. Total displacements of spheres (a) at maximum load (maximum	
displacement = 8.25mm) and (b) after one cycle of loading and	
unloading (maximum displacement = 11.79mm)	103
Figure 4.19. Total displacements for clumps in Sample 4.1 (a) at maximum load	
(maximum displacement = 2.34mm) and (b) after one cycle of	
loading and unloading (maximum displacement = 2.32mm)	104
Figure 4.20. Displacement vectors of (a) Figure 4.19(a) and (b) Figure 4.19(b)	
magnified by a factor of 80	105
Figure 4.21. Cyclic response for spheres and Sample 4.1	106
Figure 5.1. (a) Settlement and (b) stiffness plotted against number of cycles for	
traffic-only box test and standard box test (tamping and traffic	
loading) on wet ballast (McDowell <i>et al.</i> , 2005)	108
Figure 5.2. (a) Three-dimensional particle comprising two-ball clump and two	
asperities; (b) clump and asperity dimensions and (c) aggregate of	
particles prior to cyclic loading	110
Figure 5.3. Displacement of bottom of sleeper during 20 load cycles for (a)	
Simulation 5.1; (b) Simulation 5.2 and (c) Simulation 5.3	114
Figure 5.4. Number of broken bonds during 20 load cycles	115
Figure 5.5. Settlement plotted against number of load cycles for all three	
simulations plotted on (a) linear scale and (b) logarithmic scale	115

Figure 5.6.	Stiffness plotted against number of load cycles for all three simulations	117
Figure 5.7.	(a) Typical contact force distribution during cyclic loading in Simulation 5.3 and (b) locations of where asperities break during 20 load cycles in Simulation 5.3	118
Figure 6.1.	Experiment results of drained compression tests on ballast under different confining pressures (Indraratna <i>et al.</i> , 1998)	122
Figure 6.2.	PFC ^{3D} model (a) triaxial cell; (b) single sphere as a ballast particle; (c) eight-ball cubic clump as a ballast particle; (d) ten-ball triangular clump as a ballast particle and (e) ten-ball triangular clump with eight small balls (asperities) bonded as a ballast particle	126
Figure 6.3.	Results of triaxial simulations on both loose and dense samples for spheres, eight-ball cubic clumps and ten-ball triangular clumps under a confining pressure of 120 kPa	128
Figure 6.4.	Effect of friction coefficient on (a) shear strength and (b) volumetric strain (contraction positive) for dense sample of ten-ball triangular clumps	130
Figure 6.5.	Effect of friction coefficient on (a) shear strength and (b) volumetric strain (contraction positive) for loose sample of ten-ball triangular clumps	131
Figure 6.6.	Effect of increasing parallel bond strength and stiffness between clumps on (a) shear strength and (b) volumetric strain (contraction positive)	135

Figure 6.7. Effect of increasing parallel bond strength and stiffness between clumps on average coordination number of clumps	136
Figure 6.8. Effect of increasing the ratio of shear parallel bond strength and stiffness to normal parallel bond strength and stiffness between clumps on (a) shear strength and (b) volumetric strain (contraction positive)	138
Figure 6.9. Effect of increasing the ratio of shear parallel bond strength and stiffness to normal parallel bond strength and stiffness between clumps on average coordination number of clumps	139
Figure 6.10. Effect of increasing bond strength and stiffness between clump and asperity on (a) shear strength and (b) volumetric strain (contraction positive)	142
Figure 6.11. Number of asperities broken off during monotonic loading	143
Figure 6.12. Locations of broken bonds between clumps and asperities during monotonic loading in Simulation 6.11	143
Figure 6.13. Results of deviator stress against axial strain under a range of confining pressures (a) using ten-ball triangular clumps bonded with eight small balls as asperities; (b) using ten-ball triangular clumps with eight small balls (unbreakable asperities) and (c) experimental results (Indraratna <i>et al.</i> , 1998)	146
Figure 6.14. Results of volumetric strain against axial strain under a range of confining pressures (a) using ten-ball triangular clumps bonded with eight small balls as asperities; (b) using ten-ball triangular	

clumps with eight small balls (unbreakable asperities) and (c)	
experimental results (Indraratna <i>et al.</i> , 1998).....	147
Figure 6.15. Number of asperities broken off during monotonic loading under a	
range of confining pressures against (a) axial strain and (b)	
volumetric strain	148
Figure 6.16. Number of contacts prior to shearing and after shearing for the	
breakable and unbreakable assemblies	149
Figure 7.1. Assembly of ten-ball triangular clumps with eight small balls	
(asperities) bonded in the triaxial cell.....	153
Figure 7.2. (a) Axial strain and (b) volumetric strain (contraction positive)	
under a confining pressure of 120 kPa against number of cycles	
(Lackenby <i>et al.</i> , 2007).....	157
Figure 7.3. (a) Axial strain and (b) volumetric strain (contraction positive)	
under a confining pressure of 120 kPa during the first 1,000 cycles	
(Lackenby <i>et al.</i> , 2007).....	158
Figure 7.4. (a) Axial strain and (b) volumetric strain (contraction positive) for	
both breakable and unbreakable assemblies under a confining	
pressure of 120 kPa against number of cycles.....	159
Figure 7.5. Number of asperities broken off under a confining pressure of 120	
kPa against number of cycles	160
Figure 7.6. (a) Axial strain and (b) volumetric strain (contraction positive)	
after 100 cycles for simulations and experimental tests, and after	
500,000 cycles for experimental tests.....	163

Figure 7.7. Axial strain as a function of the number of cycles (Lackenby <i>et al.</i> , 2007).....	165
Figure 7.8. Volumetric strain (contraction positive) as a function of the number of cycles (Lackenby <i>et al.</i> , 2007)	166
Figure 7.9. Axial strain during the first 1,000 cycles (Lackenby <i>et al.</i> , 2007)	167
Figure 7.10. Volumetric strain (contraction positive) during the first 1,000 cycles (Lackenby <i>et al.</i> , 2007).....	168
Figure 7.11. Axial strain as a function of the number of cycles for the simulations.....	169
Figure 7.12. Volumetric strain (contraction positive) as a function of the number of cycles for the simulations.....	170
Figure 7.13. Number of asperities broken off against number of cycles	171
Figure 7.14. Axial strain against confining pressure: (a) experimental results at 500,000 loading cycles (Lackenby <i>et al.</i> , 2007); (b) experimental results at 100 loading cycles (Lackenby <i>et al.</i> , 2007) and (c) simulation results	173
Figure 7.15. Volumetric strain (contraction positive) against confining pressure: (a) experimental results at 500,000 loading cycles (Lackenby <i>et al.</i> , 2007); (b) experimental results at 100 loading cycles (Lackenby <i>et al.</i> , 2007) and (c) simulation results	174
Figure 7.16. Axial strain against the ratio of maximum deviator stress under cyclic loading to maximum deviator stress under monotonic loading (a) experimental results at 500,000 loading cycles	

(Lackenby <i>et al.</i> , 2007); (b) experimental results at 100 loading cycles (Lackenby <i>et al.</i> , 2007) and (c) simulation results	178
Figure 7.17. Number of contacts for both cyclic and monotonic triaxial test simulations	179
Figure 7.18. Effect of confining pressure and maximum deviator stress on ballast breakage index (Lackenby <i>et al.</i> , 2007)	180
Figure 7.19. Number of broken asperities against confining pressure	181
Figure 7.20. Number of broken parallel bonds between clumps against confining pressure	181
Figure 7.21. Number of broken asperities under a confining pressure of 10 kPa against axial strain	185
Figure 7.22. Number of broken asperities under a confining pressure of 30 kPa against axial strain	185
Figure 7.23. Number of broken asperities under a confining pressure of 60 kPa against axial strain	185
Figure 7.24. Number of broken asperities under a confining pressure of 120 kPa against axial strain	186
Figure 7.25. Number of broken asperities under a confining pressure of 240 kPa against axial strain	186
Figure 7.26. Number of broken asperities under confining pressures of 10 kPa to 240 kPa against axial strain	187
Figure 7.27. 3D plot showing the relationship between confining pressure, axial strain and number of broken asperities	187

Figure 7.28. (a) Axial strain and (b) volumetric strain (contraction positive) against number of cycles	189
Figure 7.29. Number of broken parallel bonds between clumps against number of cycles	190
Figure 7.30. Number of broken asperities against number of cycles	190
Figure 7.31. Number of broken parallel bonds between clumps against axial strain	191

LIST OF TABLES

Table 2.1 Particle size distribution specification (RT/CE/S/006 Issue 3, 2000) ..	
.....	15
Table 4.1. Parameters for clumps in different sample	88
Table 6.1. Number of particles, sizes of the particles and porosity of the	
samples	124
Table 6.2. Parameters of parallel bonds between clumps used in the series of	
simulations to investigate the effect of increasing bond strengths and	
stiffnesses for parallel bonds between clumps.....	134
Table 6.3. Parameters of parallel bonds between clumps used in the series of	
simulations to investigate the effect of increasing ratio of shear to	
normal bond strength and stiffness for parallel bonds between	
clumps.....	137
Table 6.4. Parameters for parallel bonds and contact bonds used to bond	
asperities with clumps used in the series of simulations to investigate	
the effect particle abrasion.....	141
Table 7.1. Parameters for parallel bonds and contact bonds used to bond	
asperities with clumps used in the simulations.....	153

Table 7.2. Parameters for parallel bonds between clumps used in the simulations	153
Table 7.3. List of cyclic triaxial test simulations in Series 7.1	155
Table 7.4. List of cyclic triaxial test simulations in Series 7.2	156
Table 7.5. Parameters for parallel bonds between clumps used in the simulations in Series 7.3	156
Table 7.6. Regression coefficients for Equation 7.1 (Lackenby <i>et al.</i> , 2007) ·	175
Table 7.7. Upper limits of confining pressure for DUDZ and ODZ (Lackenby <i>et al.</i> , 2007).....	182
Table 7.8. Regression coefficients for Equation 7.3	184

NOTATION

BBI	Ballast breakage index
CSDZ	Compressive stable degradation zone
c	Maximum reduction of radius in each direction
DEM	Discrete Element Method
D_{ekv}	Equivalent or average particle size
DUDZ	Dilatant unstable degradation zone
d	Diameter of a grain.
e	Eccentricity
F_f	Diametral force at failure
G	Gain factor
K	Resilient stiffness
LAA	Los Angeles abrasion
MA	Mill abrasion
MDA	Micro-Deval attrition
MDEM	Modified discrete element method
M_R	Resilient modulus
m	Weibull modulus
N	Number of loading cycles

N_{asp}	Number of broken asperities
ODZ	Optimum degradation zone
PFC ^{3D}	Particle Flow Code in 3 Dimensions
p	Probability of the number of directions of ball generation used
q	Deviator stress
$q_{max,cyc}$	Maximum deviator stress for cyclic loading
$q_{peak,sta}$	Peak strength obtained from monotonic triaxial test
R	Radius of ball
R_v	Radius of virtual sphere
V_{clump}	Volume of clump
ε_a	Axial strain
ε_v	Volumetric strain
μ	Friction coefficient
ρ_m	Modified density
ρ_0	Initial density
σ_{av}	Mean tensile strength
σ_f	Tensile stress at failure
σ'_c	Confining pressure
σ'_1	Major principal effective stress
σ'_3	Minor principal effective stress
φ'	Friction angle
φ'_μ	Interparticle friction angle
φ'_{peak}	Peak internal friction angle

ψ Ratio of maximum deviator stress for cyclic loading to the peak strength obtained from monotonic triaxial tests

ψ_d Dilatancy angle

CHAPTER 1

INTRODUCTION

1.1 Background and Problem Definition

Railways play an important role in the worldwide transportation system. Every year a large amount of money is spent on track maintenance. With growing demand for high speed trains and heavy freight movement, deterioration of the track geometry has been recognised as the main cause of the need for track maintenance. According to Selig and Waters (1994), ballast is one of the main sources of track geometry deterioration as shown in Figure 1.1.

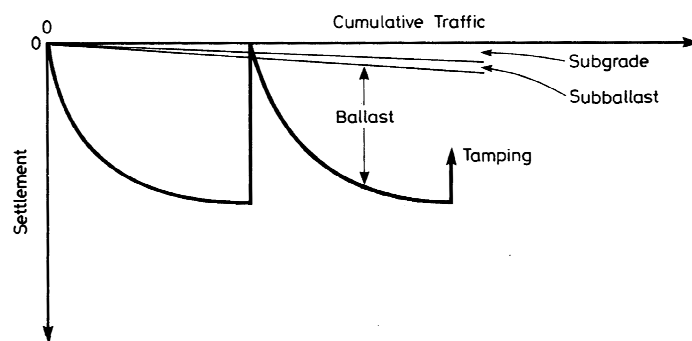


Figure 1.1. Contributions to settlement in rail track (Selig and Waters, 1994).

Railway ballast generally comprises large, angular particles of typical size approximately 40 mm. The main functions of railway ballast are to reduce pressures from the sleeper bearing area to acceptable levels at the surface of the subgrade soil, to facilitate maintenance operations for the re-establishment of track riding quality, and to provide rapid drainage (Selig and Waters, 1994). Ballast functions deteriorate through the actions of traffic loading and maintenance tamping. The angularity (sharp corners) of ballast leads to stress concentrations and breakage, but is necessary for good shearing resistance. Traffic loading is one of the main causes of ballast degradation. Over the years, many researchers have studied the complex behaviour of ballast using laboratory and in-situ test techniques. However, due to the limitations of the physical tests to accurately monitor the ballast response at a particle level, the true nature of the deformation and mechanism of degradation has not yet been fully understood.

The discrete element method (DEM) (Cundall and Strack, 1979) provides a way to investigate the mechanical behaviour of granular material at both micro and macro level. In DEM, finite displacements and rotations of discrete bodies are allowed and new contacts can be recognised automatically during the calculation process. It enables investigation of the micro mechanics of the deformation of granular materials that cannot be easily studied in laboratory tests. DEM has been used to investigate the mechanical behaviour of granular material over the past three decades; details will be described in the literature review. In recent years, it has also been used to model particle crushing (also discussed in the literature review). Thus, it provides a powerful numerical tool for modelling the mechanical

behaviour of railway ballast and for studying the micro mechanical behaviour of railway ballast and the mechanisms of particle degradation.

1.2 Aims and Objectives

The ultimate goal of this project is to gain a better understanding of the mechanical behaviour of railway ballast at particle level by using the discrete element method.

The aims of this project can be stated as:

- To develop a suitable particle model in PFC^{3D}, so that the mechanical response of ballast under different loading condition can be modelled.
- To model box tests and both monotonic and cyclic triaxial tests to gain a better understanding of ballast mechanics.
- To study the effect of ballast degradation on the performance of ballast under different loading conditions.

To achieve these aims, the following specific objectives are required:

1. Selection of a particle shape that effectively captures the main mechanical features of real ballast (e.g. stress-strain response, volumetric behaviour, permanent deformation and particle degradation).
2. Modelling of the mechanism of particle abrasion.
3. Simulations of box tests and both monotonic and cyclic triaxial tests.
4. Comparison of simulation results with experimental data.

5. Comparison of the simulation results using breakable assemblies and unbreakable assemblies to study the effect of degradation of railway ballast on macroscopic behaviour.

1.3 Thesis Outline

This thesis is divided into eight chapters. A brief outline of this thesis is given below.

Chapter 2 contains a literature review of the mechanical behaviour of railway ballast. A description of the track components, ballast functions, forces generated on the ballast layer, and ballast characteristics are presented. The mechanical behaviour of railway ballast under both static and repeated loading and the factors influencing the behaviour are then discussed. A review of degradation of granular materials is also presented in section 2.2.

Chapter 3 contains a literature review of DEM and PFC^{3D} used in the modelling of granular materials. The effects of particle shape and interparticle friction on the mechanical behaviour of granular material are discussed and methods used to model the particle shape and particle breakage are presented. Recent applications of PFC in the modelling mechanical response of railway ballast are reviewed.

In Chapter 4, a simple procedure to generate clumps which resemble real ballast particles is introduced and a procedure for the box test simulation is described. The effect of particle shape on behaviour is investigated in box test simulations by using both spheres and clumps.

In Chapter 5, a simple particle model to simulate particle abrasion is described. The effect of particle abrasion under cyclic loading is investigated in the box test simulations.

Chapter 6 presents monotonic triaxial test simulations. Different scales of particle abrasion are simulated. Parallel bonds are introduced between clumps to simulate the interlocking of very small asperities and small balls are bonded at the corners to model relatively larger asperities. The effects of particle shape, particle friction, and particle abrasion on the behaviour of railway ballast are investigated. The behaviour of the assembly for the developed particle model under a range of confining pressures is then compared with experimental data.

Chapter 7 presents cyclic triaxial test simulations. The assemblies of particles developed in Chapter 6 are used. The effect of particle abrasion under cyclic loading is investigated in the cyclic triaxial test simulations. Simulation results under different cyclic loading conditions are compared with experimental results. The effect of particle abrasion on permanent strain and degradation is investigated and presented.

Chapter 8 summarises the major contributions of this research and presents suggestions for future research.

CHAPTER 2

LITERATURE REVIEW: MECHANICAL BEHAVIOUR OF RAILWAY BALLAST

2.1 Introduction

A large amount of money is spent on the maintenance of the railway track every year. Railway track maintenance arises mainly from the degradation of ballast and the deterioration of the track geometry (Selig and Waters, 1994). In order to minimise maintenance costs, a proper understanding of how ballast performs under traffic loading is imperative. In this chapter, an introduction of track components, ballast functions, and track forces will first be presented, followed by ballast characteristics. A literature review of recent studies of the mechanical behaviour of railway ballast under both static loading and repeated loading is presented. Finally, a review of the degradation of granular materials is presented.

2.2 Track Components and Ballast Functions

Generally, ballasted track structures can be grouped into two main components: the superstructure and substructure. The superstructure consists of the rails, the fastening system and the sleepers, while the substructure consists of the ballast, the

subballast and the subgrade. Figures 2.1 and 2.2 show the components of a typical ballasted track. Railway ballast is a crushed granular material placed as the top layer of the substructure where the sleepers are embedded. Ideal ballast materials are angular, crushed, hard stones and rocks, uniformly graded, free of dust and dirt, and not prone to cementing action (Selig and Waters, 1994). However, due to the lack of universal agreement concerning the proper specifications for the ballast material index characteristics, availability and economic considerations have been the main factors considered in selection of ballast materials. Various materials have been used for ballast such as crushed granite, basalt, limestone, slag and gravel.

The ballast layer plays an important role in the rail track system. Main ballast functions were summarised by Selig and Waters (1994) as follows:

1. Retain the track in its required position by withstanding forces applied to the sleepers.
2. Provide the required degree of resiliency and energy absorption to the track.
3. Distribute stresses from the sleeper bearing area to acceptable stress levels for the subballast and subgrade, thereby limiting permanent settlement of the track.
4. Provide sufficient voids for storage of fouling material in the ballast, and movement of particles through the ballast.

5. Facilitate maintenance surfacing and lining operations (to adjust track geometry) by an ability to rearrange ballast particles with tamping.
6. Provide immediate drainage of water falling onto the track.

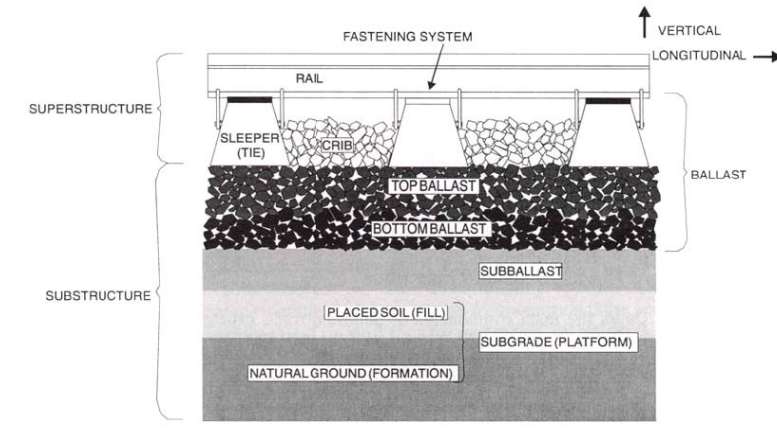


Figure 2.1. Track layout of a typical ballasted track – side view (Selig and Waters, 1994).

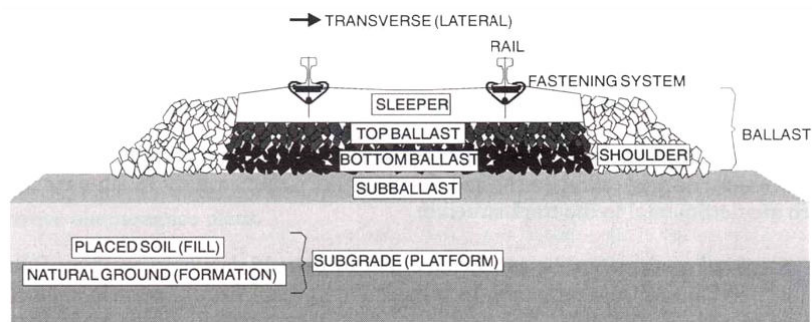


Figure 2.2. Track layout of a typical ballasted track – cross section (Selig and Waters, 1994).

2.3 Track Forces

Track forces imposed on ballast layer can be divided into vertical, lateral, and longitudinal components. Vertical forces are the main imposed forces on ballast, while, the lateral and longitudinal forces are much harder to predict (Selig and Waters, 1994).

2.3.1 Vertical forces

The vertical force is a combination of static load and dynamic load. The static load combines the dead weight of train and the weight of superstructure (i.e. the weight of the rails, the fastening system and the sleepers). Regarding the dynamic load, it depends on track, vehicle and train characteristics, operating conditions, and environmental conditions. Figure 2.3 shows static and dynamic wheel loads plotted in the form of cumulative frequency distribution curves. Field measurements carried out by Broadley *et al.* (1981) and Frederick and Round (1985) showed that the dynamic forces could increase the wheel load by a factor of three, depending on the different types of the rail track system.

The stress in the ballast layer due to the vertical force passing down from the sleeper has not yet been accurately determined. The reason for this is that the ballast layer consists of large particles and its behaviour is more like discrete than continuous (Shenton, 1974). Figures 2.4(a) and (b) show the pressure distribution along the sleeper bottom and vertical pressure of different levels in the ballast layer, respectively.

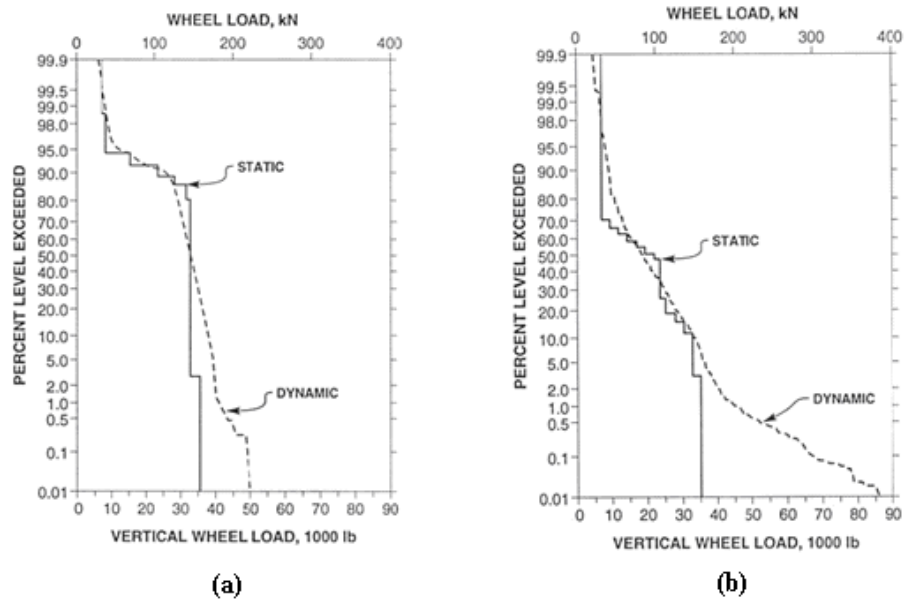


Figure 2.3. Static and dynamic wheel loads for (a) Colorado test track and (b) mainline track between New York and Washington (Selig and Waters, 1994).

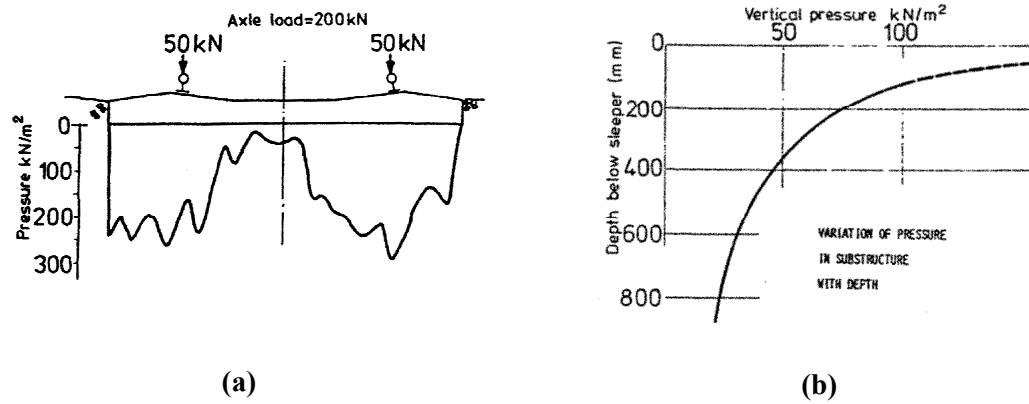


Figure 2.4. Pressure distribution (Shenton, 1974).

2.3.2 Lateral forces

The lateral force is the force that acts parallel to the long axis of the sleepers. The principal sources of this type of force are lateral wheel force and buckling reaction

force (Selig and Waters, 1994). The lateral wheel force arises from the train reaction to geometry deviations in self-excited hunting motions which result from bogie instability at high speeds, and centrifugal forces in curved tracks. The buckling reaction force arises from buckling of rails due to the high longitudinal rail compressive stress which results from rail temperature increase.

2.3.3 Longitudinal forces

The longitudinal forces are parallel to the rail. The sources of this force are: locomotive traction force including force required to accelerate the train and braking force and thermal expansion and contraction of rails (Selig and Waters, 1994).

2.4 Ballast Characteristics

The ability of ballast to perform its functions depends on the particle characteristics (e.g. particle size, shape, angularity, hardness, surface texture and durability) together with the in-situ physical state (e.g. grain structure and density). Selig and Waters (1994) pointed out that no single characteristic controls ballast behaviour and that the behaviour of ballast is the net effect of many combined characteristics. This section contains a presentation of the main ballast characteristics. Their effect on the behaviour of railway ballast under different loading conditions will be presented in the next few sections.

2.4.1 Durability

Durability tests have been developed to evaluate toughness of ballast particles or tendency for particle breakage. Granular materials consisting of weak grains should exhibit higher degrees of degradation, and hence, relatively more compressibility and lower shear strengths. Two abrasion tests (i.e. Los Angeles Abrasion (LAA) test and micro-Deval Attrition (MDA) test) are commonly used to evaluate the durability of ballast in railway engineering. The LAA test for railway ballast is carried out as specified in BS EN 13450 (2002). The LAA test involves rotation 5 kg of 31.5-40 mm and 5 kg of 40-50mm dry ballast with 10 spherical steel balls weighing 5.2 kg in a steel drum. The steel drum is rotated on a horizontal axis for 1000 revolutions. The tested ballast materials are sieved using a 1.6 mm sieve. The definition of the LAA is the percentage of the test portion passing a 1.6 mm sieve after the completion of the test. The LAA test measures the resistance of ballast to fragmentation. The MDA test is carried out as specified in BS EN 13450 (2002). The MDA test involves rotating two specimens of dry ballast materials in two separate steel drums. Each specimen consists of 5 kg of 31.5-40 mm and 5 kg of 40-50 mm particles. Two litres of water are added into each steel drum and the ballast specimen is rotated on a horizontal axis for 14,000 revolutions with a rotational speed of 100 rot/min. The tested ballast materials are sieved using a 1.6 mm sieve. The definition of the MDA is the percentage of the test portion passing a 1.6 mm sieve after the completion of the test. This test measures the resistance of ballast to wear.

2.4.2 Particle shape

Particle shape influences not only the physical state of the assembly (grain structure and porosity) but also the particle interaction (interparticle friction, contact force and coordination number). In the past, various attempts have been made to characterise particle shape of railway ballast. However, due to the complexity and irregularity of the shape of particle, universally accepted effective parameters on shape characteristic have not been established so far. In the railway industry, various shape characteristics (i.e. flakiness, elongation, sphericity, angularity and surface texture) are used.

Barrett (1980) reviewed various approaches to analyze particle shape in geology and sedimentology and expressed the shape of a particle in terms of three independent properties, namely: form (overall shape), roundness (large-scale smoothness) and surface texture, as shown in Figure 2.5. These three properties can be distinguished at least partly because of their different scales with respect to the particle, as shown in Figure 2.6. Form reflects variations in the particle scale, while roundness reflects variations at the corners. Surface texture is a property of particle surfaces between and at the corners.

2.4.3 Gradation

The selection of the particle size distribution of ballast layer has a great effect on both in-situ performance and the economic evaluation of track design. It is widely accepted that a narrow gradation would best meet the requirements for railway ballast. Sufficient voids are formed within the railway ballast with a narrow

gradation and, therefore, it provides efficient drainage of water from the ballast trackbed. The particle size distributions required in British railway ballast specification (RT/CE/S/006 issue 3, 2000) is shown in Table 2.1.

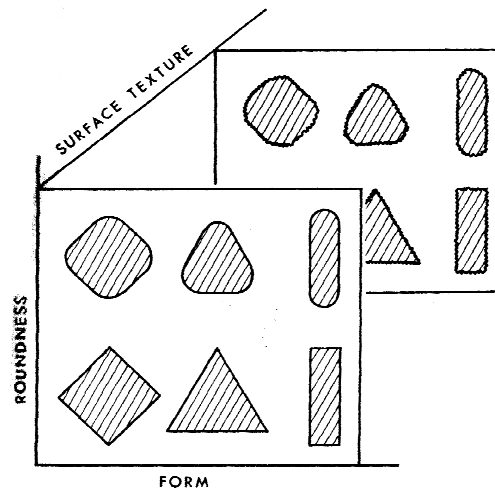


Figure 2.5. A simplified representation of form, roundness and surface texture by three linear dimensions to illustrate their independence (Barrett, 1980).

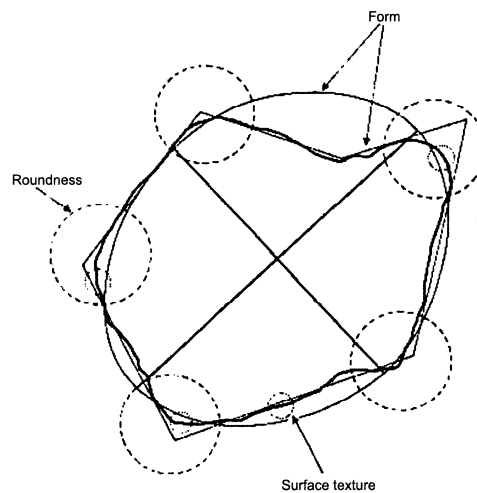


Figure 2.6. A particle outline (heavy solid line) with its component elements of form (light solid lines, two approximations shown), roundness (dashed circles) and texture (dotted circles) identified (Barrett, 1980).

Square Mesh Sieve (mm)	Cumulative % by mass passing BS sieve
63	100
50	70-100
40	30-65
31.5	0-25
22.4	0-3
32-50	≥ 50

Table 2.1. Particle size distribution specification (RT/CE/S/006 Issue 3, 2000).

2.5 Mechanical Behaviour of Railway Ballast under Static Loading

2.5.1 Micromechanics of deformation during loading

Ballast consists of grains in contact and surrounding voids. It is commonly known that the mechanical behaviour of ballast is inherently discontinuous and heterogeneous. Oda and Iwashita (1999) indicated that the behaviour of granular materials is determined not only by the arrangement of particles in space, but also by what kinds of interactions occur between them. Ballast, like other granular materials, shows complex elastic-plastic behaviour under loading and unloading. Many laboratory tests have been conducted to investigate the stress-strain behaviour of ballast. However, complete understanding of the micro mechanical response (at a particle level) has not been fully established.

Deformation under loading is normally a combination of the volumetric and shear at the macroscopic level, whereas, at the microscopic level, deformation is the

results of particle rearrangement and breakage. Luong (1982) postulated that the deformation of granular soils under loading is the result of three main mechanisms: consolidation, distortion, and attrition. The consolidation mechanism (densification or dilation) is the change in volume of particle assemblies; the distortion mechanism is the change in aggregate shape due to sliding and rolling; the attrition mechanism is particle crushing and breakage leading to rearrangement and compaction or dilation. The resistance to particle sliding and rolling depends on the interparticle friction of the granular material (Oda and Iwashita, 1999). Crushing is a progressive process that can start at relatively low stresses, and certainly dominates the behaviour of the assembly at very high effective stress. The details of particle crushing and degradation will be presented in the later section.

2.5.2 Factors controlling stress-strain behaviour of granular material

Due to the size of railway ballast particles, large-scale triaxial test equipment has been developed to investigate the mechanical behaviour. Monotonic triaxial tests are commonly used to investigate mechanical response of typical ballast under static loading conditions. Indraratna *et al.* (1998), for example, performed large-scale triaxial tests on latite basalt to study the stress-strain relationships, strength properties and degradation characteristics of railway ballast. Figure 2.7 shows the large-scale triaxial equipment used in their tests. Results of monotonic triaxial tests can provide valuable insight into results for the cyclic loading tests.

Effect of stress level

Ballast in railway track is normally subjected to low confining pressure. Indraratna *et al.* (1998) conducted a series of monotonic triaxial tests on ballast under a range of confining pressures from 1 kPa to 240 kPa (which simulate the typical confining pressures generated within ballasted track by the passage of unloaded to fully loaded trains). Their results showed that the peak shear stress increased with confining stress, as shown in Figure 2.8. At very low confining pressure, ballast specimens exhibited dilatancy, while at higher levels of confining pressure (e.g. >120 kPa) an overall volume compression was observed over a wide range of axial strains.

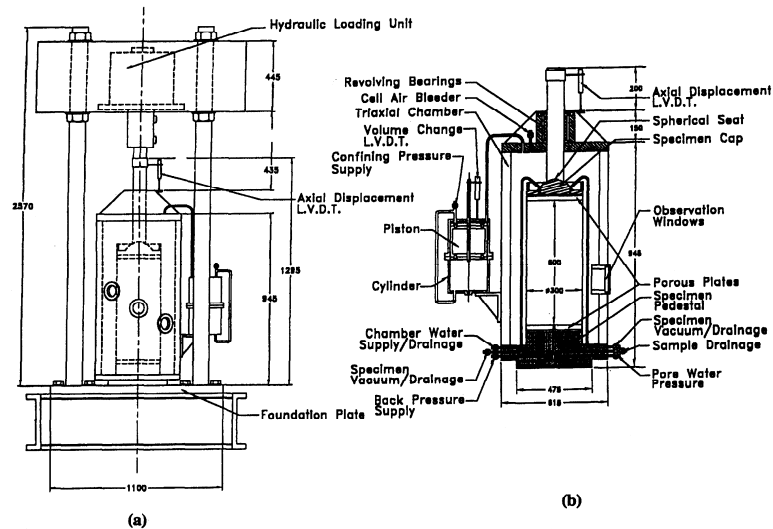


Figure 2.7. Large-scale triaxial equipment: (a) schematic view of test frame with triaxial chamber and (b) detailed components of triaxial chamber (Indraratna *et al.*, 1998).

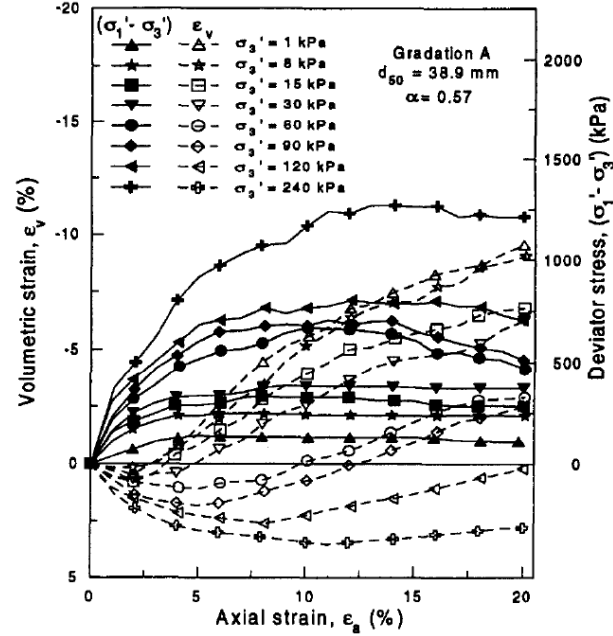


Figure 2.8. Experiment results of drained compression tests on ballast under different confining pressures (contraction positive) (Indraratna *et al.*, 1998).

Indraratna *et al.* (1998) compared the principal stress ratios at failure of ballast from the tests with those of other granular materials (e.g. sandy materials and rockfill) measured by Marsal (1967, 1973), Ponce and Bell (1971), Marachi *et al.* (1972), Charles and Watts (1980), Fukushima and Tatsuoka (1984). They found that the peak principal stress ratio was markedly higher at low confining pressure (e.g. <35 kPa) and that the peak principal stress ratio decreased rapidly with increasing confining pressure, as shown in Figure 2.9.

For granular material, a non-linear Mohr-Coulomb envelope is more noticeable at lower confining pressure (Oda and Iwashita, 1999; Powrie, 2004). Similar observations from monotonic triaxial tests on railway ballast under low confining pressure (e.g. less than 300 kPa) were reported by Raymond and Davies (1978)

and Indraratna *et al.* (1998). Figure 2.10 illustrates a typical Mohr-Coulomb envelope for ballast.

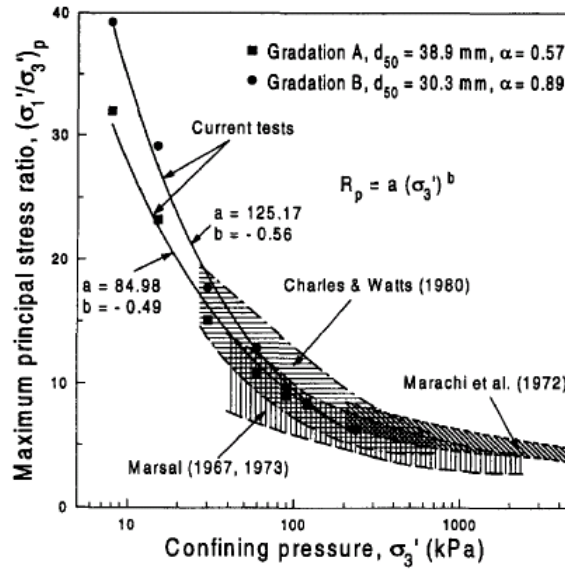


Figure 2.9. Influence of confining pressure on peak principal stress ratio for basalt in comparison with various granular media (Indraratna *et al.*, 1998).

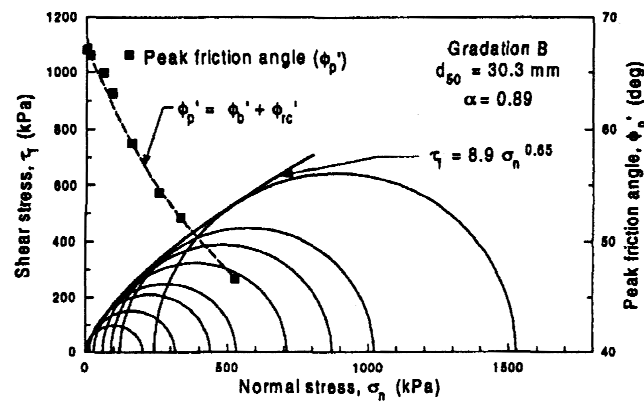


Figure 2.10. Mohr-Coulomb failure envelopes for Latite Ballast (Indraratna *et al.*, 1998).

For granular materials, like sand and rockfill, many researchers (e.g. Bishop, 1966; Vesic and Clough, 1968; Marsal 1967, 1973; Charles and Watts, 1980; Indraratna *et al.*, 1993) found that the peak friction angle decreased with increasing confining pressure. A similar relationship between peak friction angle and confining pressure for ballast was found by Indraratna *et al.* (1998), as shown in Figure 2.11. Indraratna *et al.* (1998) believed that the high values of the friction angle for ballast at low confining pressure are strongly related to the low interparticle contact forces and the interlocking of particles.

Effect of initial density

Roner (1985) conducted a number of triaxial tests on quartzite ballast and concluded that, independent of gradation and particle size, peak friction angle increased with decreasing initial voids ratio, as shown in Figure 2.12(a).

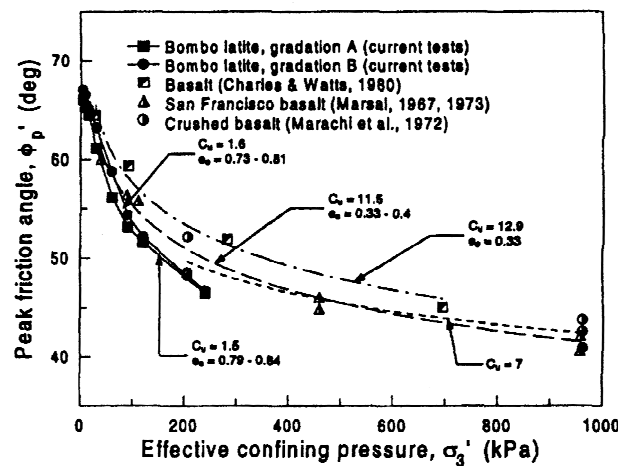
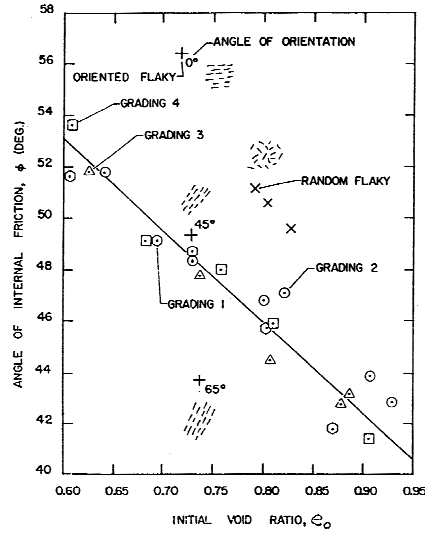
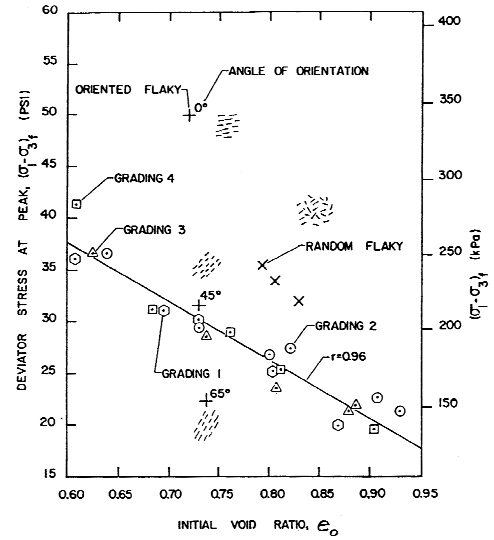


Figure 2.11. Influence of confining pressure on the peak angle of internal friction of Basalt at low to medium confining pressures (Indraratna *et al.*, 1998).



(a)



(b)

Figure 2.12. Effect of particle characteristics on (a) peak internal friction angle and (b) deviator stress at failure (Selig and Waters, 1994).

Effect of particle characteristics

As mentioned in the previous section, the behaviour of ballast is governed by particle characteristics. Although laboratory tests have been developed to determine trends for influence of particle characteristics on aggregate specimen performance, some effects of particle characteristics on the behaviour of ballast still need to be investigated.

Selig and Waters (1994) summarised the effect of shape characteristics on behaviour of granular materials. They indicated that any amount of flaky particles, either randomly oriented or oriented other than generally parallel to the failure plane, increase the shear strength of the granular assembly and that, when a significant proportion of the particles are flaky, orientation parallel to the failure

plane will cause a substantial strength reduction. Roner (1985) conducted triaxial tests on both flaky and non-flaky ballast specimens with random and different parallel particle orientations. The results showed that the random flaky specimens had a strength which is significantly greater than the strength at the corresponding voids ratio for the non-flaky specimens and that only if the particles were parallel to the failure plane a substantially lower strength occurred for the flaky specimens. The effect of ballast particle shape on the shear strength of the assembly is shown in Figure 2.12.

The shear strength of aggregate also increases with increasing particle angularity and particle surface roughness (Thom and Brown, 1988 and 1989). However, higher particle angularity and particle surface roughness would also tend to cause more particle breakage and a lower specimen stiffness.

As for the effect of gradation, Roner (1985) concluded that the shear strength was not affected by change of gradation on quartzite ballast specimens for equal voids ratios.

2.6 Mechanical Behaviour of Railway Ballast under Repeated Loading

Results of monotonic triaxial tests provide valuable information on the shear strength, stress-strain behaviour and degradation characteristics of typical ballast. However, because passing trains generate non-uniform vibrations and induce dynamic effects on the ballasted layer (Selig and Waters, 1994), the static tests

alone do not model the field situation completely. Thus, it is necessary to investigate the behaviour of ballast under repeated loading conditions.

Figure 2.13 shows complex elastic-plastic behaviour of ballast when subjected to repeated loadings. In general, the deformation of granular layers under repeated loading is characterized by a resilient deformation and a permanent deformation, as shown in Figure 2.14. However, the true nature of the deformation mechanism of a layer of granular material is not yet fully understood (Lekarp *et al.* 2000a). In this section, shakedown theory is firstly introduced; factors affecting both resilient and permanent behaviour of granular material will then be presented.

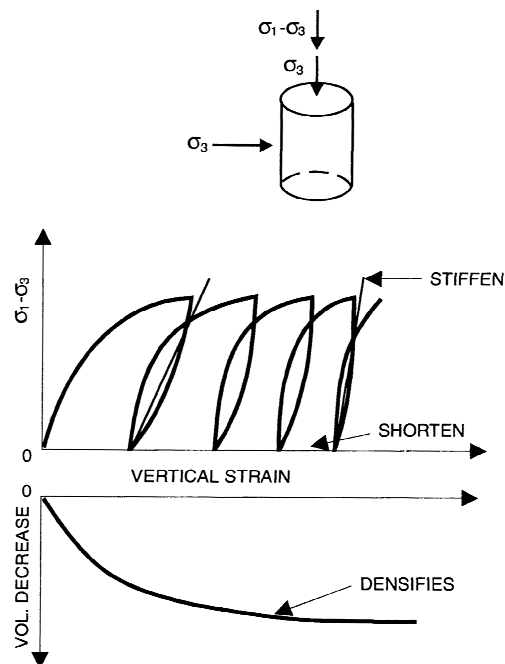


Figure 2.13. Ballast behaviour in the cyclic triaxial test (Selig and Waters, 1994).

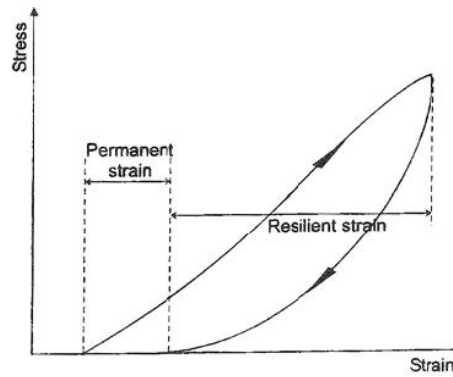


Figure 2.14. Strains in granular materials during one cycle of load application
(Lekarp *et al.*, 2000a).

2.6.1 Shakedown theory

The shakedown concept has been used to describe the evolution of the plastic deformation in materials under repeated loading. The basic assumption is that the structure can be modelled by an inhomogeneous elastic-plastic material. It predicts that the structure will eventually either shakedown or collapse. The critical load level separating these two types of behaviour is termed the “shakedown limit”. According to the shakedown theory (Collins and Boulbibane, 2000), four categories of material response under repeated loading can be distinguished:

1. Purely Elastic. The applied stress is sufficiently small, so that no permanent strain accumulation occurs.
2. Elastic Shakedown. The applied stress is slightly below the plastic shakedown limit. The material response is plastic for a finite number of cycles, however, the ultimate response is elastic.

3. Plastic Shakedown. The applied stress is low enough to avoid a rapid incremental collapse. The material achieves a long-term steady state response with no accumulation of plastic strain, but hysteresis in the stress-strain plot.
4. Incremental Collapse. The repeated stress is relatively large, so that a significant zone of material is in a yielding condition and plastic strain accumulates rapidly with failure occurring in the relatively short term.

Figure 2.15 shows these four types of response of elastic-plastic structure to repeated loading.

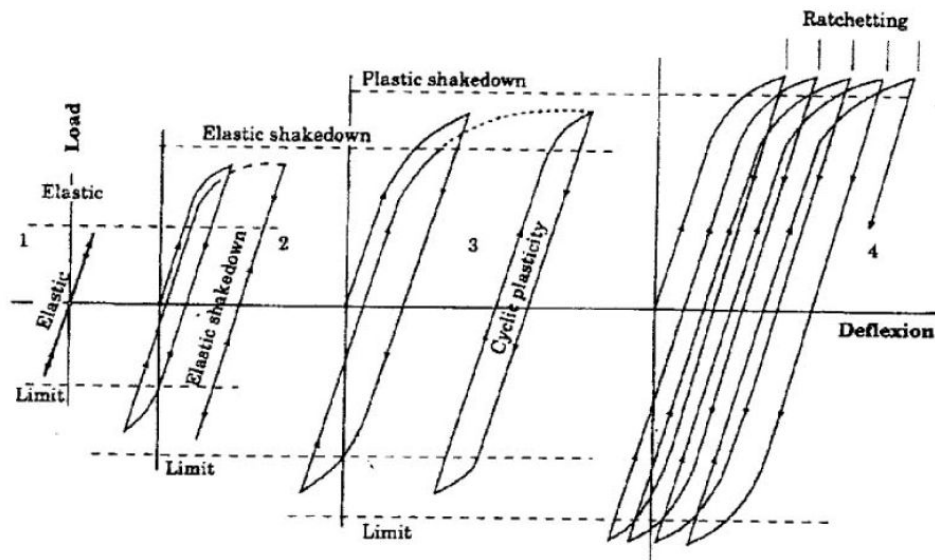


Figure 2.15. Four types of response of an elastic-plastic structure to repeated loading
(Collins and Boulbibane, 2000).

When the load level exceeds the elastic limit load, permanent plastic strains occur and the response of the structure to a second and subsequent loading cycle is

different from the first. Three basic causes are postulated by Collins and Boulbibane (2000) as follows:

1. Residual stresses are induced in the structure by the application of a load cycle, therefore, the total stress field induced in the second cycle is the sum of this residual stress field and that produced by the applied load.
2. Material properties (e.g. strain hardening or softening) change due to the previous loading.
3. The geometry of the surface is changed, as a consequence of the permanent strains induced there.

2.6.2 The cyclic triaxial test and the box test

Over the years, many researchers have studied the complex behaviour of granular materials using laboratory and in-situ testing techniques. The cyclic triaxial test (Indraratna *et al.*, 2005; Suiker *et al.*, 2005; and Lackenby *et al.*, 2007) is a common laboratory test used to investigate the mechanical behaviour of railway ballast under a large number of passing train wheels.

Norman and Selig (1983) developed a box test, in which sleeper settlement, ballast breakage and abrasion, changes of density and stiffness of ballast, and horizontal residual stresses in the ballast during cyclic loading were investigated. McDowell *et al.* (2005) developed the box test to simulate the effects of train loading and tamping on the performance of ballast. Both resilient and permanent behaviour of ballast under cyclic loading were investigated in their box tests. Figures 2.16 and

2.17 show the section of ballast underneath the rail seat modelled in the box test and the set up of the box test, respectively (Lim, 2004).

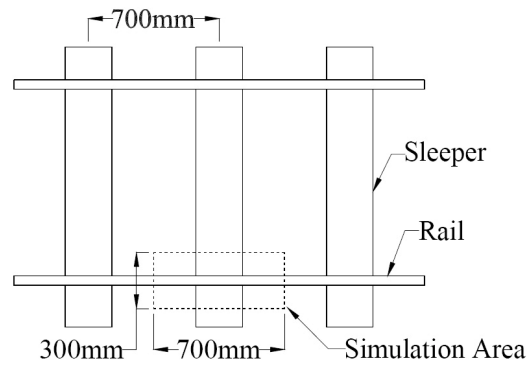
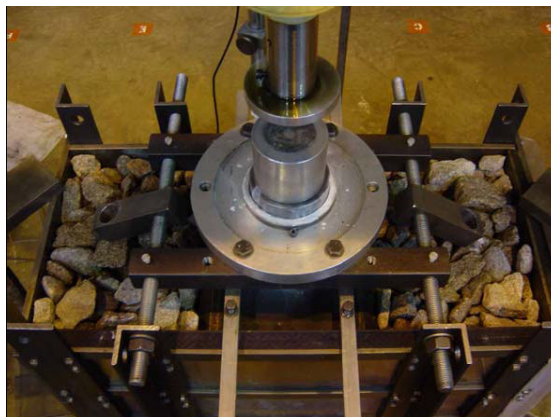
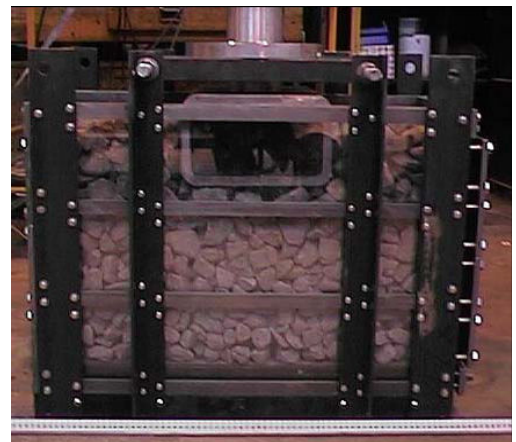


Figure 2.16. Plan of rail and sleepers showing section represented by the box test (Lim, 2004).



(a)



(b)

Figure 2.17. Box test set-up: (a) view from the top of the box and (b) front view (Lim, 2004).

2.6.3 Factors affecting resilient response

According to Seed *et al.* (1962), the resilient modulus of a material is defined as the repeated deviator stress divided by the recoverable axial strain during unloading in the triaxial test, as shown in Figure 2.14. The resilient response of railway ballast under cyclic loading is affected by many factors (e.g. confining pressure, stress ratio, number of loading cycles, stress history, density, particle sizes and grading, fines content, and aggregate type) (Lekarp *et al.*, 2000a). In this subsection, the main factors that affect the resilient response of ballast are presented.

Effect of stress level

Lekarp *et al.* (2000a) summarised that the resilient response of granular material is influenced mostly by stress level. Lackenby *et al.* (2007) conducted a series of triaxial test on ballast and indicated that the resilient modulus increased with increasing confining pressure, as shown in Figure 2.18.

Effect of initial density

It is widely accepted that the resilient modulus of granular material generally increases with increasing density (e.g. Trollope *et al.*, 1962; Hicks, 1970; Robinson, 1974; Rada and Witczak, 1981; Kolisoja, 1997). However, for railway ballast, Shenton (1974) indicated that the porosity have little influence on the resilient modulus. Thom and Brown (1988), and O'Reilly and Brown (1991) also reported similar observations in their studies.

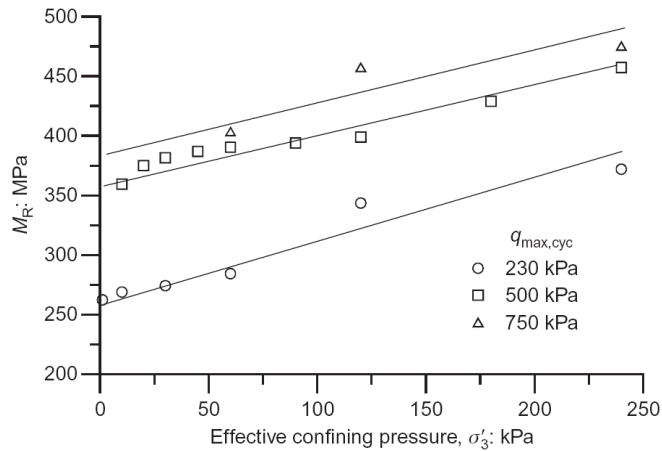


Figure 2.18. Resilient modulus M_R response under various stress states after 500,000 cycles (Lackenby *et al.*, 2007).

Effect of frequency and number of cycles

It is generally agreed that the impact of frequency and load duration on the resilient behaviour of granular materials is not significant (e.g. Seed *et al.*, 1965; Morgan, 1966; Hicks, 1970; Boyce *et al.*, 1976; Thom and Brown, 1988).

Suiker *et al.* (2005) and Lackenby *et al.* (2007) conducted cyclic triaxial tests on ballast and showed that the application of cyclic loading can lead to a considerably increase in material stiffness. The resilient modulus generally increases gradually with the number of repeated load applications as the material stiffens (Moore *et al.*, 1970 and Lackenby *et al.*, 2007). Figure 2.19 shows the effect of the number of cycles on the resilient modulus. Researchers (Hicks, 1970; Shenton, 1974 and Alva-Hurtado, 1980) found that, after a certain number of repeated load applications, the material behaves in an almost purely resilient manner and the resilient modulus eventually comes to an approximately constant value.

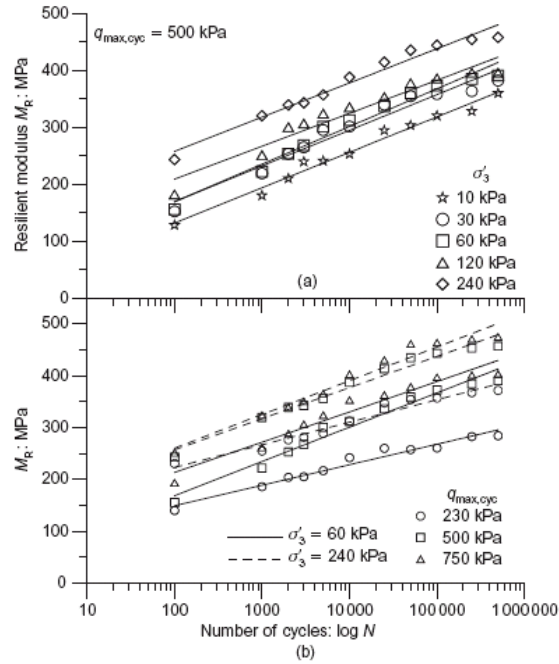


Figure 2.19. Resilient modulus M_R response under various stress states: (a) effect of confining pressure σ'_3 and number of cycles N on M_R for $q_{max,cyc} = 500$ kPa and (b) effect of $q_{max,cyc}$ on M_R for $\sigma'_3 = 60$ and 240 kPa (Lackeny *et al.*, 2007).

Effect of particle characteristics

Researchers (Janardhanam and Desai, 1983; Thom and Brown, 1989; Thompson, 1989; O'Reilly and Brown, 1991; and Lekarp *et al.*, 2000a) showed that the resilient behaviour of ballast is, to some degree, affected by the particle shape, particle size, particle strength and the gradation. Many studies (Hicks, 1970; Hicks and Monismith, 1971; Allen, 1973; Allen and Thompson, 1974; Thom, 1988; Barksdale and Itani, 1989; Thom and Brown, 1989) have reported that crushed aggregates which have angular to subangular shaped particles give a higher resilient modulus than uncrushed gravel with subrounded or rounded particles. A rough particle surface is also said to result in a higher resilient

modulus. Thom and Brown (1988 and 1989) reported that for granular materials the resilient modulus increased with increasing particle surface friction angle (the surface friction angle between particle of approximately 20 mm and concrete surface). Kolisoja (1997) showed that the magnitude of the resilient modulus increased linearly with the equivalent or average particle size D_{ekv} , which was defined as:

$$D_{ekv} = \frac{D_{10} + D_{50} + D_{90}}{3} \quad (2.1)$$

2.6.4 Factors affecting permanent strain response

The permanent strain of granular material after unloading is defined in Figure 2.14. Possible micro mechanisms for the accumulation of permanent strain under repeated loading are particle rearrangement and breakage. Factors affecting the permanent strain response of granular materials are present as follows:

Effect of stress level

The development of permanent strain is significantly influenced by stress level. Lackenby *et al.* (2007) conducted a series of cyclic triaxial tests on ballast under various loading conditions. They pointed out that permanent axial strain is dependent both on the magnitudes of maximum deviator stress and confining pressure. Figure 2.20 shows the permanent axial strain and permanent volumetric strain response as a function of number of cycles and confining pressure. They

found that permanent axial strain decreased with decreasing maximum deviator stress and increasing confining pressure.

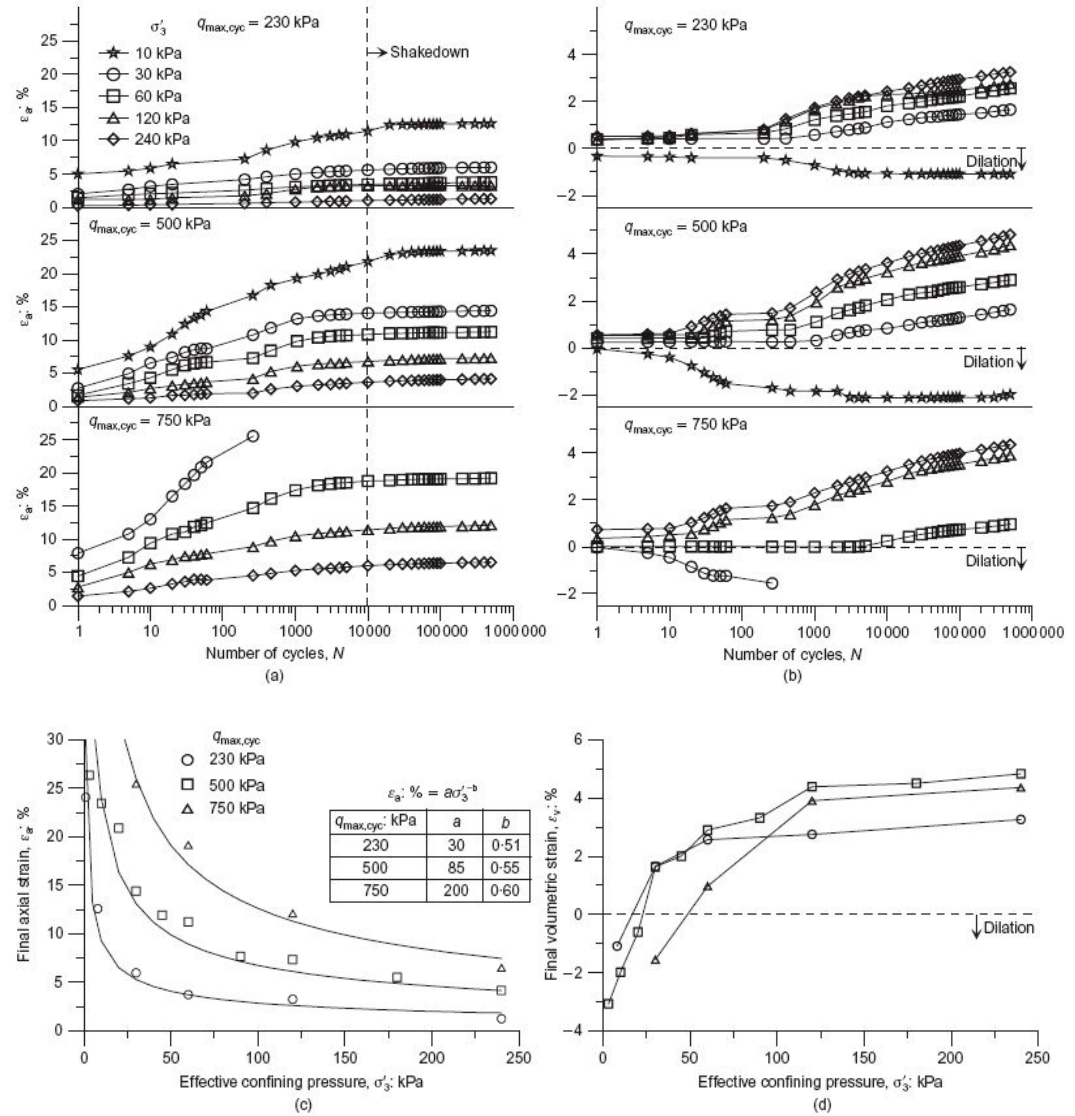


Figure 2.20. Strain response under cyclic loading: (a) axial strain ϵ_a as a function of the number of cycles N ; (b) volumetric strain ϵ_v as a function of N ; (c) final ϵ_a after 500,000 cycles and (d) final ϵ_v after 500,000 cycles (Lackenby *et al.*, 2007).

Effect of initial density

Initial density is one of the most important factors affecting the accumulation of permanent strain (Olowokere, 1975; Shenton, 1974; Knutson, 1976; Raymond and Davies, 1978; and Alva-Hurtado and Selig, 1981). Many researchers have found that a small decrease in initial density will lead to a significant increase in the accumulated permanent strain and that this effect is more significant for angular aggregates than rounded aggregates (Lekarp *et al.*, 2000b). Shenton (1974), Jeffs and Marich (1987), and Brown (1996) indicated that the resistance to accumulation of plastic deformation can be greatly improved if high initial compacted density is achieved.

Effect of frequency, number of cycles and sequence of loading

Shenton (1974) investigated the influence of loading frequency on the accumulation of permanent strain in ballast and showed that the loading frequency did not affect the accumulation of permanent strain. Figure 2.21 shows a plot of normalised axial strain after 10^4 cycles against frequency for the same value of deviator and confining stress (Shenton, 1974). Recently, Eisenmann *et al.* (1994) demonstrated that only the higher range of frequencies specific to high-speed lines (speed > 225 km/h) would affect the settlement of ballast. Thus, in general, the response approximately is frequency independent, except that higher frequencies may cause a dynamic increment to be superimposed on the “static” load.

For railway ballast under typical wheel load, it is widely agreed that permanent deformation is generally proportional to the logarithm of the number of loading

cycles, as shown in Figure 2.22. The rate of accumulation of permanent strain has generally been found to decrease with increasing number of cycles (Morgan, 1966; Barksdale, 1972; Shenton, 1974; Sweere, 1990; and McDowell *et al.*, 2005). However, Lekarp (1997) and Lekarp and Dawson (1998) indicated that for low applied stress, granular material has a limiting permanent strain, while, for high applied stress, the rate of accumulation of permanent strain will continue to increase with increasing number of cycles (i.e. the structure collapse). This is based on shakedown concept, as mentioned earlier.

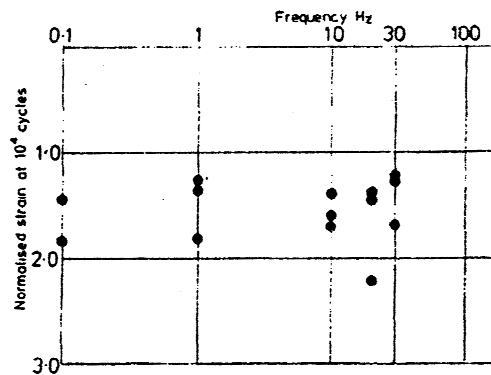


Figure 2.21. Effect of loading frequency (Shenton, 1974).

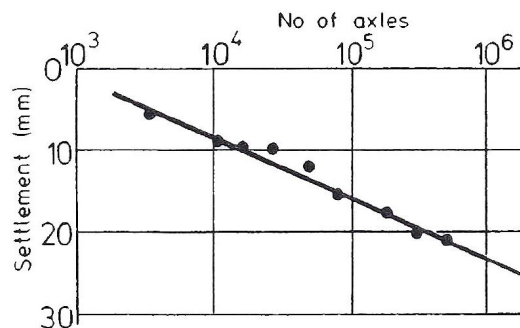


Figure 2.22. Permanent deformation as a linear function of logarithm of number of load cycle (Shenton, 1974).

The effect of the sequence of loading has been investigated by Stewart and Selig (1984) and Selig and Waters (1994). Their results showed that the sequence of loading did not affect the accumulation of permanent strain. Figure 2.23 shows typical results strain accumulation for different loading sequences. In these experimental tests different magnitudes of deviator stress were used and the deviator stress was changed after every 1000 load applications. Clearly the final permanent strains for all the different loading sequences are approximately equal.

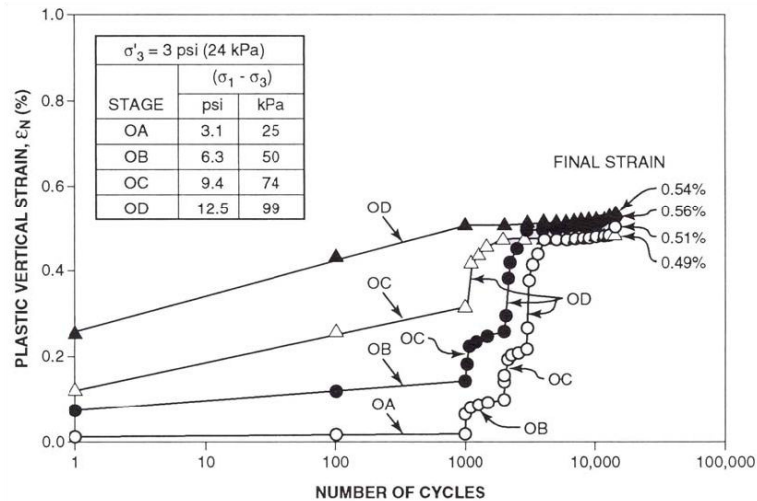


Figure 2.23. Effect of difference in sequence of loading on permanent strain (Selig and Waters, 1994).

2.7 Degradation of Granular Materials

Crushing is a progressive process that can start at relatively low stresses, and results in gradual changes in the soil fabric and packing. Particle crushing is governed by grain size and shape, the magnitudes of the applied stresses, and the mineralogy and strengths of individual grains. The influence of particle degradation on the mechanical behaviour of granular material has been studied by

many researchers (Marsal, 1967; Vesic and Clough, 1968; Hardin, 1985; Indratana *et al.*, 1998; and Ueng and Chen, 2000). Indraratna *et al.* (1998) pointed out that the crushing of particles is a decisive factor in the behaviour of ballast. They indicated that the breakage of ballast is related macroscopically to the applied deviator stress and confining pressure, and microscopically to the excessive contact stresses generated within the body of angular particles. However, because ballast is highly inhomogeneous in nature, it is difficult to predict mechanisms of degradation upon loading. In the following subsections, different types of particle breakage and the mechanism of single particle fracture are presented. Factors affecting particle breakage are also presented. Finally, the mechanism of ballast degradation under repeated loading is discussed.

2.7.1 Description of particle breakage

According to Raymond and Diyaljee (1979), the process of degradation of ballast particles due to wheel loading can occur in three ways:

1. The breakage of particles into approximately equal parts.
2. The breakage of angular projections
3. The grinding off of small-scale asperities.

A similar description of particle breakage in sand was reported by Nakata *et al.* (1999). It should be noted that the description of breakage given to each particle relies heavily on visual observation and requires a measure of personal judgement.

2.7.2 Single particle under compression

A study of single particle fracture (when compressed between flat platens) provides a useful insight to the fundamental mechanisms of particle fracture. It also provides a useful method to quantify, scientifically, the tensile strength of different particles (e.g. McDowell and Amon, 2000; McDowell, 2002; McDowell *et al.*, 2003; Lim 2004). However, particles within a granular assembly interact with neighbours leading to considerably complex loading paths. Contact forces between particles are unique in magnitude and direction, depending on the size and shape of grains, the particle arrangement and the number of contact points (Marsal, 1973). The loading path is complicated further by the variation in particle strengths within the assembly.

It is widely accepted that the failure of a spherical particle under compression is a tensile failure. Particle fractures are initiated through existing internal flaws in which stress concentration occurs. According to Jaeger (1967), the tensile strength of rock grains can be indirectly measured by diametral compression between flat platens. Lee (1992) following Jaeger (1967) calculated the tensile strength of grain (e.g. Leighton Buzzard sand, oolitic limestone and carboniferous limestone) as

$$\sigma_f = \frac{F_f}{d^2} \quad (2.2)$$

where the subscript f denotes failure, σ is the tensile stress, F is the diametral force and d is the diameter of a grain. Recently, McDowell and Amon (2000) showed

that Weibull statistics (Weibull, 1951) can be applied to characterise soil particle strength. They showed that the mean tensile strength σ_{av} is a function of particle size d according to the equation

$$\sigma_{av} \propto d^{-3/m} \quad (2.3)$$

where m is the Weibull modulus. Lim *et al.* (2004) performed single particle crushing tests on a range of ballasts and found that for most ballasts, although a Weibull distribution of strengths was obtained within each size range, the size effect on the average strength was inconsistent with that predicted by Weibull statistics. This is in contrast to the results obtained by McDowell and Amon (2000) and McDowell (2002) for sand particles, which followed the Weibullian size effect. Lim *et al.* (2004) hypothesised that this may have been because those sands were each largely composed of one mineral.

2.7.3 Factors affecting particle degradation

In general, the breakage of ballast particles depends on several factors, including particle strength, particle shape, density, stress level, frequency, number of cycles, and degree of saturation (Indraratna *et al.*, 2004). Indraratna *et al.* (2004) divided these factors into three categories as follows:

1. Properties related to the characteristics of the parent rock (e.g. hardness, specific gravity, toughness, weathering, mineralogical composition, internal bonding and grain size).

2. Properties associated with the blasting, crushing and transportation processes (e.g. roundness, particle shape, particle size and surface smoothness).
3. Factors related to the field/experimental variables (e.g. confining pressure, initial density or porosity, thickness of the ballast layer, ballast gradation, presence of water or ballast moisture content, and dynamic loading pattern including train speed and frequency).

The micro mechanics of crushable aggregates has also been studied by researchers (e.g. Lee, 1992; Lade *et al.*, 1996; McDowell *et al.*, 1996; McDowell and Amon, 2000; Lim *et al.*, 2004). According to McDowell *et al.* (1996), the survival probability of a particle in an aggregate subjected to one-dimensional compression is determined by the applied macroscopic stress, the size of the particle and the coordination number.

Applied macroscopic stress

An increase in applied macroscopic stress would increase the average induced tensile stress in a particle; and this leads to a higher probability of particle breakage. Experimental results (Indraratna *et al.*, 1998) showed that for the same ballast material, more particle breakage is observed when the applied stress increases.

Size of particle

There is a variation in soil particle strength because of the dispersion in internal flaw sizes. Since large particles contain more flaws or defects compared to smaller particles, it exhibits a lower average tensile strength. Thus, the probability of particle breakage increases with an increase in particle size.

Coordination number

The probability of particle breakage also reduces with an increase in the coordination number because the induced tensile stress in a particle is reduced by the compressive stress caused by the many contacts. The coordination number depends on particle shape, particle size, gradation and density.

2.7.4 Ballast degradation under cyclic loading

Ballast breakage index (BBI) was introduced by Indraratna *et al.* (2005) to quantify the magnitude of degradation of railway ballast. BBI can be calculated from Equation 2.4, where A and B are defined in Figure 2.24.

$$BBI = \frac{A}{A + B} \quad (2.4)$$

Lackenby *et al.* (2007) indicated that ballast degradation behaviour under cyclic loading can be categorised into three zones, namely: the dilatant unstable degradation zone (DUDZ), the optimum degradation zone (ODZ), and the compressive stable degradation zone (CSDZ). These zones are dependent on the

level of confining pressure and maximum deviator stress acting on the specimen, as shown in Figure 2.25.

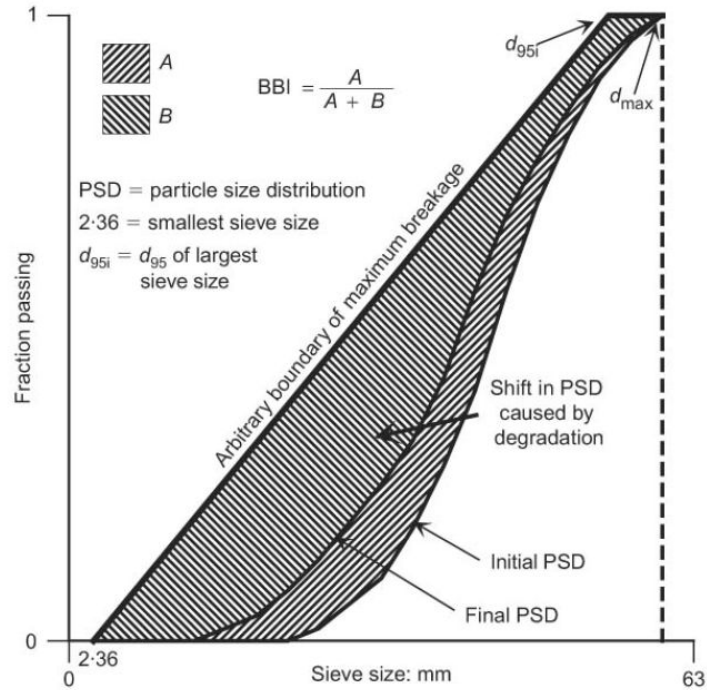


Figure 2.24. Ballast breakage index (Indraratna *et al.*, 2005).

Dilatant unstable degradation zone (DUDZ)

Degradation in the DUDZ is the most significant among the three zones. Breakage occurs mainly at the onset of loading, when the axial strain and dilation rates are at a maximum. Lackenby *et al.* (2007) found that most of the degradation in this zone was due to the breakage of angular corners or projections, rather than particle splitting. They indicated that this is due to internal deformation mechanisms, such as sliding or rolling, that inhibit the formation of permanent interparticle contacts, thus preventing splitting due to excessive stresses.

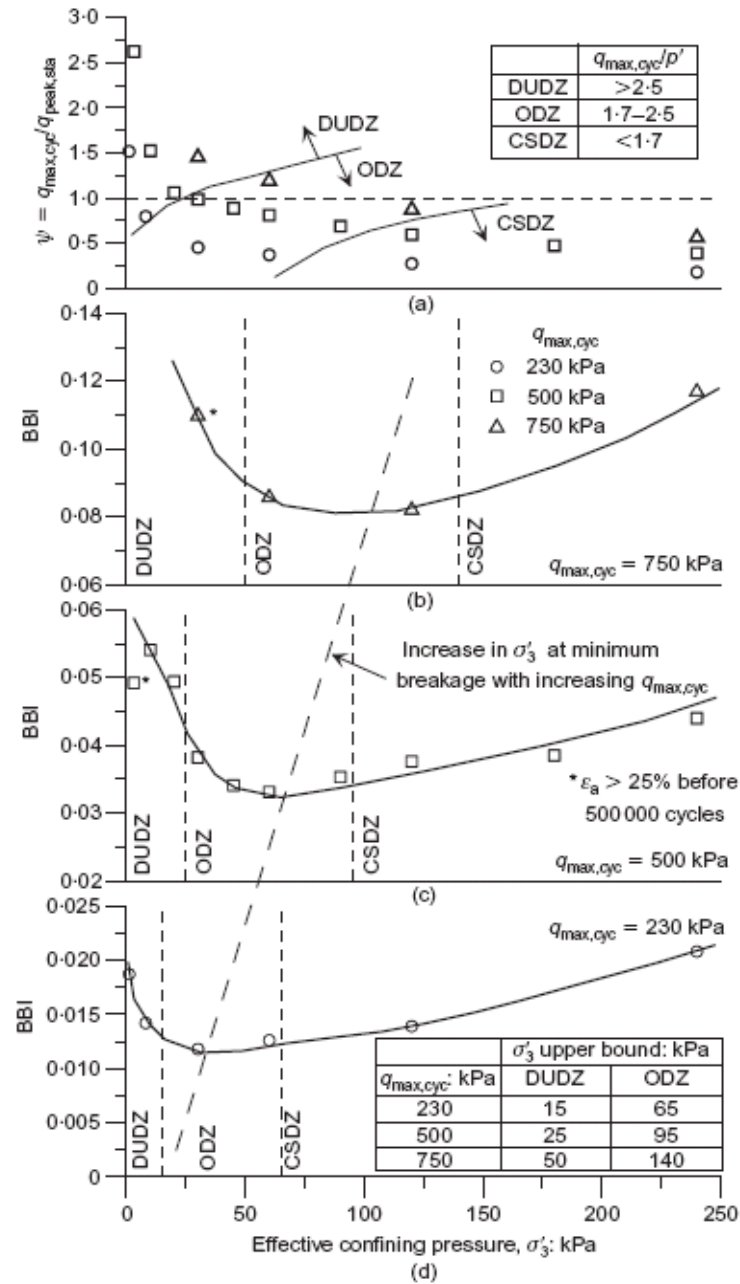


Figure 2.25. Effect of confining pressure σ'_3 and maximum deviator stress $q_{max,cyc}$ on ballast breakage index BBI, and effect of $q_{max,cyc}$ on DUDZ, ODZ and CSDZ breakage zones (Lackenby *et al.*, 2007).

Optimum degradation zone (ODZ)

Lackenby *et al.* (2007) indicated that, as the results of small increase of confining pressure, an optimum internal contact stress distribution and increased interparticle contact area occurred in ODZ. Therefore, tensile stresses within particles were diminished and breakage was reduced significantly. Besides, the coordination number was expected to be slightly increased (compared with DUDZ specimens) owing to the reversal of volumetric strain behaviour (from dilation to compression)

Compressive stable degradation zone (CSDZ)

According to Lackenby *et al.* (2007), breakage was more significant in CSDZ than in the ODZ. They found that although corner degradation was still the foremost kind of breakage, some particle splitting takes place and that the fatigue of particles became more prominent in the CSDZ. They postulated that particles were highly stressed and contact forces were more isotropic under increasing confining pressure.

2.8 Summary

Railway ballast generally comprises large, angular particles of typical size approximately 40 mm. It places at the top layer of the substructure where the sleepers are embedded. The main functions of railway ballast are to reduce pressures from the sleeper bearing area to acceptable levels at the surface of the subgrade soil, to facilitate maintenance operations for re-establishment of track riding quality, and to provide rapid drainage. The ability of ballast to perform its

functions depends on the particle characteristics (e.g. particle size, shape, angularity, hardness, surface texture, gradation and durability) together with the in-situ physical state (e.g. grain structure and density). Durability, particle shape and gradation are three main particle characteristics influencing the mechanical behaviour of ballast.

Ballast functions deteriorate through the actions of traffic loading and maintenance tamping. Laboratory tests (e.g. monotonic and cyclic triaxial tests, box tests) have been carried out to investigate the mechanical behaviour of ballast by researchers. The mechanical behaviour of ballast under static loading is mainly affected by stress level, initial density, particle angularity and particle surface roughness. Under low confining pressure, ballast exhibits high dilatancy and high principal stress ratios as result of the low interparticle contact forces and the interlocking of particles. Under repeated loading, the resilient and permanent behaviour of ballast are mainly affected by the confining pressure and the applied cyclic loading.

Particle crushing is a progressive process that can start at relatively low stresses, and certainly dominates the behaviour of the assembly at very high effective stress. The degree of particle breakage affects the deformation and the ultimate strength characteristics of ballast, and therefore the performance of the track. Ballast particle breakage can occur in three ways (i.e. the splitting of particles, the breakage of angular projections and the grinding of small-scale asperities). The particle breakage depends on the applied macroscopic stress, the size of particle and the coordination number. The mechanism of ballast degradation under

repeated loading depends both on the confining pressure and maximum deviator stress.

CHAPTER 3

LITERATURE REVIEW: DISCRETE ELEMENT MODELLING OF GRANULAR MATERIAL

3.1 Introduction

Granular materials are composed of distinct particles which displace independently from one another and interact only at contact points. The discrete characteristics of the granular material result in complex behaviour under different loading conditions. The discrete element method provides a way of investigating the mechanical behaviour of granular materials both microscopically and macroscopically. In the modelling of granular materials, the discrete element method has the advantage that it enables the investigation of some features which are not easily measured in laboratory tests, such as interparticle friction, distribution of contact forces, coordination number, and particle movement. Furthermore, an identical prepared sample can be reused for different loading conditions in discrete element modelling. Therefore, the material properties and the effect of loading condition can be investigated without any influence from the initial sample preparation method.

Cundall and Strack (1979) firstly applied the discrete element method (DEM) to granular materials and showed that DEM is a valid tool for fundamental research into the behaviour of granular materials by comparing the numerical results with the results from photoelastic analysis. Parallel with the development of computational capacity, DEM has been used increasingly over the past three decades to investigate the behaviour of granular materials from a micro mechanical point of view. However, some effects of micro properties are not yet fully understood, such as particle shape, interparticle friction, contact constitutive law and fabric (i.e. particle arrangement and orientation).

This chapter generally contains the basic knowledge of DEM and PFC^{3D} and the developments and recent achievements of DEM. In section 3.2, a description of the conceptual model of the discrete element method is presented first. Then, attention is given to the computer code PFC^{3D}, which is a simplified implementation of DEM. The general mathematical background and some specific features (i.e. bonding models and clump logic) are presented. In section 3.3, the effects of particle shape in discrete element modelling are discussed, together with the introduction of two methods used to model the effect of particle shape. The effect of interparticle friction on mechanical behaviour of granular material is discussed in section 3.4. Section 3.5 shows two main methods of simulating particle breakage in two-dimension and three-dimension. Finally, recent applications of PFC in modelling mechanical response of railway ballast are reviewed and presented in section 3.6.

3.2 Introduction to the Discrete Element Method and PFC^{3D}

3.2.1 The discrete element method

The discrete element method was first developed by Cundall (1971) for rock mechanics problems and later applied to granular materials by Cundall and Strack (1979). Cundall and Hart (1992) defined the scope of the discrete element method and summarized fundamental aspects in the modelling of discrete element systems. In their definition, the DEM allows finite displacements and rotations of discrete bodies, including complete detachment, and recognises new contacts automatically as the calculation progresses.

The DEM models granular materials as packed assemblies of discrete elements. This method is based on the use of an explicit numerical scheme in which the interaction of the particles is modelled contact by contact and the motion of the particles is modelled particle by particle. Therefore, the DEM makes it possible to analyse the mechanics of granular materials at both micro and macro levels.

In the DEM, the interaction of the particles is treated as a dynamic process with states of equilibrium developing whenever the internal forces balance. The contact forces and displacements of a stressed assembly of particles are found by tracing the movements of the individual particles. Movements result from the propagation through the particle system of disturbances caused by specified wall and/or particle motion, and body forces.

The dynamic behaviour is represented numerically by a timestepping algorithm in which it is assumed that the velocities and accelerations are constant within each timestep. The solution scheme is identical to that used by the explicit finite-difference method for continuum analysis. DEM is based upon the idea that the timestep is so small that, during a single timestep, disturbances cannot propagate from any particle further than its immediate neighbours. Then, at all times, the forces acting on any particle are determined exclusively by its interaction with the particles with which it is in contact.

The calculations performed in the DEM alternate between the application of Newton's second law to the particles and a force-displacement law at the contacts. Newton's second law is used to determine the motion of each particle arising from the contact and body forces acting upon it, while the force-displacement law is used to update the contact forces arising from the relative motion at each contact. More details about the calculation algorithm are described further in a later section.

3.2.2 The PFC^{3D} Particle-Flow Model

PFC^{3D} models stressed assemblies by the movement and interaction of rigid spherical particles based on the DEM. The model is composed of distinct spheres that displace independently of one another and interact only at contacts or interfaces between the particles. The assumptions made in PFC^{3D} are:

1. The particles are treated as rigid bodies.
2. The contacts occur over a vanishingly small area (i.e. at a point).

3. A soft-contact approach is used in the contacts so that the rigid particles are allowed to overlap one another at the contact points.
4. The magnitude of the overlap is related to the contact force via the force-displacement law.
5. Bonds can exist at contacts between particles.
6. All particles are spherical; however, the clump logic supports the creation of super-particles of arbitrary shape. Each clump consists of a set of overlapping spheres, and acts as a rigid body with a deformable boundary.

In PFC^{3D}, the ball and the wall are the two basic entities. Walls allow one to apply velocity boundary conditions to assemblies of balls for purposes of compaction and confinement. The balls and walls interact with one another via the forces that arise at contacts. PFC^{3D} is suitable for modelling the stress-strain response of a granular material, which deformation results primarily from the sliding and rotation of the rigid particles and the interlocking at particle interfaces. More complex behaviour of granular materials can be modelled by allowing the particles to be bonded together at their contact points, so that internal forces (i.e. tensile, shear or moment) are allowed to develop at the contacts. Some basic conceptual models and the mathematical background of PFC^{3D} are presented in the following subsections. Further information with regard to PFC^{3D} can be found in the PFC^{3D} manual (Itasca, 1999).

3.2.3 Calculation cycle

The calculation cycle in PFC^{3D} is a timestepping algorithm that requires the repeated application of the law of motion to each particle, a force-displacement law to each contact, and constant updating of wall positions. Figure 3.1 illustrates the calculation cycle. At the start of each timestep, the contacts are updated from the particle and wall positions. The force-displacement law is then applied to each contact to update the contact forces based on the relative motion between the two contacted entities and the contact constitutive model. Then, the law of motion is applied to each particle to update its velocity and position based on the resultant force and moment arising from the contact forces and any body forces acting on the ball. Also the wall positions are updated based on the specified wall velocities.

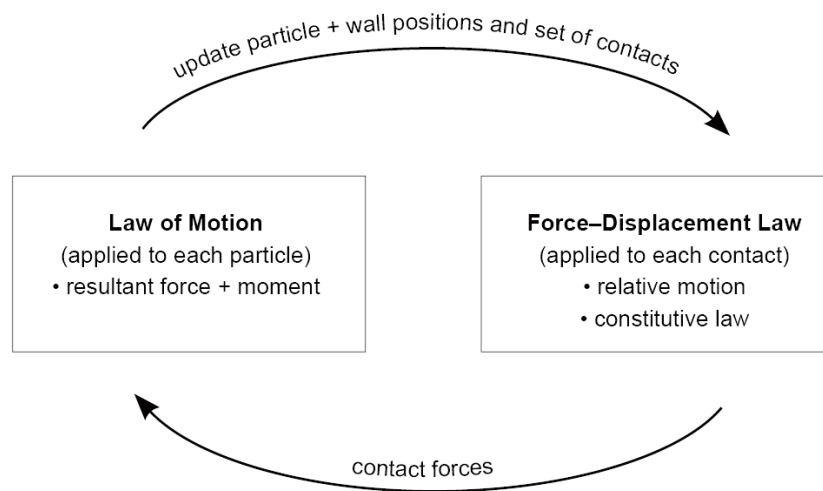


Figure 3.1. Calculation cycle use in PFC^{3D} (Itasca, 1999).

Force-Displacement law

The contact force vector F_i can be resolved into normal and shear components (F_i^n and F_i^s) with respect to the contact plane as

$$F_i = F_i^n + F_i^s \quad (3.1)$$

The force-displacement law relates the relative displacement between two entities at a contact to the contact force acting on the entities via the normal and shear stiffnesses at the contact. The normal contact force vector is calculated by

$$F_i^n = K^n U^n n_i \quad (3.2)$$

where K^n is the normal stiffness [force/displacement] at the contact and U^n is the overlap of the two entities. The shear contact force is calculated in an incremental fashion. When the contact is formed, the total shear contact force is initialized to zero. Each subsequent relative shear-displacement increment results in an increment of elastic shear force that is added to the current value. The shear elastic force-increment vector is calculated by

$$\Delta F_i^s = -k^s \Delta U_i^s \quad (3.3)$$

where k^s is the shear stiffness [force/displacement] at the contact and ΔU_i^s is the shear component of the contact displacement-increment vector calculated from the motion. Finally, the new shear contact force is calculated by summing the shear

force vector existing at the start of the timestep with the shear elastic force-increment vector

$$F_i^s = \{F_j^s\}^{[old]} + \Delta F_i^s \quad (3.4)$$

Law of motion

The motion of a single particle is determined by the resultant force and moment vectors acting upon it. The equations of motion can be expressed as two vector equations. One of the equations of motion relates the resultant force to the translational motion, as

$$F_i = m(\ddot{x}_i - g_i) \quad (3.5)$$

where F_i is the resultant force, m is the total mass of the particle, and g_i is the body force acceleration vector. The other equation of motion relates the resultant moment to the rotational motion, as

$$M_i = \dot{H}_i \quad (3.6)$$

where M_i is the resultant moment acting on the particle, and H_i is the angular momentum of the particle. For a spherical particle of radius R with uniform density, Equation 3.6 can be simplified and referred to the global-axis system as

$$M_i = I\dot{\omega}_i = \left(\frac{2}{5}mR^2\right)\dot{\omega}_i \quad (3.7)$$

For the clump, the equations of motion are further described in the section 3.3.3.

The equations of motion, given by Equations 3.5 and 3.7, are integrated using a centred finite-difference procedure involving a timestep of Δt . The quantities \dot{x}_i and ω_i are computed at the mid-intervals of $t \pm n\Delta t/2$, while the quantities x_i , \ddot{x}_i , $\dot{\omega}_i$, F_i , and M_i are computed at the primary intervals of $t \pm n\Delta t$. The accelerations are calculated as

$$\ddot{x}_i^{(t)} = \frac{1}{\Delta t} \left(\dot{x}_i^{(t+\Delta t/2)} - \dot{x}_i^{(t-\Delta t/2)} \right) \quad (3.8)$$

$$\dot{\omega}_i^{(t)} = \frac{1}{\Delta t} \left(\omega_i^{(t+\Delta t/2)} - \omega_i^{(t-\Delta t/2)} \right) \quad (3.9)$$

Inserting these expressions into Equations 3.5 and 3.7 and solving for the velocities at time $(t \pm \Delta t/2)$ result in

$$\dot{x}_i^{(t+\Delta t/2)} = \dot{x}_i^{(t-\Delta t/2)} + \left(\frac{F_i^{(t)}}{m} + g_i \right) \Delta t \quad (3.10)$$

$$\omega_i^{(t+\Delta t/2)} = \omega_i^{(t-\Delta t/2)} + \left(\frac{M_i^{(t)}}{I} \right) \Delta t \quad (3.11)$$

Finally, the position of the particle centre for the next cycle can be calculated by

$$x_i^{(t+\Delta t)} = x_i^{(t)} + \dot{x}_i^{(t+\Delta t/2)} \Delta t \quad (3.12)$$

3.2.4 Contact constitutive model

The overall constitutive behaviour of a material is simulated in PFC^{3D} by associating a simple constitutive model with each contact. Generally, the constitutive model acting at a particular contact consists of three parts: a stiffness model, a slip model and a bonding model.

Contact-stiffness model

The stiffness model provides an elastic relationship between the contact force and the relative displacement via a Force-Displacement Law (i.e. Equations 3.2 and 3.3). A linear contact-stiffness model is used in the simulations for this research. The linear contact model assumes that the stiffnesses of the two contacting entities A and B act in series. The contact stiffnesses for the linear contact model can be calculated by

$$K^n = \frac{k_n^{[A]}k_n^{[B]}}{k_n^{[A]} + k_n^{[B]}} \quad (3.13)$$

$$K^s = \frac{k_s^{[A]}k_s^{[B]}}{k_s^{[A]} + k_s^{[B]}} \quad (3.14)$$

where the superscripts [A] and [B] denote the two entities in contact.

The Slip Model

The slip model, which is an intrinsic property of the two entities in contact, enforces a relationship between shear and normal contact forces such that the two

contacting balls may slip relative to one another. It is defined by the friction coefficient at the contact μ [dimensionless], where μ is taken to be the minimum friction coefficient of the two contacting entities. If the overlap is less than or equal to zero, then both the normal and shear contact forces are set to zero. Otherwise, the contact is checked for slip conditions by calculating the maximum allowable shear contact force

$$F_{\max}^s = \mu |F_i^n| \quad (3.15)$$

If $|F_i^s| > F_{\max}^s$, then slip is allowed to occur (during the next calculation cycle) by setting the magnitude of F_i^s equal to F_{\max}^s via

$$F_i^s \leftarrow F_i^s \left(F_{\max}^s / |F_i^s| \right) \quad (3.16)$$

The bonding models

PFC^{3D} allows particles to be bonded together at contacts. Two bonding models are provided: a) a contact-bond model and b) a parallel-bond model. Once a bond is formed at a contact between two particles, the contact continues to exist until the bond is broken.

a) The contact-bond model

A contact bond can be envisaged as a pair of elastic springs with constant normal and shear stiffnesses acting at the contact point. These two springs have specified shear and tensile normal strengths. The constitutive behaviour relating the normal

and shear components of contact force and relative displacement for particle contact occurring at a point is shown in Figure 3.2. The contact bond breaks when the contact force exceeds either the normal contact bond strength or the shear contact bond strength.

b) The parallel-bond model

A parallel bond can be envisaged as column of elastic glue lying on the contact plane. The parallel bond can transmit both forces and moments between particles. The constitutive behaviour of the parallel bond is similar to that of the contact bond, as shown in Figure 3.2. Relative motion at the contact causes a force and a moment to develop within the parallel bond as a result of the stiffness of the parallel bond. The parallel bond breaks when the stress in any part of the bond exceeds the parallel bond strength.

The total force and moment associated with the parallel bond are denoted by \bar{F}_i and \bar{M}_i . Each of these vectors can be resolved into normal and shear components with respect to the contact plane as

$$\bar{F}_i = \bar{F}_i^n + \bar{F}_i^s \quad (3.17)$$

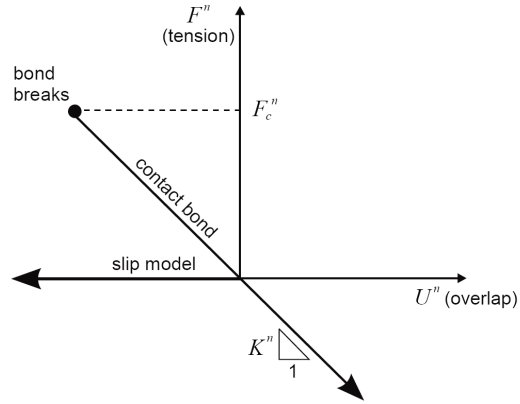
$$\bar{M}_i = \bar{M}_i^n + \bar{M}_i^s \quad (3.18)$$

where \bar{F}_i^n , \bar{M}_i^n and \bar{F}_i^s , \bar{M}_i^s denote the normal and shear component vectors, respectively. These vectors are shown in Figure 3.3. The maximum tensile and shear stresses acting on the bond periphery can be calculated by

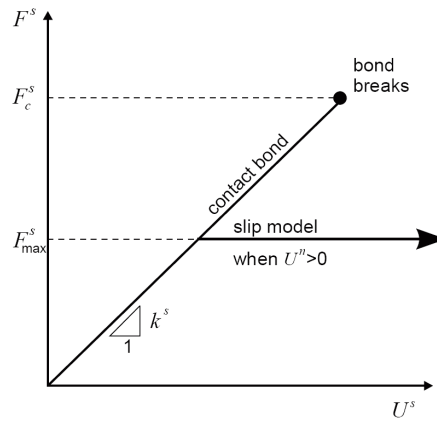
$$\sigma_{\max} = \frac{-\bar{F}^n}{A} + \frac{|\bar{M}_i^s|}{I} \bar{R} \quad (3.19)$$

$$\tau_{\max} = \frac{|\bar{F}_i^s|}{A} + \frac{|\bar{M}^n|}{J} \bar{R} \quad (3.20)$$

where A is the area of the bond disc, J is the polar moment of inertia of the disc cross-section, I is the moment of inertia of the disc cross-section about an axis through the contact point and \bar{R} is the radius of the bond disc.



(a) Normal component of contact force



(b) Shear component of contact force

Figure 3.2. Constitutive behaviour for contact occurring at a point (Itasca, 1999).

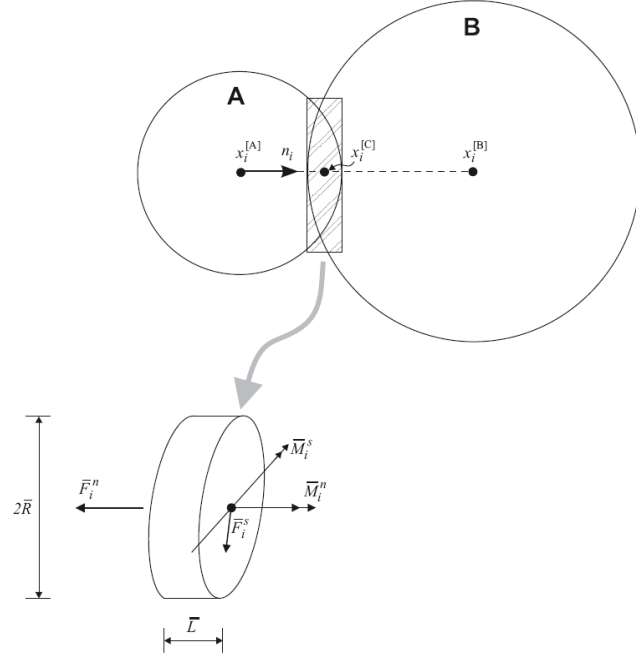


Figure 3.3. Parallel bond depicted as a cylinder of cementitious material (Itasca, 1999).

3.2.5 Clump logic

A clump is a single entity of overlapping balls (i.e. the balls comprising the clump remain at a fixed distance from each other). Internal overlapping contacts are ignored in calculations, resulting in a saving of computational time compared to a similar calculation in which all contacts are active. In this sense, a clump differs from a group of particles that are bonded to one another (an agglomerate).

The total mass of a clump m , the location of the centre of mass of clump $x_i^{[G]}$ and the moments and products of inertia I_{ii} and I_{ij} , which are the basic mass properties of a clump, are defined by the following equations

$$m = \sum_{p=1}^{N_p} m^{[p]} \quad (3.21)$$

$$x_i^{[G]} = \frac{1}{m} \sum_{p=1}^{N_p} m^{[p]} x_i^{[p]} \quad (3.22)$$

$$I_{ii} = \sum_{p=1}^{N_p} \left\{ m^{[p]} (x_j^{[p]} - x_j^{[G]})(x_j^{[p]} - x_j^{[G]}) + \frac{2}{5} m^{[p]} R^{[p]} R^{[p]} \right\} \quad (3.23)$$

$$I_{ij} = \sum_{p=1}^{N_p} \left\{ m^{[p]} (x_i^{[p]} - x_i^{[G]})(x_j^{[p]} - x_j^{[G]}) \right\} ; (j \neq i) \quad (3.24)$$

where N_p is the number of balls in the clump, $m^{[p]}$ is the mass of a ball, $x^{[p]}$ is the centroid location of the ball and $R^{[p]}$ is the radius of the ball.

The motion of a clump is determined by the resultant force and moment vectors acting upon it. Because a clump is treated as a rigid body, its motion can be described in terms of the translational motion of a point in the clump and the rotational motion of the entire clump. The equation for translational motion can be written in the vector form

$$F_i = m(\ddot{x}_i - g_i) \quad (3.25)$$

where F_i is the resultant force, the sum of all externally-applied forces acting on the clump and g_i is the body force acceleration vector arising from gravity loading. The equation for rotational motion can be expressed in the matrix form as

$$\{\mathbf{M}\} - \{\mathbf{W}\} = [\mathbf{I}]\{\boldsymbol{\alpha}\} \quad (3.26)$$

where

$$[\mathbf{M}] = \begin{Bmatrix} M_1 \\ M_2 \\ M_3 \end{Bmatrix}$$

$$[\mathbf{W}] = \begin{Bmatrix} \omega_2 \omega_3 (I_{33} - I_{22}) + \omega_3 \omega_3 I_{23} - \omega_2 \omega_2 I_{32} - \omega_1 \omega_2 I_{31} + \omega_1 \omega_3 I_{21} \\ \omega_3 \omega_1 (I_{11} - I_{33}) + \omega_1 \omega_1 I_{31} - \omega_3 \omega_3 I_{13} - \omega_2 \omega_3 I_{12} + \omega_2 \omega_1 I_{32} \\ \omega_1 \omega_2 (I_{22} - I_{11}) + \omega_2 \omega_2 I_{12} - \omega_1 \omega_1 I_{21} - \omega_3 \omega_1 I_{23} + \omega_3 \omega_2 I_{13} \end{Bmatrix}$$

$$[\mathbf{I}] = \begin{bmatrix} I_{11} & -I_{12} & -I_{13} \\ -I_{21} & I_{22} & -I_{23} \\ -I_{31} & -I_{32} & I_{33} \end{bmatrix}$$

$$[\boldsymbol{\alpha}] = \begin{Bmatrix} \alpha_1 \\ \alpha_2 \\ \alpha_3 \end{Bmatrix} = \begin{Bmatrix} \dot{\omega}_1 \\ \dot{\omega}_2 \\ \dot{\omega}_3 \end{Bmatrix}$$

in which $[\mathbf{M}]$ is the resultant moment about the centre of mass, ω_i is the angular velocity about the principal axis and $\dot{\omega}_i$ is the angular acceleration about the principal axes, referred to a local coordinate system that is attached to the clump at its centre of mass. The equations of motion, given by Equations 3.25 and 3.26, are integrated using a centred finite-difference procedure involving a timestep of Δt as described in section 3.2.3.

3.3 Influence of Particle Geometry in DEM

Due to the limited computational power, circular elements in two-dimension were used to model the granular materials in the early discrete element analysis (e.g. Cundall and Strack, 1979; Cundall, 1989; Ting *et al.*, 1989; Bathurst and Rothenburg, 1990; Bardet and Proubet, 1991; Iwashita and Oda, 1998). The studies showed that insights into the micro mechanisms governing the response of real granular materials can be obtained from two-dimensional simulations. However, laboratory tests clearly showed that the responses for two-dimensional and three-dimensional particles under similar boundary conditions are different (Thomas, 1997). Spherical elements have been widely used in recent years as computational power has increased (e.g. Thornton, 2000; Suiker and Fleck, 2004; Cui and O'Sullivan, 2006). More valuable information was obtained from these three-dimensional simulations, as they more readily relate to real granular materials.

In fact, natural grains (e.g. sand and gravel) normally have an irregular shape. Mitchell (1993) pointed out that it is typical for sands to have more than half of their particles with a ratio of length to width more than 1.4. Irregularly shaped particles can provide interlocking and extra moment resistance (i.e. resistance to rotation). The perfectly circular/spherical shape of the idealised particles makes them tend to roll excessively. As a result, a lower overall strength for an assembly of circular/spherical particles was commonly observed. Besides, sphericity also has a significant effect on the volumetric strain and the maximum dilation angle

(Frossard, 1979). The problem of excessive rolling in numerical simulations has been demonstrated by many researchers (e.g. Ting *et al.*, 1989; Bathurst and Rothenburg, 1990; Bardet and Proubet, 1991; Ng and Dobry, 1992). Different approaches have been tried to overcome the problem of using discs or spheres. Two major methods used to simulate the effect of particle shape are presented in the following subsection.

3.3.1 Restrain the rotation of individual particles

Ting *et al.* (1989) showed that realistic soil behaviour can be obtained in discrete element simulation when particle rotation is restrained artificially. A similar approach was used by Ng and Dobry (1992, 1994) to simulate the mechanical behaviour of sand under monotonic and cyclic loading. Based on studies of shear bands in laboratory and numerical simulations, Iwashita and Oda (1998) and Oda and Kazama (1998) indicated that rotational resistance to rolling for each particle is one of the factors controlling the strength and dilatancy of granular soils. They suggested that rotational resistance should be activated at contact points in the discrete element modelling. A modified distinct element method (MDEM) was, therefore, developed by Iwashita and Oda (1998). In addition to contact-stiffness model and slip model, a rolling model, which comprises an elastic spring, a dashpot, a no-tension joint and a slider, is installed at each contact point in MDEM, as shown in Figure 3.4. Iwashita and Oda (1998) used MDEM to investigate the effect of rolling restriction. The results showed that a higher peak and ultimate shear strength and clear void localization were observed by restricting the particle

rotations, compared with simulations using free rolling particles, as shown in Figure 3.5.

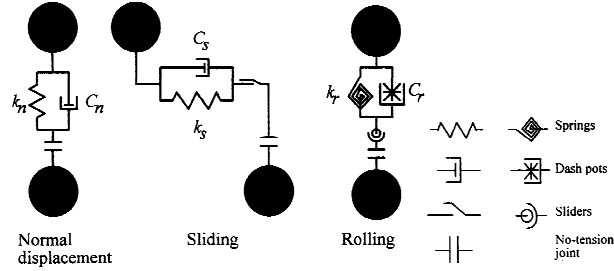


Figure 3.4. Contact model in MDEM (Iwashita and Oda, 1998).

Recently, Suiker and Fleck (2004) conducted a series of triaxial test simulations to investigate the effect of particle rotation and interparticle friction. They found that both friction angle ϕ' and dilatancy angle ψ_d increase when particle rotation is restricted and that the differences in the friction angle ϕ' and dilatancy angle ψ_d for free particle rotation samples and restricted particle rotation samples become more marked with increasing interparticle friction angle ϕ'_μ , as shown in Figure 3.6.

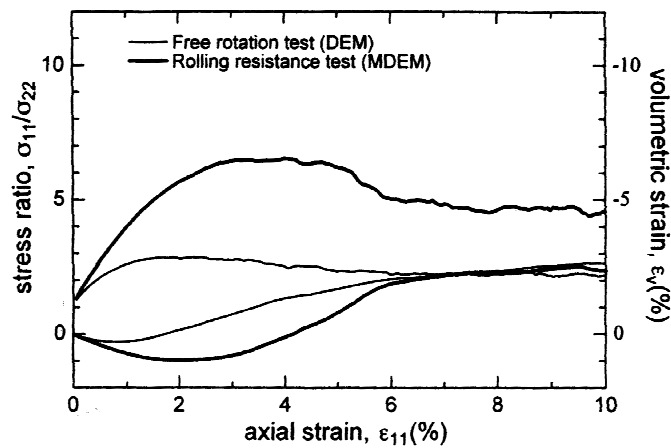


Figure 3.5. Effect of particle rolling resistance on stress-strain behaviour and volumetric change (contraction positive) (Iwashita and Oda, 1998).

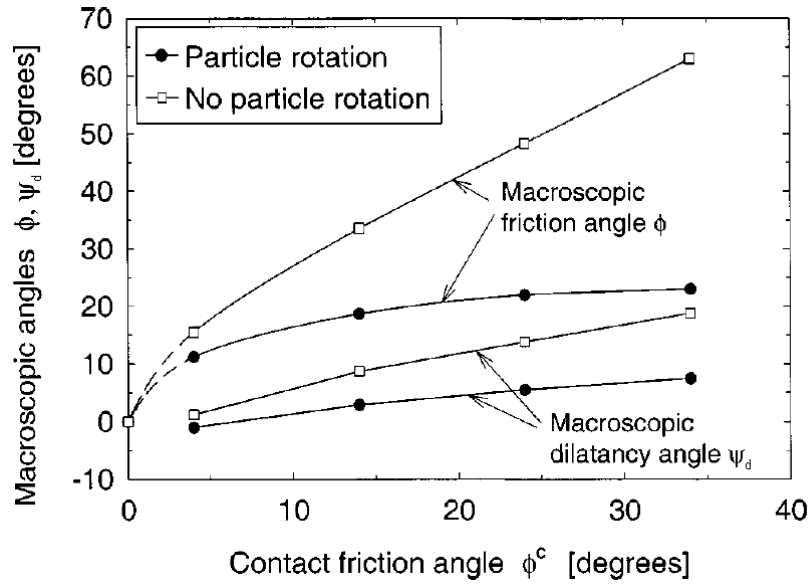


Figure 3.6. Interparticle friction angle ϕ'_μ against friction angle ϕ' and dilatancy angle ψ_d at steady-state collapse (at deviator strain = 0.05) (Suiker and Fleck, 2004).

3.3.2 Using non-circular/spherical particles

The drawback of MDEM is that the numerical parameters of rotational resistance are difficult to relate to any observable physical quantity. Particle shape determines the distribution and magnitudes of the contact forces, and particle interlocking due to the angularity of particles significantly affects the mechanical behaviour. However, these cannot be modelled by restraining rotation of circular/spherical particles. Oda *et al.* (1985) indicated that more fabrics are possible at the microscopic level with non-spherical particles and that simulations based on circular particles may be too idealised to capture the shape characteristic of soil behaviour. The approach which reduces the effect of the numerical idealization by using more accurate shape of granular materials was developed by

many researchers (e.g. Rothenburg and Bathurst, 1992; Lin and Ng, 1997; Favier *et al.*, 1999; O'Sullivan and Bray 2003; Ni *et al.*, 2000; Powrie *et al.*, 2005).

Rothenburg and Bathurst (1992) employed two-dimensional elliptical particles with eccentricity e ranging from 0 to 0.25 to model real sand behaviour. They found that the main difference in the mechanical behaviour of assemblies between elliptical particles and discs are the strength characteristics. And they showed that assemblies of elliptical particles had similar qualitative features as real sands. The stress-strain behaviour for ellipses with different eccentricities is shown in Figure 3.7. Rothenburg and Bathurst (1992) also found that the coordination number decreased with both decreasing eccentricity and increasing shear strain, as shown in Figure 3.8. Similar results were found in three-dimensional simulations (e.g. Lin and Ng, 1997; Ng, 2001). A higher peak and ultimate shear strength, larger initial stiffness, more dilation and less particle rotation for elliptical particles than spherical particles were observed by Lin and Ng (1997) when they investigated the behaviour of assemblies of elastic ellipsoidal particles in triaxial test simulations. In addition, they found that the assembly of ellipsoidal particles achieved lower porosity and larger coordination number under the same consolidation procedure.

Favier *et al.* (1999) reported a method, namely the multisphere method, to represent non-spherical particles using overlapping spheres which are fitted to the surface contour of the real particle shape. The approach has been used to approximate ellipsoidal particles using four identical overlapping spheres placed on the major and minor axes of the particle (Vu-Quoc *et al.* 2000, Zhang and Vu-Quoc, 2000, and Favier *et al.* 2001) as shown in Figure 3.9. In the same year,

Thomas and Bray (1999) used a disc cluster (which is a group of circular discs permanently connected to form an irregularly shaped particle) to represent the shape of real grains. They simulated biaxial shear tests and anchor pull-out tests using these disc clusters. The results showed that disc clusters exhibited less tendency to rotate excessively and that computation speed did not decrease significantly. Thomas and Bray (1999) showed that specimens with more realistic fabrics (i.e. particle arrangement and orientation) can be created by using disc clusters and reported that peak internal friction angles ϕ'_{peak} increased 12.5° (from 22.5° to 35°) when using disc clusters instead of single discs with free rotation, as shown in Figure 3.10.

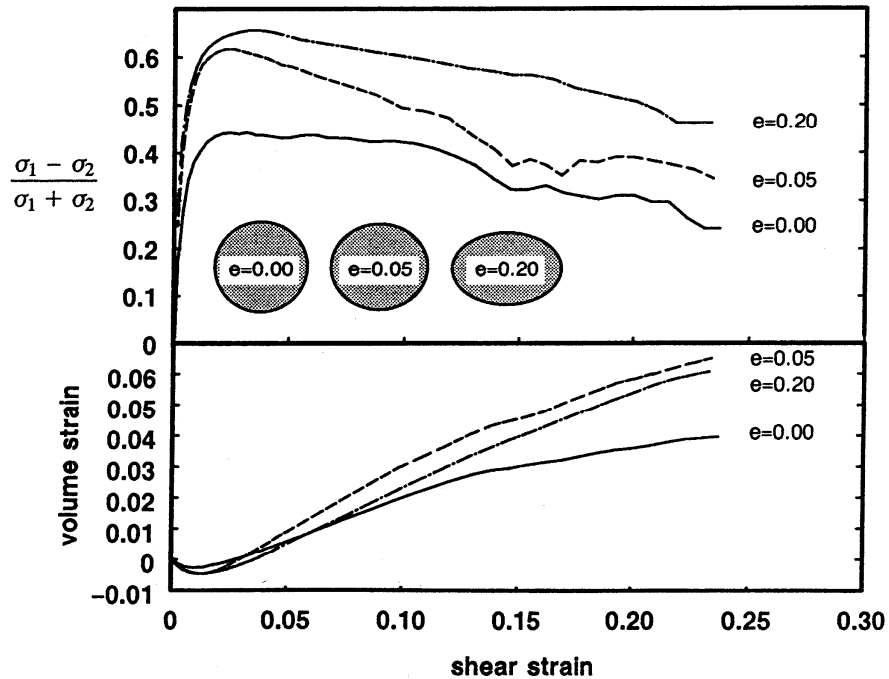


Figure 3.7. Stress-strain behaviour during biaxial compression (Rothenburg and Bathurst, 1992).

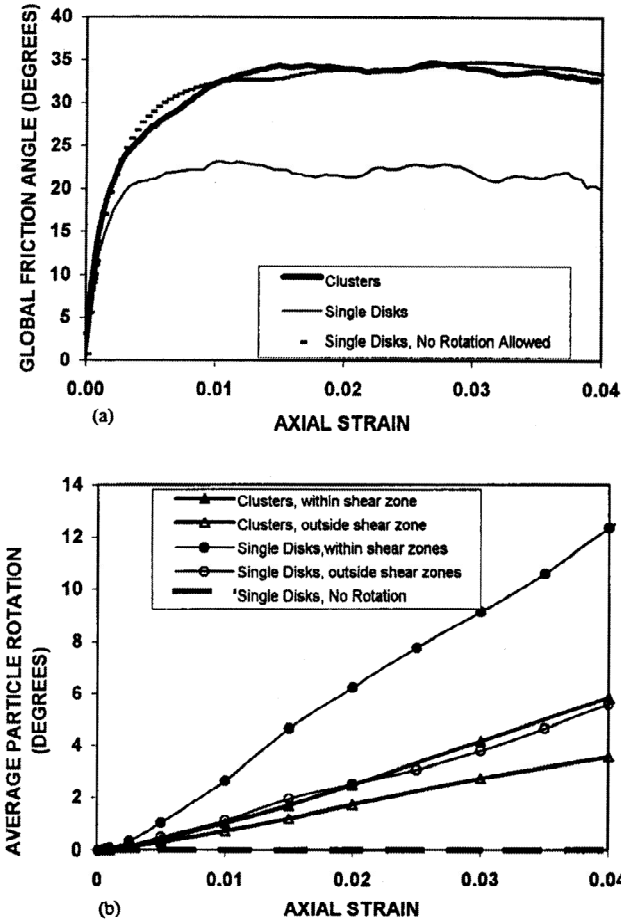


Figure 3.10. (a) Stress-strain response and (b) average particle rotation in biaxial shear tests (Thomas and Bray, 1999).

Ni *et al.* (2000) and Powrie *et al.* (2005) studied the effect of applied stress, initial sample porosity, particle shape and interparticle friction on the behaviour of sand using DEM. Each soil grain was modelled as two spheres bonded together (an “agglomerate”) with a high strength parallel bond (as shown in Figure 3.12) in their simulations. They defined the particle shape factor as $(R + r) / R$, where R and r are the radii of the larger and smaller spheres, respectively. They found that the deformation and shear strength of the assembly are a function of the particle

shape factor. With increasing the shape factor, both the peak and ultimate shear strength increased. The overall dilation of the sample during the simulations increased significantly and the degree of particle rotation reduced significantly with increasing particle shape factor. Ni *et al.* (2000) found that the shear strength of the assembly with shape factor greater than 1.7 was higher than that of single spheres with rotation prevented. They concluded that restraining rotation of spherical particles cannot capture the effect of interlocking provided by particle shape.

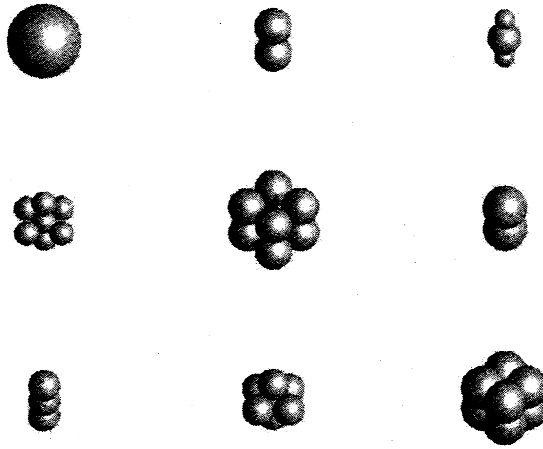


Figure 3.11. Axisymmetric sphere clusters (O’Sullivan and Bray, 2003).

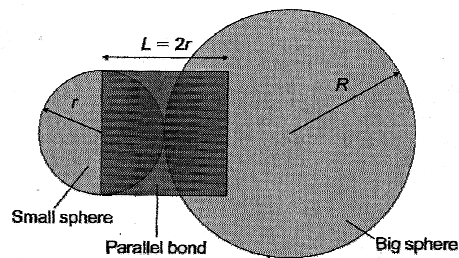


Figure 3.12. Schematic illustration of a bonded particle. The diameter of the parallel bond is the same as the diameter of the smaller sphere (Powrie *et al.*, 2005).

Since the angularity of railway ballast particle tends to be much more than that of most sand particles, modelling the shape characteristic of ballast particle is significantly important in the discrete element modelling of railway ballast. Lim and McDowell (2005) used both spheres and eight-ball cubic clumps representing railway ballast particle in the simulations of box test and showed that the eight-ball clumps give much more realistic behaviour due to particle interlocking. Similar findings were reported by McDowell *et al.* (2006) in the simulations of monotonic triaxial tests on railway ballast. Details are presented in section 3.6.

3.4 Influence of Interparticle Friction Angle

Skinner (1969) said that when the interparticle friction is high, particle rolling dominates the volume change; when the interparticle friction is low, sliding dominates the volume change. Suiker and Fleck (2004) observed that both internal friction angle ϕ' and dilatancy angle ψ_d increased with increasing interparticle friction angle ϕ'_μ in triaxial test simulations, as shown in Figure 3.13. However, when the interparticle friction was high ($\phi'_\mu > 25^\circ$), the internal friction angle ϕ' and dilatancy angle ψ_d levelled off. They concluded that the relative proportion of interparticle rolling to sliding increased with increasing interparticle friction angle ϕ'_μ . A similar conclusion was drawn by Liu and Matsuoka (2003) when they conducted simple shear test simulations using circular discs.

Ni (2003) investigated the effect of interparticle friction angle ϕ'_μ in direct shear test simulations using spheres and two bonding spheres, respectively, as described in section 3.3.2. He reported that the interparticle friction significantly affected

both peak strength and volumetric dilation of the assemblies. He found that for the samples composed of spherical particles, the interparticle friction angle φ'_μ did not affect the ultimate strength; whereas, for the samples composed of two bonding particles the ultimate strength increased with increasing interparticle friction. Hence, particle shape and interparticle friction together affect the ultimate strength of an assembly. Ni (2003) also reported that for both the assembly of spheres and the assembly of two-ball agglomerates, a higher degree of particle rotation was observed when the particle friction angle φ'_μ is higher.

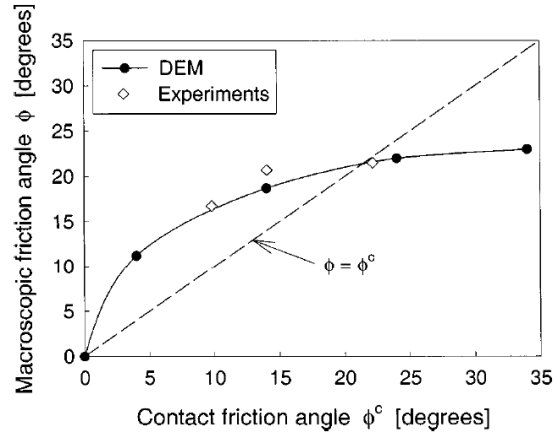


Figure 3.13. Interparticle friction angle φ'_μ versus internal friction angle φ' for DEM and experimental results (Suiker and Fleck, 2004).

3.5 Modelling of Particle Breakage

Two methods have been proposed to model particle breakage in DEM. One is to treat each granular particle as a porous agglomerate built by bonding smaller particles (Robertson, 2000; McDowell and Harireche, 2002a; Cheng *et al.*, 2003; and Lim and McDowell, 2005). The other solution is to replace the particle with

an equivalent group of smaller particles when the original particle fulfils a predefined failure criterion (Lobo-Guerrero and Vallejo, 2005). Details of these methods are presented as follows:

The fracture of soil grains was first modelled by Robertson (2000) using PFC^{3D}. In his studies, each particle was modelled as a porous agglomerate of balls bonded together with contact bonds. Three different packings (e.g. hexagonal close packing (h.c.p.), face-centred cubic packing (f.c.c.) and body-centred cubic packing (b.c.c.)) were investigated. Robertson (2000) found that results for h.c.p. agglomerates with random rotation were more repeatable than for the other packings. He also found that a Weibull distribution of bond strengths was best reproduced by removing balls at random from the h.c.p. agglomerate to simulate flaws and that scaling ball contact stiffness and bond strength by the same factor f resulted in failure at the same strain at a fracture force scaled by f .

Following Robertson (2000), McDowell and Harireche (2002a) used realistic particle parameters and applied gravity to stabilise the agglomerate prior to loading in order to replicate experiments of crushing of silica sand particles. Figure 3.14 shows the agglomerate in single particle crushing test simulation. They showed that it is possible to reproduce the right average strength of agglomerates as a function of size and the correct statistical distribution of strengths for a given size, so that the strengths followed the Weibull distribution.

McDowell and Harireche (2002b) then used these agglomerates to model one-dimensional compression tests on silica sand. The results from these simulations

showed that yielding coincided with the onset of bond fracture, consistent with the hypothesis by McDowell and Bolton (1998) that yielding is due to the onset of particle breakage.

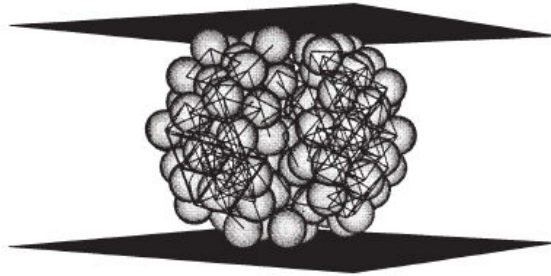


Figure 3.14. Final fracture of a typical 0.5 mm diameter agglomerate, showing intact contact bonds (McDowell and Harireche, 2002a).

Lobo-Guerrero and Vallejo (2005) developed a method to model particle crushing in two-dimensional simulations. In their method, they assumed that the breakage criterion applies only to a particle having a coordination number smaller than or equal to three and that the real loading configuration (as shown in Figure 3.15(a)) is equivalent to that obtained in a diametrical compression test (as shown in Figure 3.15(b)). When the internal tensile stress of the disc is greater than its tensile strength, the disc is fractured into eight smaller discs, as shown in Figure 3.15(c).

3.6 Modelling Mechanical Response of Railway Ballast Using DEM

Since railway ballast in the track generally comprises large particles of typical size approximately 40 mm, it is difficult to treat such a material as a continuum. DEM

provides insight into the micro mechanical behaviour of railway ballast. The mechanical behaviour of railway ballast in various test conditions has been simulated by many researchers (Lim and McDowell, 2005; McDowell *et al.*, 2006; Lobo-Guerrero and Vallejo, 2006; and Hossain *et al.*, 2007). This section will review recent work on discrete element modelling of ballast.

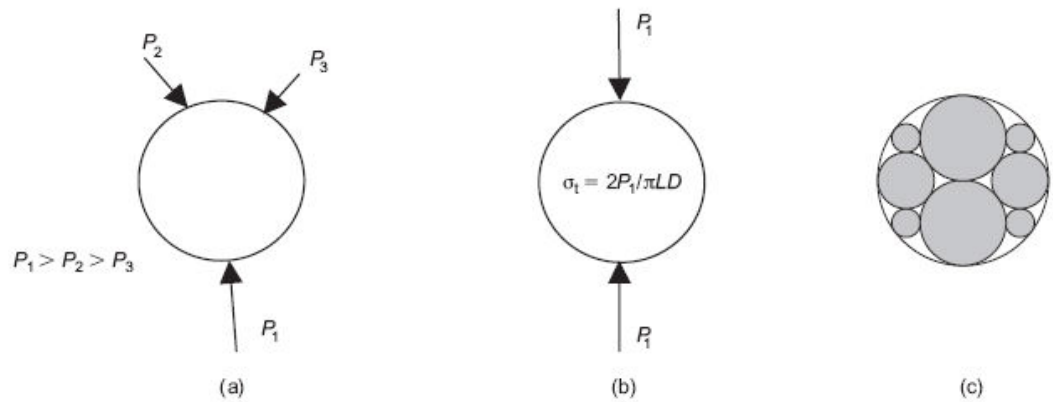


Figure 3.15. Idealisation of the induced tensile stress and arrangement of the produced fragments (Lobo-Guerrero and Vallejo, 2005).

Lim and McDowell (2005) carried out a series of simulations on single particle crushing tests for railway ballast using agglomerates of bonded balls. In their simulations, they showed that the distribution of strengths correctly followed the Weibull distribution and that the size effect on average strength was consistent with that measured in the laboratory. Lim and McDowell (2005) also simulated oedometer tests on crushable ballast particles using agglomerates of bonded balls. Compared with experimental results, they found that the yield stress for the agglomerates was less than that for the real ballast. They indicated that the difference of results between laboratory tests and simulations was due to the

spherical shape of the agglomerates, which led to columns of strong force in the simulated sample.

Box tests (as mentioned in section 2.6.2) were simulated by Lim and McDowell (2005) to study the mechanical behaviour of ballast subjected to traffic loading. Spheres and eight-ball clumps were used to represent each ballast particle to ascertain whether interlocking of ballast can be modelled and whether the particle shape influences the resilient and permanent deformation of the ballast. They found that the eight-ball clumps can provide particle interlocking and give more realistic mechanical behaviour under repeated loading. A similar conclusion was drawn by McDowell *et al.* (2006) when they used both spheres and eight-ball cubic clumps in simulations of large-scale triaxial experiments. McDowell *et al.* (2006) pointed out that, as breakage was not considered in their simulations, comparing with the experimental results (Indraratna *et al.*, 1998), dilation rather than contraction was observed at high confining pressures.

Lobo-Guerrero and Vallejo (2006) studied the effect of crushing on railway ballast in a simulated track section by using a circular disc to represent each single ballast particle. Two hundred cycles of loading were applied to the circular disc aggregate through three simulated sleepers. The method of modelling particle crushing developed by Lobo-Guerrero and Vallejo (2005), as mentioned in section 3.5, was used in their simulations. They found that permanent deformation increased considerably when particle crushing was included and that particle crushing was concentrated underneath the simulated sleepers, as shown in Figure 3.16. However, the effect of particle shape was not considered in their simulations.

Recently, Hossain *et al.* (2007) studied the effect of angular ballast breakage on the stress-strain behaviour of railway ballast under different confining pressures using biaxial test simulations. Two dimensional angular shaped clumps were used in their simulations to model particle interlocking. Similar to the method introduced by Lobo-Guerrero and Vallejo (2005), particle crushing was simulated by releasing discs from the clump when the internal tensile stress induced by contact forces was greater than or equal to 10 MPa. Hossain *et al.* (2007) showed that particle breakage had significantly effect on both the axial strain and the volumetric strain.

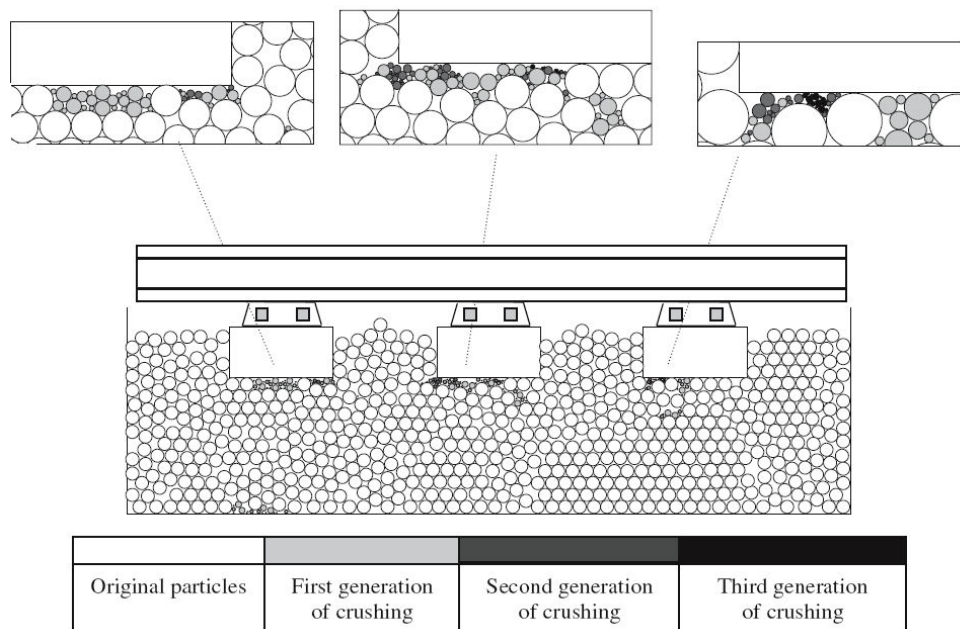


Figure 3.16. Details of the unloaded sample of crushable ballast after 200 cycles (Lobo-Guerrero and Vallejo, 2006).

3.7 Summary

DEM is a powerful tool for fundamental research into the behaviour of granular materials. The basic concepts and general mathematical backgrounds of DEM and PFC^{3D} have been presented. Some specific features (e.g. bonding models and clump logic) in PFC^{3D} have been described. Circular/spherical particles tend to roll excessively and lead to a lower strength of the assembly. Restraining rotation of individual particles and using non-circular/spherical particles are the main approaches to overcome the problem of excessive rolling when using circular discs or spheres. Both peak and ultimate shear strength can be increased by restraining the rotation of circular/spherical particles in an assembly. However, the numerical parameters of rotational resistance are difficult to relate to any observable physical quantity, and restraining rotation of circular/spherical particle cannot simulate the effect of particle interlocking. Higher shear strength can be obtained by using non-circular/spherical particles to model the effect of particle shape and particle interlocking. Interparticle friction also affects the stress-strain behaviour and volumetric change of an assembly. Both friction angle ϕ' and dilatancy angle ψ_d increase with increasing interparticle friction angle ϕ'_μ (i.e. $\phi'_\mu < 25^\circ$), but then level off with further increase in interparticle friction angle. Two main methods have been presented to model particle breakage in DEM. One is to treat a grain as a porous agglomerate built by bonding smaller particles. The other is to replace the particles that fulfil a predefined failure criterion with an equivalent group of smaller particles. The simulated mechanical behaviour of railway ballast in various test conditions has been discussed. The studies indicated that it is

necessary to simulate particle interlocking in modelling of mechanical behaviour of railway ballast. In the triaxial test simulations, dilation rather than contraction was observed at high confining pressures. This indicated that it is necessary to consider the particle breakage in the simulation of railway ballast. The effect of crushing on the railway ballast in two-dimensional simulations of ballasted track has been reported. The studies showed that the influence of particle breakage on the settlement and volumetric strain observed in the simulations was significant.

CHAPTER 4

IMPORTANCE OF MODELLING BALLAST PARTICLE SHAPE

4.1 Introduction

Previous research (e.g. Cheng *et al.*, 2004; Harireche and McDowell, 2003; Lim and McDowell, 2005; McDowell *et al.*, 2006) has shown some success in simulating the behaviour of granular materials using DEM. The use of PFC^{3D} (Itasca, 1999) to model crushable particles using bonded agglomerates has been described in detail by Robertson (2000), McDowell and Harireche (2002), Cheng *et al.* (2003), and Lim and McDowell (2005). Lim and McDowell (2005) investigated the use of DEM for modelling railway ballast subjected to single particle crushing tests, oedometer tests and box tests involving cyclic loading by a simulated railway sleeper. They found that DEM was capable of simulating particle fracture and particle interlock. In their single particle crushing test simulations and oedometer test simulations, particle fracture was achieved by bonding small balls together to form agglomerates of ballast-sized particles, whilst in the box test simulations clumps of overlapping balls were used to reduce computational time. However, the clumps used in the box test simulations were

simple cubic clumps of eight spheres, so the clump shape did not resemble that of a real ballast particle. Previous studies (Ting *et al.*, 1989; Ng and Dobry, 1992; Rothenburg and Bathurst, 1992; and Favier *et al.*, 1999) have shown that particle shape has a great influence on the mechanical behaviour of granular materials and that using spheres to represent each grain is not enough for granular materials comprising angular particles.

This chapter presents a simple procedure used to model ballast particle shape by using many overlapping balls of different sizes to form complex clumps resembling real ballast particles. The parameters affecting the clump shape are described and examples of clumps using different parameters are presented. In addition, the distribution of contact forces is examined in an aggregate of spheres and two alternative aggregates of clumps created using different parameters, in order to show the effect of the particle shape on the inhomogeneous stresses induced within the particle assembly. The result of the application of a cycle of load in a box test on clumps is compared with that for a box test on spheres and the effect of the particle shape on contact force distribution, particle displacement and particle rotation is studied.

4.2 Modelling Ballast Particle Shape

4.2.1 Modelling procedure

Figure 4.1 shows a typical real ballast particle. The aim is to model such a complex shape using DEM. For this purpose, overlapping balls are used to form

clumps using a simple procedure which gives control over the sphericity, angularity and surface texture of the clump.



Figure 4.1. Typical full-sized ballast particle.

A ball is created at the centre of a cubic cell to form the main body of the clump. Fourteen directions are created: six orthogonal to the cube faces (i.e. in positive and negative directions along each orthogonal axis), and eight along the cube space diagonals, as shown in Figure 4.2. All balls in the clump are created within a virtual sphere with a radius R_v . Along each direction, it is possible to generate balls to form the clump; however, the directions of ball generation are chosen at random, and not all directions might be employed. First, either only the six directions orthogonal to the cube faces are chosen for possible ball generation, or all 14 directions are chosen as possibilities. The likely number of directions used for ball generation is chosen as n and the probability p that a particular direction might be used is then $n/6$ if only the directions orthogonal to the cube spaces are used as possible directions, and $n/14$ if the space diagonals are also used. For each direction then, a random number r is drawn from uniform distribution in the range $[0.0, 1.0]$. If r is less than or equal to p , then this direction is chosen to generate

balls. The number of balls generated in each direction is set directly. Figure 4.3 shows the ball generation process in one direction. The radius of the second ball formed is less than the radius of the first one. The difference in the radii of successively generated balls is a uniformly distributed random variable in the range $[0.0, c]$, where c is the maximum possible difference and is chosen directly. In this way, the angle subtended by the common tangents to successively generated spheres, is created at random, and the maximum angle is controlled partly by c (see below). Figure 4.4 shows the clump geometry and generation along a typical direction x . The centre of the second ball is derived from the centre of the first one and reduction in radius. The first ball with radius R_1 is centred at $A(x_1, y_1, z_1)$ and the second ball with radius R_2 is centred at $B(x_2, y_2, z_2)$. The angle 2α is the angle subtended by the two common tangents to the spheres. It can be seen that

$$x_2 = x_1 + D_1 \quad (4.1)$$

$$y_2 = y_1 \quad (4.2)$$

$$z_2 = z_1 \quad (4.3)$$

$$R_1 = D_1 + D_2 \quad (4.4)$$

$$R_2 = D_2 + D_3 \quad (4.5)$$

$$R_1 - R_2 = D_4 \quad (4.6)$$

where D_4 is the reduction of radius in the range $[0.0, c]$.

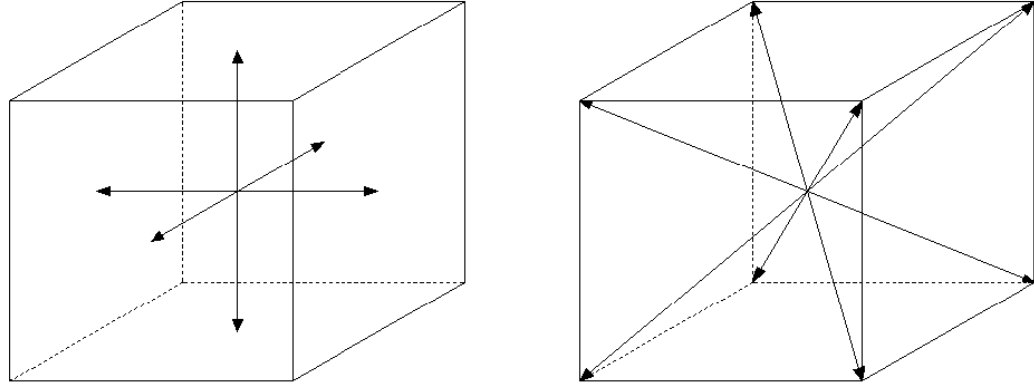


Figure 4.2. Directions of ball generation for clumps.

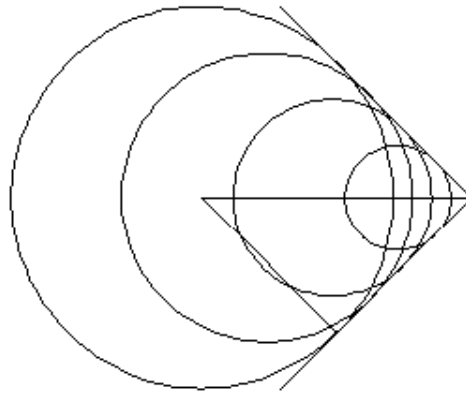


Figure 4.3. Ball generation along one direction.

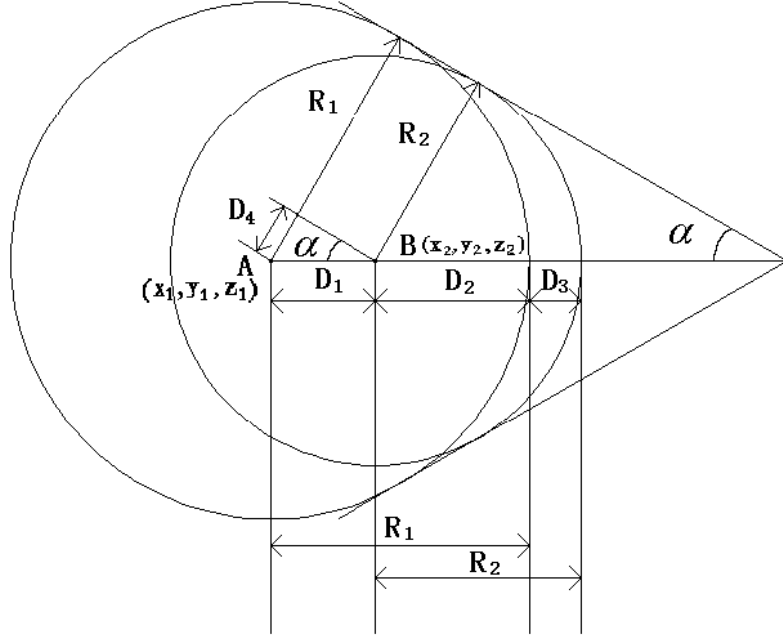


Figure 4.4. Definition of clump geometry.

Substituting Equations 4.4 and 4.5 into Equation 4.6 yields

$$D_1 = D_3 + D_4 \quad (4.7)$$

Substituting Equation 4.7 in Equation 4.1:

$$x_2 = x_1 + D_3 + D_4 \quad (4.8)$$

where D_3 is the clump extension parameter and is constant and is chosen by the user.

The relationship between D_4 , D_3 and α is given by

$$\sin \alpha = \frac{D_4}{D_3 + D_4} = (1 + D_3/D_4)^{-1} \quad (4.9)$$

The parameters D_3 , c (and hence D_4), and the number of balls generated along each direction each has an influence on the sphericity of the particle. The ratio D_3/D_4 controls the angle α which will influence the sphericity depending on the number of balls used. Figure 4.5 shows the effect of using different values of α to generate clumps, shown for a constant value of D_3 . In Figure 4.5 the value of α and hence D_4 is constant for each generated ball and the maximum permissible number of balls have been shown; in the simulations described in subsection 4.2.2 below, the value of D_4 is a uniformly distributed random variable in the range $[0.0, c]$ and is chosen at random for each ball generated. A high sphericity would be achieved with a low value of D_3 , a high value of D_4 , and a small number of balls. The value of D_4 and the number of balls used also influences the angularity since this will determine the size of the smallest ball. Using a large number of balls with small extension D_3 can be used to produce flatter particle surfaces.

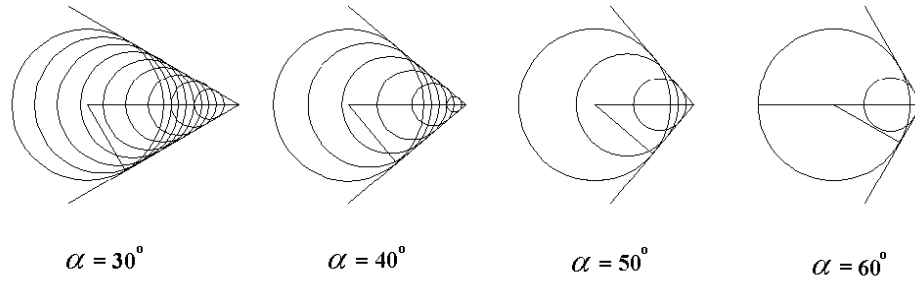


Figure 4.5. Effect of angle α on clump geometry.

After all the selected directions for ball generation have been used, balls are used to link up outermost balls of adjacent directions in order to form edges of the clump. A line is used to join the outermost balls, and a series of balls inserted in

between, as shown in Figure 4.6. The radii of these balls vary linearly from one outermost ball to the other, and the number of such balls for each edge, set directly, affects the fineness or surface texture of the modelled ballast particle. The greater the number of balls used in each edge, the more ‘realistic’ the clump.

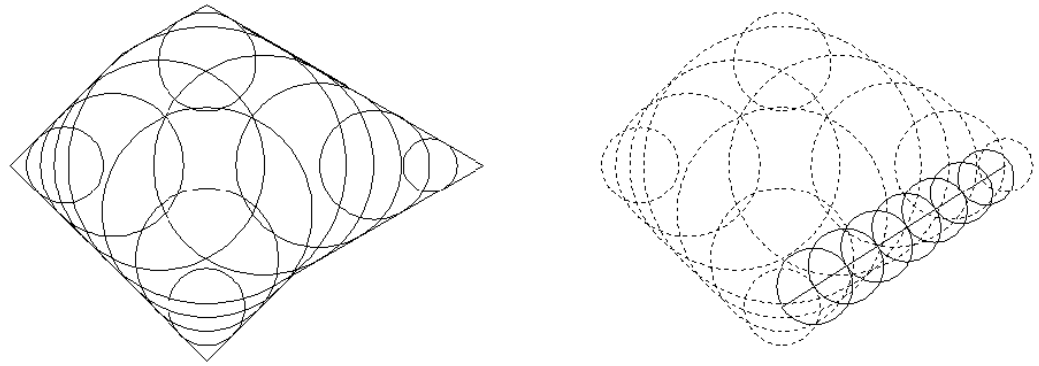



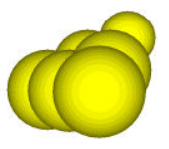
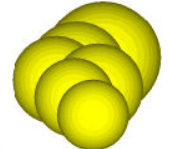
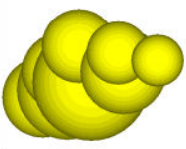
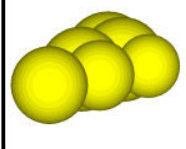
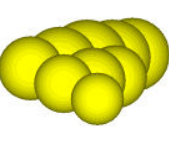
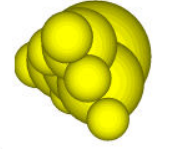

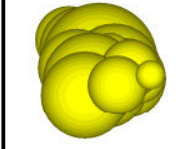
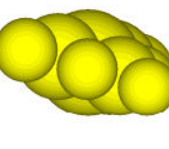
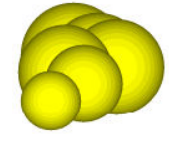
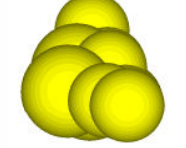
Figure 4.6. Formation of edge of clump.

4.2.2 Results

Table 4.1 shows the parameters used for five different samples of clumps. Figures 4.7-4.11 show some examples of the clumps formed using these parameters. It can be seen that realistic clumps can be formed by choosing a small extension between the clumps D_3 and large maximum value c in the reduction in ball size D_4 , which is chosen at random for each generated ball; this tends to give large values of α and serves to produce simulated ballast which is reasonably equi-dimensional as is required by the Railtrack Line Specification for track ballast in the UK (RT/CE/S/006 Issue 3, 2000).

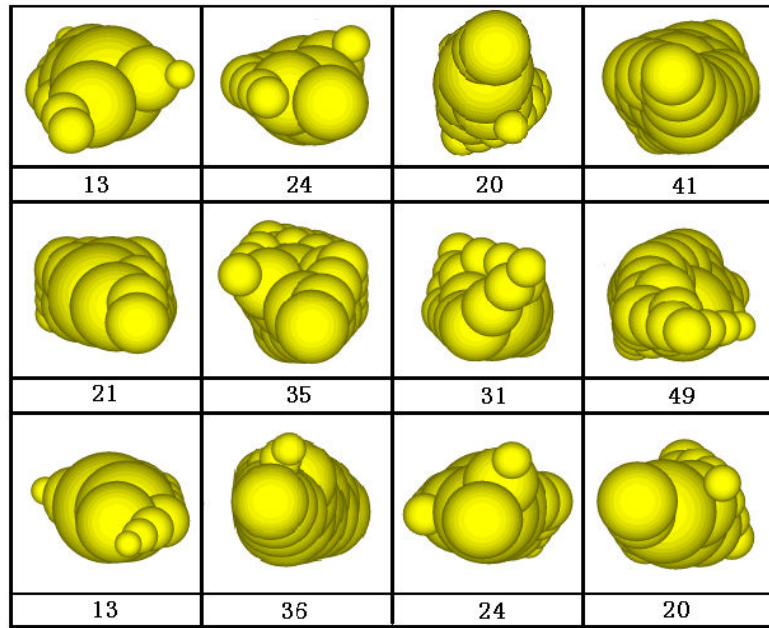
Shape parameters	Sample 4.1	Sample 4.2	Sample 4.3	Sample 4.4	Sample 4.5
Number of directions of ball generation	6	14	14	14	6
Probability of the number of directions of ball generation used, p (%)	50	50	50	40	80
Maximum number of balls in each direction	2	2	2	2	2
Maximum reduction of radius in each direction, c	$0.2R$	$0.5R$	$0.2R$	$0.4R$	$0.5R$
D_3	$0.2R$	$0.2R$	$0.2R$	$0.2R$	$0.5R$
Number of balls used in each edge	1	2	2	2	2

Table 4.1. Parameters for clumps in different sample.

			
9	6	6	8
			
6	9	13	13
			
13	9	6	9

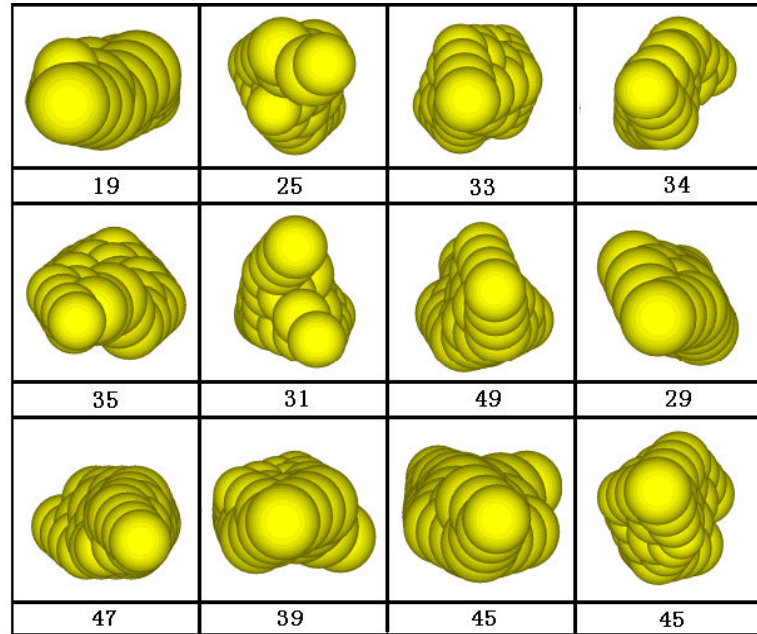
Average number of balls in clump = 8.92

Figure 4.7. Typical clumps generated for Sample 4.1 (refer to Table 4.1 for parameters).



Average number of balls in clump = 27.25

Figure 4.8. Typical clumps generated for Sample 4.2 (refer to Table 4.1 for parameters).



Average number of balls in clump = 35.92

Figure 4.9. Typical clumps generated for Sample 4.3 (refer to Table 4.1 for parameters).

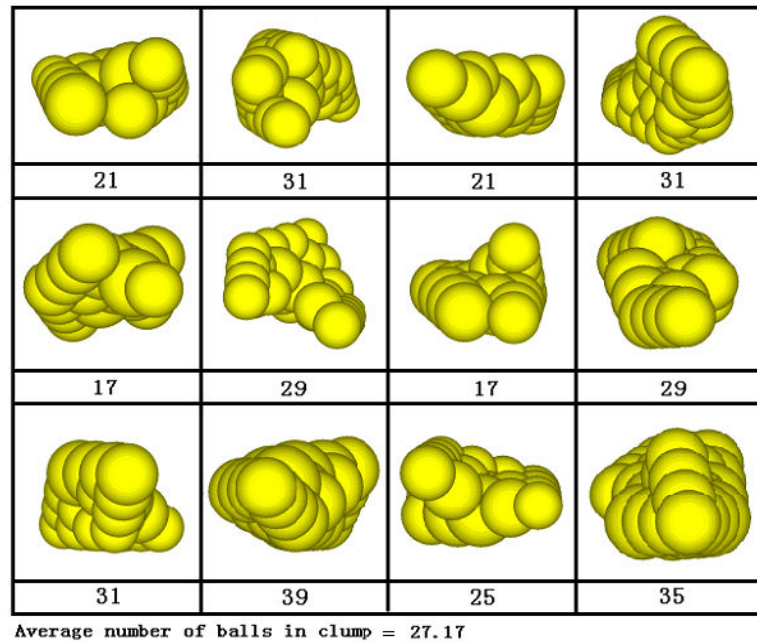


Figure 4.10. Typical clumps generated for Sample 4.4 (refer to Table 4.1 for parameters).

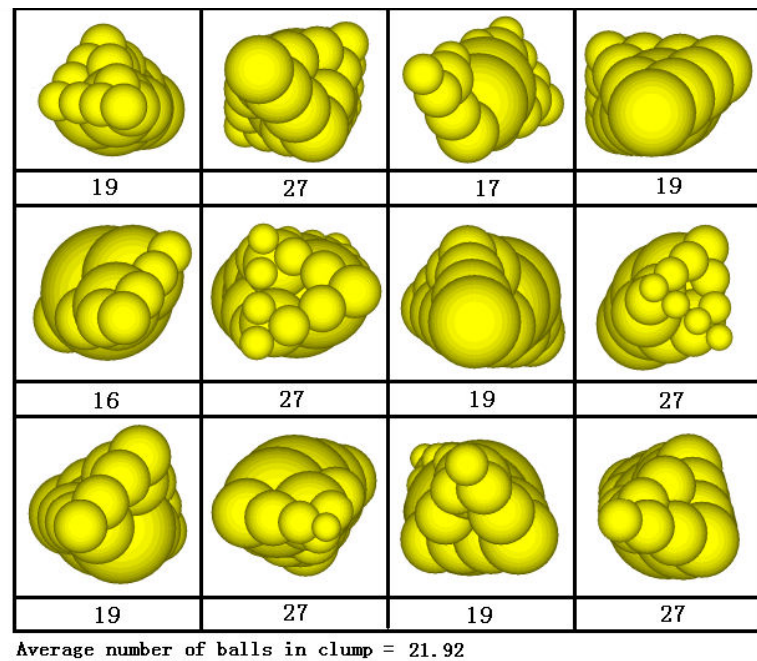


Figure 4.11. Typical clumps generated for Sample 4.5 (refer to Table 4.1 for parameters).

4.3 Box Test Simulations Using Unbreakable Irregular Shaped Particles

4.3.1 Modelling procedure

McDowell *et al.* (2004) described box tests on ballast involving applied cyclic load to a simulated sleeper on ballast in a box of dimensions 700 mm \times 300 mm \times 450 mm. The test set-up is shown in Figure 2.20. Lim and McDowell (2005) described discrete element modelling of this ballast using a sphere to represent each ballast particle, and also using a simple eight-ball cubic clump. Following Lim and McDowell (2005), box tests were simulated using the new clumps developed in section 4.2, to examine the effect of clump shape on the distribution of contact forces and also the cyclic response of the aggregate.

Figure 4.12 shows the simulated box test arrangements for the spheres, Samples 4.1 and 4.2. The box has dimensions 700 mm \times 300 mm \times 450 mm. Figure 4.12(a) shows the box with 1936 spheres, each of diameter 36.25 mm prior to loading. The sample was compacted by enhanced gravity and reducing gravity to 9.81 m/s² towards the end of the compaction stage. In order to make particle compact easier and reduce computational time for the compaction process, a low friction coefficient was used. However, frictionless balls were not used as it was found that it took the spheres a long time to stabilise after compaction, even with the default local non-viscous damping active. Therefore, during the compaction process, the coefficients of friction for the spheres, sleeper, walls and base were set to be 0.3. During subsequent loading, the friction coefficients were set equal to

0.5. The normal and shear stiffnesses (linear-elastic) of the spheres were set to be 5.08×10^9 N/m and the stiffnesses of the sleeper and walls were set to have the same values. Since in box test the Young's modulus of stiff rubber is approximately 2,000 times smaller than that of steel (Ashby and Jones, 1980), the stiffnesses of the simulated rubber base were set to 2.54×10^6 N/m (which is 2,000 times smaller than that of value for the walls). The density of the spheres was $2,600 \text{ kg/m}^3$.

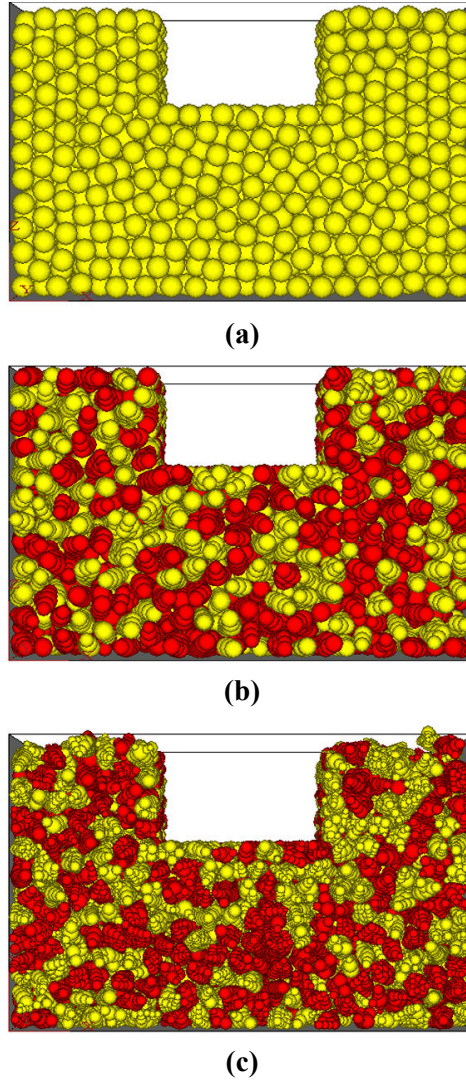


Figure 4.12. Box test on (a) spheres, (b) Sample 4.1 and (c) Sample 4.2.

The clumps were formed by creating small initial spheres, expanding to a diameter of 36.25 mm and cycling to equilibrium. “Virtual spheres” were then created by deleting the initial spheres and creating a virtual space by multiplying the initial sphere diameter by a factor of 1.26 for Sample 4.1 and 1.31 for Sample 4.2. Each “virtual sphere” formed the outermost possible boundary for each clump and the clumps were created within the “virtual spheres”. Figure 4.12(b) shows Sample 4.1, containing 1,770 clumps (17,642 balls) and Figure 4.12(c) shows Sample 4.2 with 1,995 clumps (65,591 balls). For the clumps, the stiffnesses and coefficients of friction used were the same as for the simulated box tests on spheres. Similar to the compaction procedure for the spheres, during compaction the coefficient of friction of the balls was set to 0.3, and increased to 0.5 after compaction.

It should be noted that for the clumps, since balls overlap, the total volume of balls in a clump is greater than the volume of the clump and the mass of the clump is therefore greater than the mass of an equivalent clump with a uniform density; such an entity is currently not available within PFC^{3D}. Where there is overlapping of balls within a clump, there is a contribution to the mass in the overlapping region from each of the overlapping balls. This may not influence the mechanical behaviour of the clumps under static loading. However, when the dynamic effect of the clumps is significant, the influence of mass due to overlapping balls will become significant. The mass of overlapping balls also affects the moments of inertia of the clump since the mass is not uniformly distributed within the clump. Thus, a modified density was used in each clump. In order to achieve the desired mass, the modified density ρ_m is derived from the initial density ρ_o as

$$\rho_m = \frac{V_{clump} \cdot \rho_o}{\sum V_i} \quad (4.10)$$

where V_i is the volume of the i^{th} ball in the clump and V_{clump} is the volume of the clump and

$$\sum V_i = \sum V_i^{overlap} + V_{clump} \quad (4.11)$$

where $\sum V_i^{overlap}$ is the volume of overlap in the clump. This procedure produces clumps with the correct mass but with a non-uniform density. Due to the difficulty in calculating the volume of each clump, and since the geometry of each clump is different, the volume of a clump in Equation 4.10 was approximated to be equivalent to the volume of a sphere of diameter 36.25 mm (i.e. the volume of the sphere created before expanding to create a virtual sphere to contain the clump). The use of clumps having non-uniform density because of overlapping mass means that the dynamics of the clumps are only approximately correct. Since the balls of the clump produced following the procedure described in section 4.2 locate around the first generated sphere, with smaller degrees of overlap occurring further from that sphere, the location of the centre of mass of the clump is very close to the centre of mass of a clump with the same mass and uniform density.

For the sample of spheres, it was possible to calculate the porosity directly using a measurement sphere in PFC^{3D} (Itasca, 1999); in this way the variation in the porosity throughout the box can be studied. However, no facility is available in PFC^{3D} for calculating the porosity of a sample of clumps comprising more than

two particles within each clump. Therefore the initial porosities of the samples were estimated using a three-dimensional grid of small cubes, each of side 0.005 m, in the column directly below the sleeper and found to be 0.37 for the aggregate of spheres, 0.35 for Sample 4.6 and 0.37 for Sample 4.7.

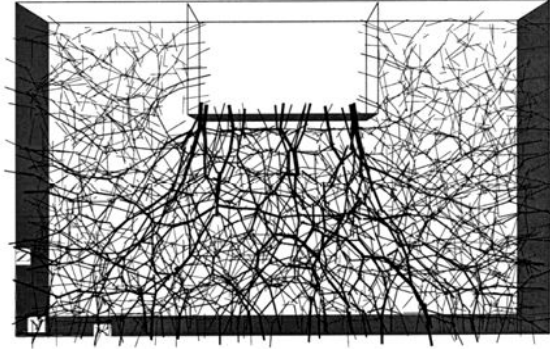
The spheres and Sample 4.1 were loaded using a sinusoidal load pulse with a minimum load of 3 kN and a maximum load of 40 kN, at a frequency of 3 Hz (following McDowell *et al.*, 2004). The required loading was maintained by PFC^{3D} servo-control mechanism (the algorithm of the servo-control mechanism can be found in the Appendix).

4.3.2 Effect of particle shape on mechanical response

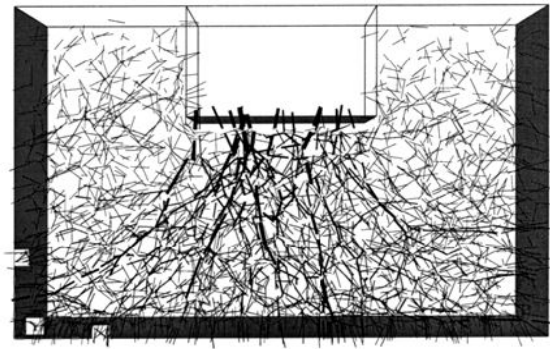
Figure 4.13 shows the contact forces for each of the three samples under self-weight after compaction by enhanced gravity and then reducing gravity to 9.81 m/s². It can be seen that the contact forces are reduced for the more angular clumps (i.e. Sample 4.2), which is in agreement with data published by Nakata *et al.* (2001) for real sands, and that the stress distribution for the spheres is more homogeneous.

Figures 4.14 and 4.15 show the contact forces for the spheres and Sample 4.1 prior to loading, at maximum load and after unloading to 3 kN respectively. It is noted that the number of contacts does not change much during the cycle of loading and unloading. The magnitude of the mean contact force for Sample 4.1 (whose shape is closer to reality comparing with those of spheres) is less than that for the spheres

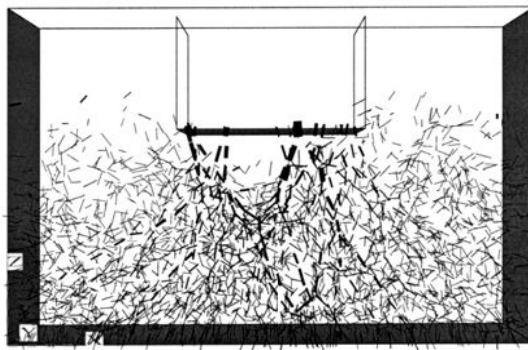
because of the higher number of contacts for Sample 4.1. It should be noted that Sample 4.1 contains flaky particles, as shown in Figure 4.7.



(a)

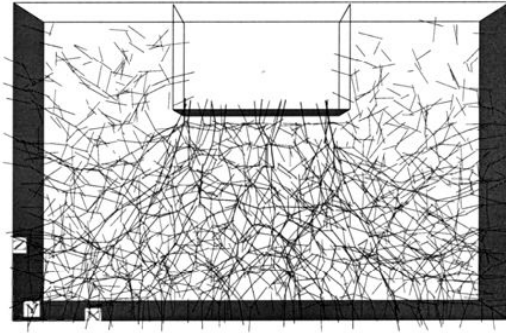


(b)

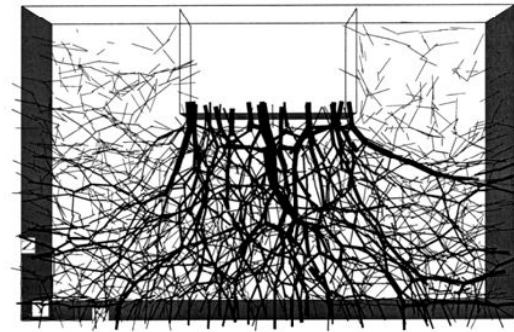


(c)

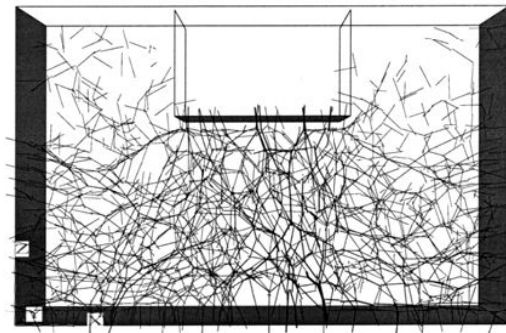
Figure 4.13. Contact forces for (a) spheres, (b) Sample 4.1 and (c) Sample 4.2 prior to loading.



(a)

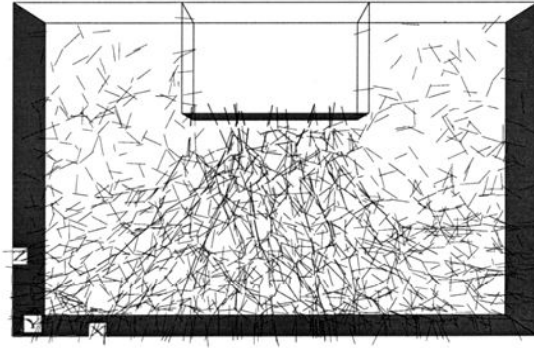


(b)

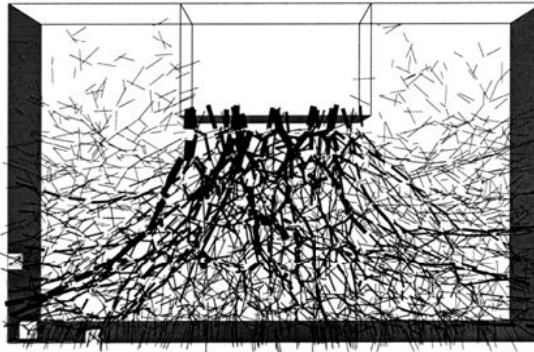


(c)

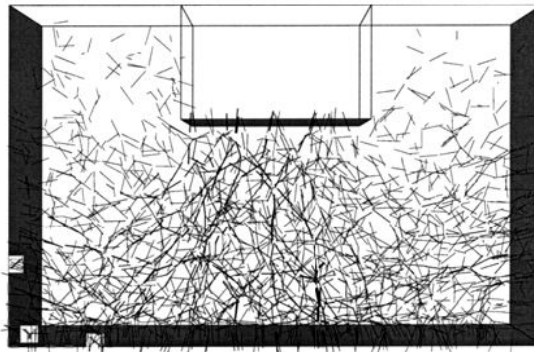
Figure 4.14. Contact forces for spheres (a) prior to loading (maximum contact force = 482N, average contact force = 29.9N, number of contacts = 10,337); (b) at maximum load (maximum contact force = 4,050N, average contact force = 336.2N, number of contacts = 10,323) and (c) after unloading to 3kN (maximum contact force = 1,012N, average contact force = 42.7N, number of contacts = 10,328).



(a)



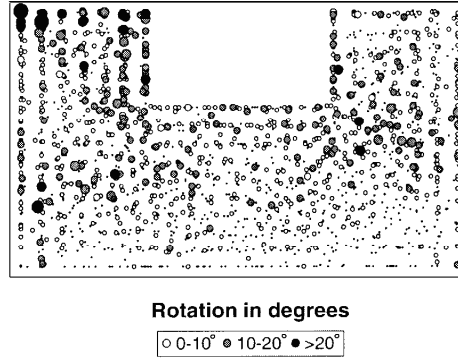
(b)



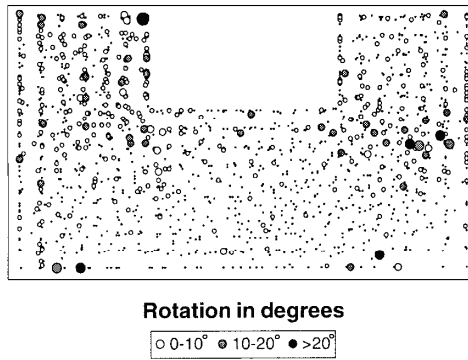
(c)

Figure 4.15. Contact forces for Sample 4.1 (a) prior to loading (maximum contact force = 374N, average contact force = 15.4N, number of contacts = 282,955); (b) at maximum load (maximum contact force = 4,233N, average contact force = 164.1N, number of contacts = 282,955) and (c) after unloading to 3kN (maximum contact force = 1,354N, average contact force = 34.4N, number of contacts = 282,955).

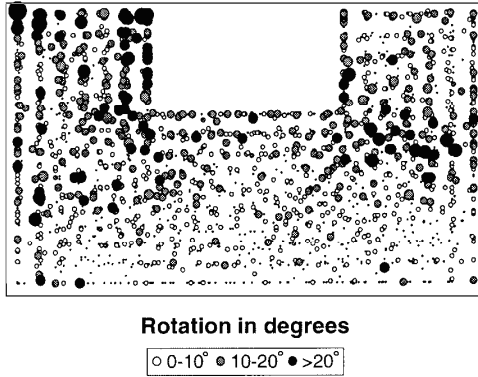
Figures 4.16 and 4.17 show the rotations of the spheres and clumps during one cycle of loading. The size of each circle is proportional to the magnitude of the particle rotation, calculated as the vector sum of the rotations about three mutually orthogonal axes. The grey circles reflect a rotation of 10° - 20° for the spheres and 0.1° - 1° for the clumps in Sample 4.1. Solid black circles indicate larger rotations of $>20^{\circ}$ for spheres and $>1^{\circ}$ for clumps. For the sample of spheres, it is clear that the main particle rotations occur near the corner of the sleeper and both sides of the sleeper. Less rotation occurs directly below the sleeper. In Sample 4.1, the distribution of the rotations is quite uniform except for a few particles which have relatively large rotations, and the average particle rotation is much less than for the spheres. The magnitude of the average rotation of the spheres after the complete cycle of loading and unloading is almost equal to the summation of the magnitudes of the average rotation during loading and during unloading separately. Similarly, the magnitude of the maximum rotation after the load-unload cycle is much greater than that at maximum load. This shows that spheres continue to roll in the same sense even on unloading. However, in Sample 4.1 the magnitude of the average particle rotation of the clumps after the complete cycle of loading and unloading is similar to that at maximum load, and it can be seen that the maximum rotation after the load-unload cycle is much less than that at maximum load. This indicates that for the clumps, some particles must have rolled in the opposite sense by a significant amount on unloading. Thus the influence of three-dimensional particle shape can be seen in providing interlock and thus reduced particle rotation. The multiple contacts between clumps give increased rolling resistance.



(a)

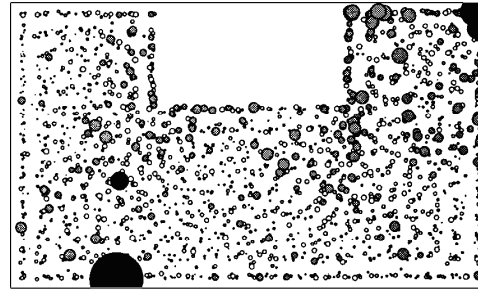


(b)



(c)

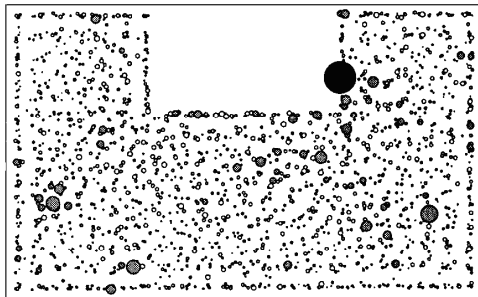
Figure 4.16. Rotations of spheres (a) during loading (maximum rotation = 48.3° , average rotation = 5.18° ; (b) during unloading (maximum rotation = 26.5° , average rotation = 2.92°) and (c) after the complete cycle of loading and unloading (maximum rotation = 63.2° , average rotation = 7.25°).



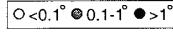
Rotation in degrees



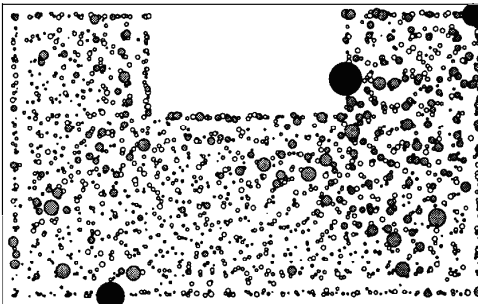
(a)



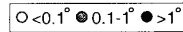
Rotation in degrees



(b)



Rotation in degrees



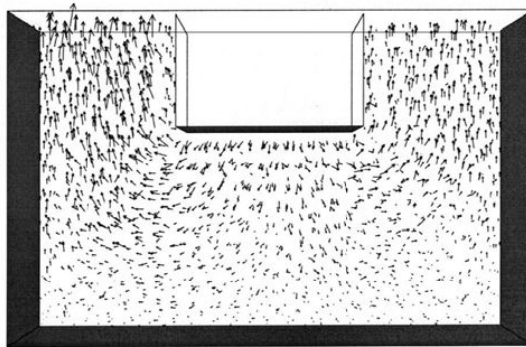
(c)

Figure 4.17. Rotations of clumps in Sample 4.1 (a) during loading (maximum rotation = 8.89° , average rotation = 0.061°); (b) during unloading (maximum rotation = 3.15° , average rotation = 0.033°) and (c) after the complete cycle of loading and unloading (maximum rotation = 3.31° , average rotation = 0.062°).

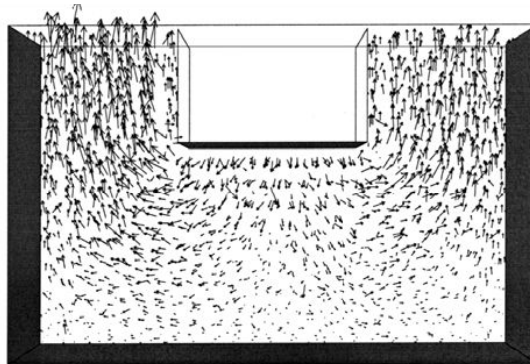
Figures 4.18 and 4.19 show the particle displacement vectors for the spheres and Sample 4.1 drawn at the same scale. Since the particle displacements for Sample 4.1 are so small, this scale has been magnified by a factor of 80 and reproduced in Figure 4.20. It can be noted that the displacements of the spheres on both sides of the sleeper are larger than those below the sleeper and the displacements are generally upwards (as shown in Figure 4.18). Comparing Figure 4.18(a) and (b), it can be noted that the spheres on both sides of the sleeper continue to move upwards on unloading. For the clumps, the behaviour is very different: the average particle displacement is greatest directly beneath the sleeper and is downwards. Comparing Figure 4.20(a) and (b), it can be seen that the clumps below the sleeper must have moved upwards during unloading. The displacements of Sample 4.1 seem closer to the response of ballast particles in the box test (McDowell *et al.*, 2004).

Figure 4.21 shows the response of the spheres and Sample 4.1 to a single cycle of load (sinusoidal, at frequency 3 Hz and maximum load of 40 kN). It can be seen that the clumps show a more realistic load-deformation response than the spheres, comparing with available data for the cyclic loading of granular materials (Lekarp *et al.*, 2000a), in which it is usually observed that axial strain does not continue to increase beyond maximum load, but rather reduces in a resilient manner on unloading. The difference in the response of the spheres and Sample 4.1 can be attributed to the interlocking provided by the three-dimensional clumps, which affects the rolling resistance and particle displacements, as shown in Figures 4.16-4.20. This is consistent with three-dimensional simulations using PFC^{3D} by Suiker

and Fleck (2004) in which they showed that restricting particle rotation may substantially increase the overall shearing resistance of the spheres. The use of clumps generated using the simple procedure described above therefore looks to be a promising tool for generating more realistic ballast particle shapes and consequently a more realistic load-deformation response.

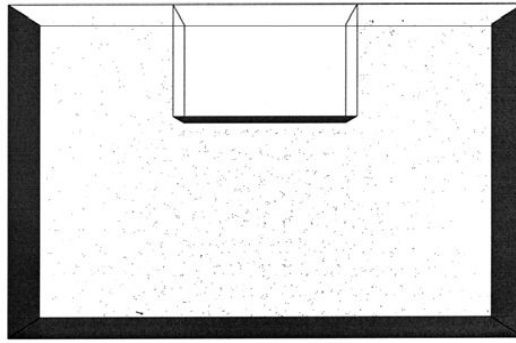


(a)

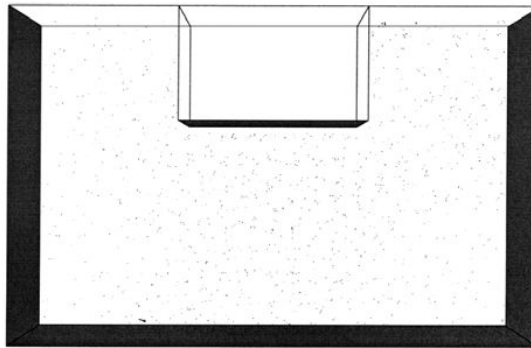


(b)

Figure 4.18. Total displacements of spheres (a) at maximum load (maximum displacement = 8.25mm) and (b) after one cycle of loading and unloading (maximum displacement = 11.79mm).



(a)



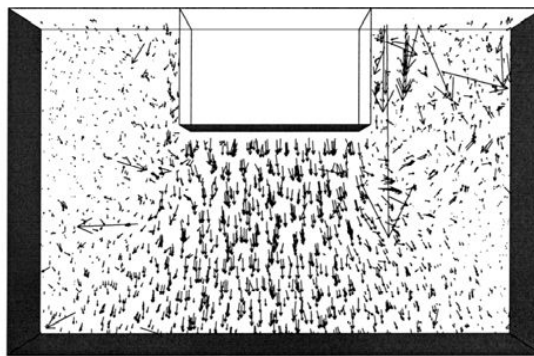
(b)

Figure 4.19. Total displacements for clumps in Sample 4.1 (a) at maximum load (maximum displacement = 2.34mm) and (b) after one cycle of loading and unloading (maximum displacement = 2.32mm).

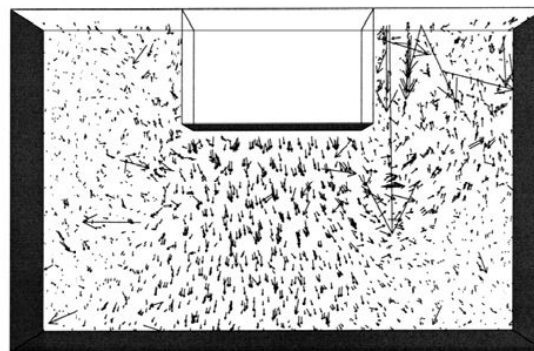
4.4 Conclusions

A simple procedure has been developed which permits the generation of clumps of spheres to simulate ballast in a realistic way. Simple parameters have been shown to allow control over the sphericity, angularity and surface roughness, and examples of various clumps generated at random using the procedure have been described. Aggregates of clumps have been generated in a box and the stresses induced by self-weight are found to become less homogeneous with increasing

angularity of the clump, in agreement with available data. The interlocking provided by the three-dimensional clumps gives much reduced particle rotations and displacements. For the spheres, deformation is concentrated at the corners and sides of the sleeper where particles flow upwards, even on unloading. For the clumps, however, deformation is concentrated directly under the sleeper where particles move downwards on loading, and then upwards by a smaller amount on unloading, giving a cyclic load-deformation response of the clumps which is found to resemble more closely the response of real ballast.



(a)



(b)

Figure 4.20. Displacement vectors of (a) Figure 4.19(a) and (b) Figure 4.19(b) magnified by a factor of 80.

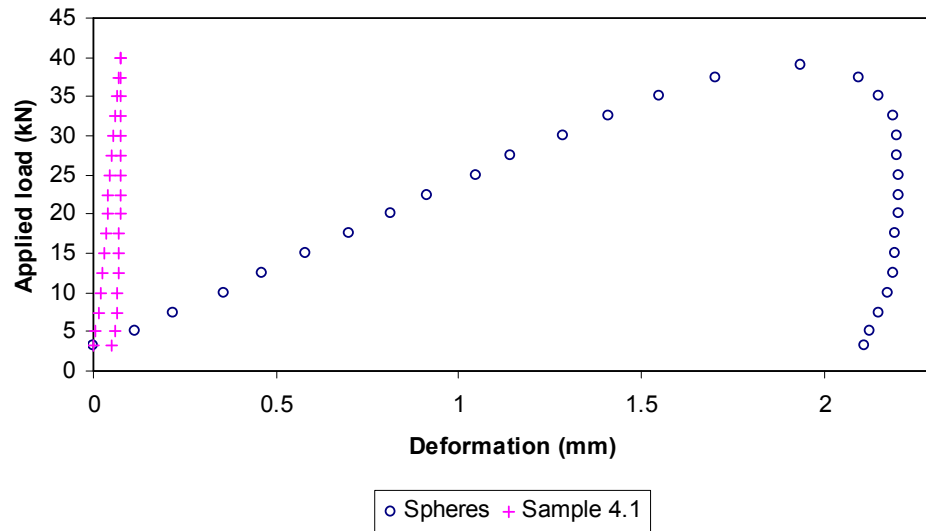


Figure 4.21. Cyclic response for spheres and Sample 4.1.

It should be noted that the work described in this chapter has been published in the form of a paper in Granular Matter (Lu and McDowell, 2007).

CHAPTER 5

DISCRETE ELEMENT MODELLING OF BALLAST ABRASION IN THE BOX TEST

5.1 Introduction

For granular materials subjected to cyclic loading, permanent axial strain accumulates linearly with the logarithm of the number of load cycles (Barksdale, 1972). Shenton (1974) showed this to be true for ballast subjected to cyclic loading in a triaxial test, and that the response of the ballast becomes approximately resilient after approximately 1,000 cycles. McDowell *et al.* (2005) conducted both box test with tamping and traffic loading and box tests with only traffic loading on ballast. Figure 5.1 shows the results from their study. ‘Traffic-only wet ballast A4’ and ‘Traffic-only wet ballast A5’ (as shown in Figure 5.1) are the samples used in the box tests with only traffic loading. ‘Wet ballast A2’ is the sample used in the box tests with tamping and traffic loading. The cumulative settlement for the ‘Wet ballast A2’ is shown as ‘Cumulative wet ballast A2’ in Figure 5.1. They found that, for box tests with only traffic loading (i.e. cyclic loading was applied to the sleeper for 10^6 cycles), the settlement of the sleeper was proportional to the logarithm of number of load cycles and that the resilient

stiffness increased towards some constant value with increasing number of cycles. They also found that most of the particle breakage was due to abrasion rather than bulk fracture, and this occurred mainly directly beneath the sleeper. Aursudkij (2007) observed similar results in the Nottingham Railway Test Facility (described by Brown *et al.*, 2007). This highlights the importance of ballast abrasion in influencing its behaviour.

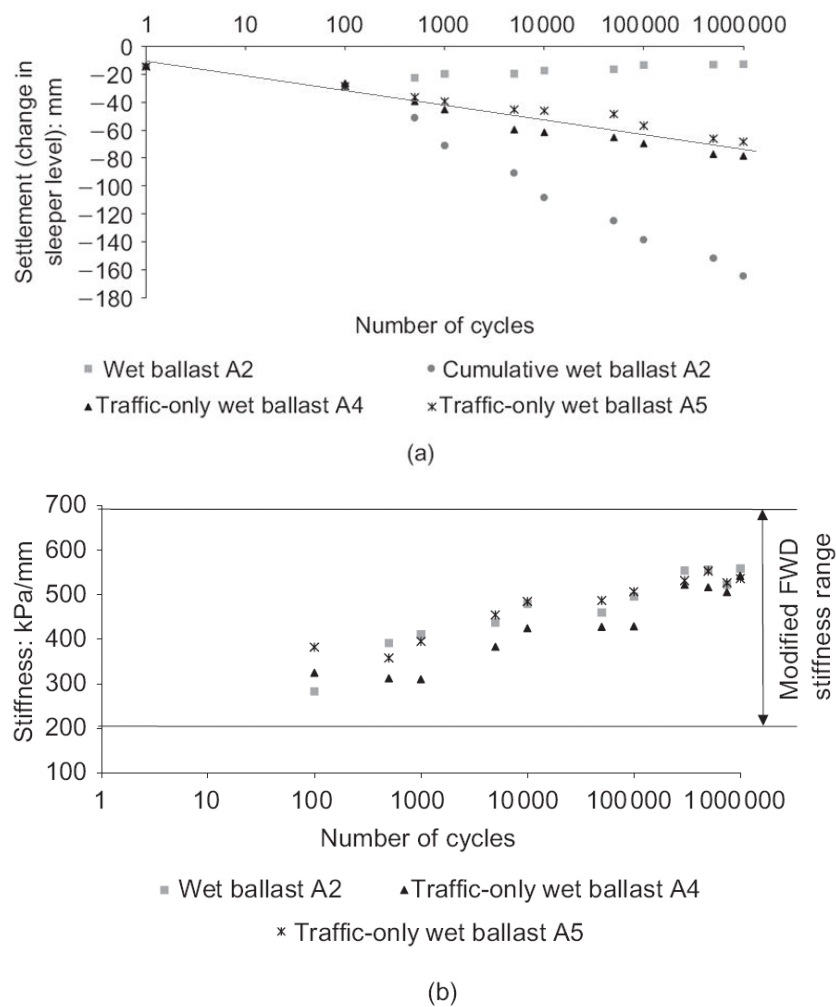


Figure 5.1. (a) Settlement and (b) stiffness plotted against number of cycles for traffic-only box test and standard box test (tamping and traffic loading) on wet ballast (McDowell *et al.*, 2005).

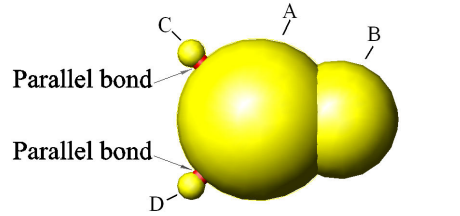
The use of PFC^{3D} to model crushable particles using bonded agglomerates of balls has been described in detail by Robertson (2000), McDowell and Harireche (2002a), Cheng *et al.* (2003) and Lim and McDowell (2005). Since it is computationally very time-consuming to use agglomerates of bonded balls to represent a large number of ballast particles in a simulation, clumps have been used to model ballast particle shape and introduce interlock in the previous chapter. However, the clumps used in those simulations were unbreakable, so particle degradation could not be investigated.

This chapter aims to show that it is possible to use DEM to model ballast abrasion correctly, and to show that ballast abrasion gives rise to the correct form of settlement response, albeit for only a small number of cycles at this stage. Asperities are introduced and bonded to the rigid clumps, so as to provide a mechanism for abrasion. Three samples of particles with different asperity bond strengths are used to examine the influence of particle abrasion (i.e. asperity fracture) during cyclic loading on settlement and stiffness.

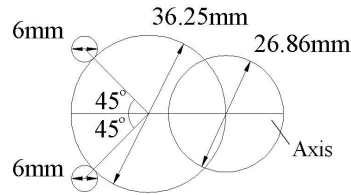
5.2 Modelling Procedure

A simple two-ball clump is used with two additional small balls (asperities) bonded at the surface, to represent a single ballast particle. Figure 5.2 shows the clump used to represent a single ballast particle, in addition to the box containing an aggregate of 1,510 of such clumps. Dimensions are such as to mimic typical ballast sized particles; the average size of the ballast particles used in the laboratory box test (McDowell *et al.* 2005) was 36.25 mm. The centre of ball B is

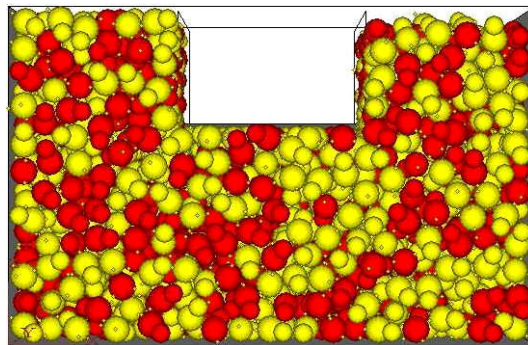
on the surface of ball A. Two smaller balls C and D of diameter 6 mm are also visible in Figure 5.2: these are the asperities.



(a)



(b)



(c)

Figure 5.2. (a) Three-dimensional particle comprising two-ball clump and two asperities; (b) clump and asperity dimensions and (c) aggregate of particles prior to cyclic loading.

It has been shown in Chapter 4 and Lu and McDowell (2007) that spheres are too simplistic to capture the real behaviour of railway ballast. However, modelling real particle shapes is computationally too time-consuming, and so the simple

clumps with bonded asperities used in this chapter can provide some degree of particle interlocking and surface damage without being too computationally inefficient. It is necessary to concede that ballast particles tend to have angular asperities, and the amount of degradation will be a function of both the strength and the angularity of the asperities. Thus this chapter presents a crude approximation to the real geometry, and is unlikely to provide sufficient damage or interlocking. An optimum ballast particle model, which provides more particle interlocking and extensive asperities breakage, will be studied in Chapters 6 and 7. In order to study the effect of abrasion on ballast behaviour, a sample was created in which balls C and D formed part of the particle clump (i.e. unbreakable ballast particle): this is Simulation 5.1. For Simulations 5.2 and 5.3, balls C and D were bonded to ball A using parallel bonds and the radii of the bond discs were 2 mm. The bond tensile and shear strengths were 500 MPa for Simulation 5.2 and 300 MPa for Simulation 5.3. The bond breaks when the tensile stress or shear stress in the bond exceeds the strength (Itasca, 1999). For the balls and walls, the normal and shear stiffnesses (linear-elastic) were 10^8 N/m. The parallel bond stiffness (uniformly distributed over the bond area) was 3.5×10^6 MPa/m, so as to give a resultant stiffness equal to that for the balls and walls. The stiffness of the simulated rubber base (subgrade) was 5×10^5 N/m and the density of the particles was $2,600 \text{ kg/m}^3$.

The procedure of sample preparation used here was the same as that described in section 4.3.1. In order to reduce computational time and prevent particle breakage occurring during this process, the particles were treated as unbreakable clumps

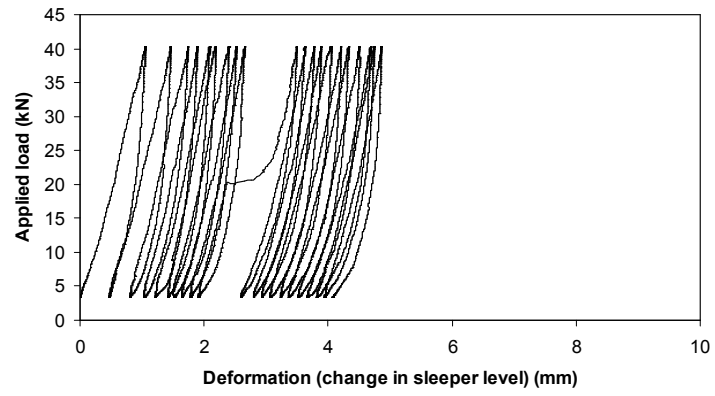
during gravitational compaction. During compaction, the ball and wall coefficients of friction were set to 0.3 (to reduce computational time as described in section 4.3.1); these were then subsequently increased to 0.8 after compaction. Once the sample had been cycled to equilibrium under a gravitational acceleration of 9.81 m/s^2 , balls C and D were released from each clump and parallel bonds were installed. The initial normal and shear strengths of the parallel bonds were set to be 100 times the final required values to prevent breakage during this transition; the strengths were then reduced gradually. Once the required bond strengths were achieved, a sinusoidal load pulse was applied with a minimum load of 3 kN and a maximum load of 40 kN at a frequency of 3 Hz (following McDowell *et al.*, 2005). It should be noted that for all three simulations, the same aggregate geometry was tested: that is, all particles were in the same positions at the start of each simulation. Twenty load cycles were applied to ballast assembly in each simulation. Because limitations in computing time make it unrealistic to perform simulations with large numbers of cycles, the purpose in this chapter is simply to demonstrate that modelling abrasion is important and necessary if the correct aggregate response is to be achieved. Mechanical behaviour of ballast assembly under large number of load cycles in triaxial test simulations will be investigated in Chapter 7.

5.3 Effect of Particle Abrasion on Mechanical Response

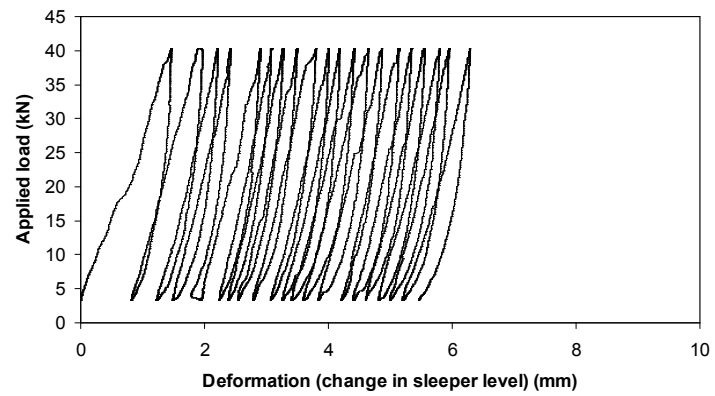
Figure 5.3 shows the position of the bottom of the simulated sleeper as a function of applied load for each of the assemblies of particles during 20 load cycles. It can

be seen that the permanent settlement continues to increase (in proportion to the number of cycles) even after 20 cycles for the uncrushable clumps, and also for the clumps in Simulation 5.2 which did not exhibit much bond breakage. It is suspected that this is due to insufficient particle interlock. It is therefore necessary here to focus on the deformation in the early stages of the test when asperity fracture dominates the behaviour of the weaker aggregate. It can be seen that, for Simulation 5.3, significant settlements occur in the early stages of the test; the rate of settlement generally reduces as the number of cycles increases up until approximately the ninth load cycle when the aggregate has stabilised.

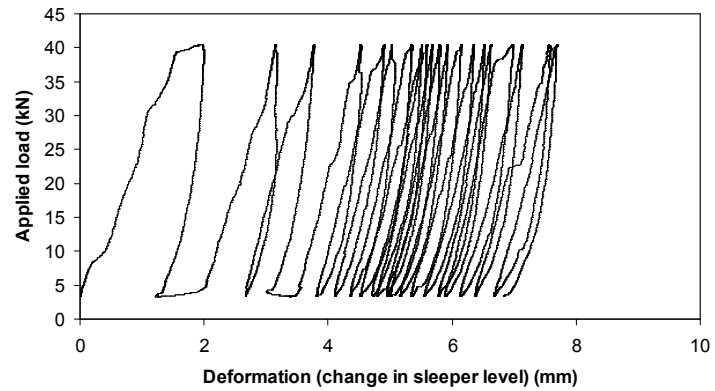
Figure 5.4 shows the number of bonds that break during the 20 load cycles for Simulations 5.2 and 5.3. For railway ballast under repeated loading, the amount of degradation must decrease with increasing number of cycles as the ballast particles become rounder and the broken asperities fall into the available voids. This sort of trend can be observed during the first 9 cycles of loading in Simulation 5.3. For Simulation 5.3, 2.52% have broken after 9 cycles and only a further 1.22% have broken in the next 11 cycles. In Simulation 5.2, only small amounts of breakage occurred, with 0.40% bonds broken after 10 cycles and 0.56% broken after 20 cycles. It can therefore be seen that the large permanent settlements in the early stages of Simulation 5.3 are associated with significant asperity breakage. A plot of permanent settlement against number of cycles is shown for each of the assemblies in Figure 5.5. The number of cycles is plotted on a linear scale in Figure 5.5(a) and on a logarithmic scale in Figure 5.5(b).



(a)



(b)



(c)

Figure 5.3. Displacement of bottom of sleeper during 20 load cycles for (a) Simulation 5.1; (b) Simulation 5.2 and (c) Simulation 5.3.

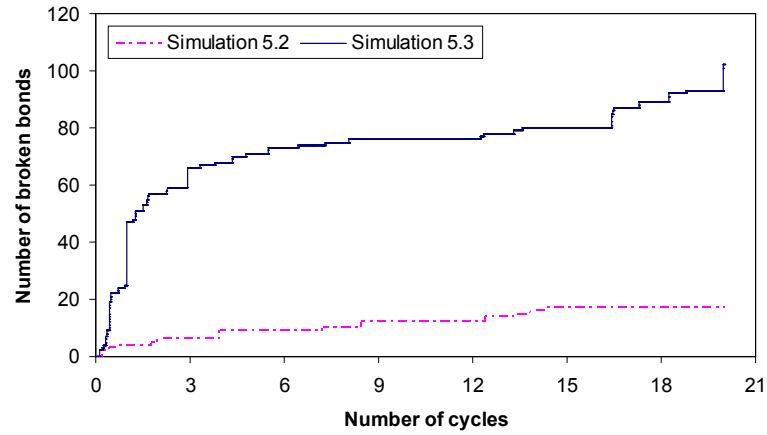
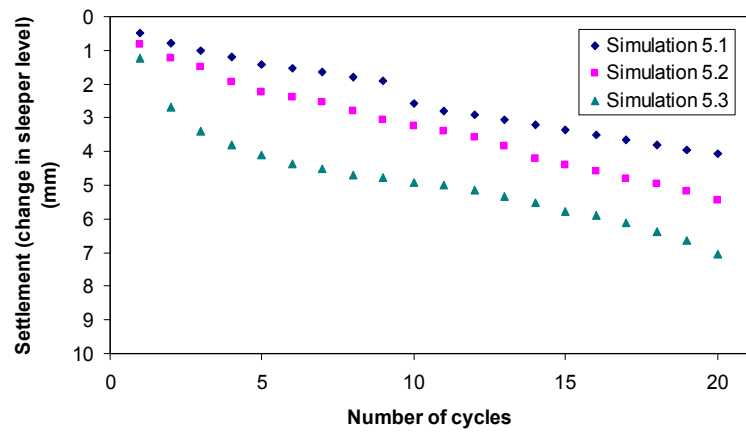
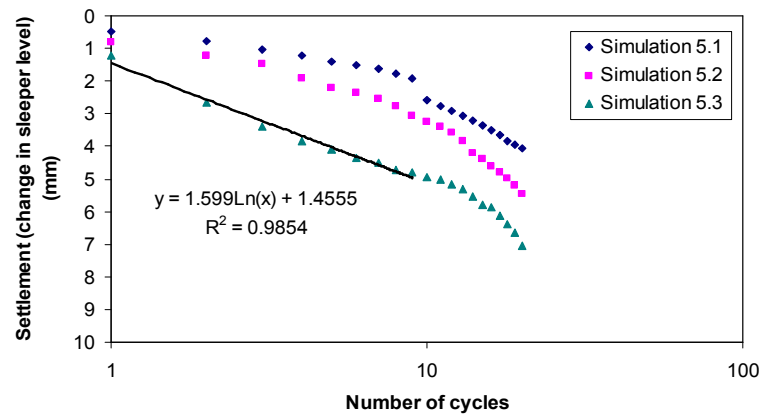


Figure 5.4. Number of broken bonds during 20 load cycles.



(a)



(b)

Figure 5.5. Settlement plotted against number of load cycles for all three simulations plotted on (a) linear scale and (b) logarithmic scale.

It should be noted that, for real ballast, settlement must be caused by rearrangement of grains, some of which will be triggered by asperity fracture. After a large number of cycles, the strong particle interlock present in real aggregates would tend to prohibit settlement without further abrasion. For Simulations 5.1 and 5.2 where little or no damage occurs, and for Simulation 5.3 after the first 9 cycles, the settlement response is approximately linear with the number of cycles; this is due to insufficient interlock given by the simplistic clumps. However, for the first 9 cycles of Simulation 5.3 in which asperity abrasion is significant, it can be seen that the settlement is approximately logarithmic with the number of cycles. Hence, it appears that a more realistic response has been achieved by permitting a significant amount of particle abrasion.

The resilient "stiffness" at any one cycle is calculated as

$$K = \frac{\sigma_{\max} - \sigma_{\min}}{\delta_{\max} - \delta_{\min}} \quad (5.1)$$

where σ relates to sleeper bearing stress and δ to sleeper displacement. Figure 5.6 shows the resilient stiffness for each of the assemblies of particles during 20 load cycles. It was found that, although for the first few cycles the stiffness increased with increasing bond strength, the stiffness of all three assemblies increased towards a steady state value of approximately 450-530 kPa/mm after 20 cycles. This is consistent with values based on falling weight deflectometer tests in the UK (McDowell *et al.*, 2005). Larger numbers of cycles are required in real ballast to achieve this steady state in which stiffness is approximately constant; it

is proposed that this is due to the large amounts of abrasion which can occur, compared with the limited amount permitted in the simulations using two bonded asperities for each clump.

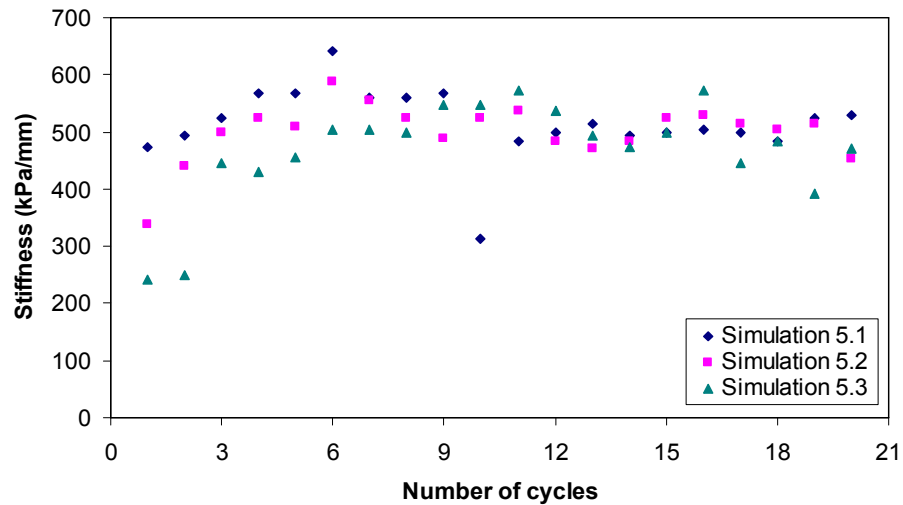
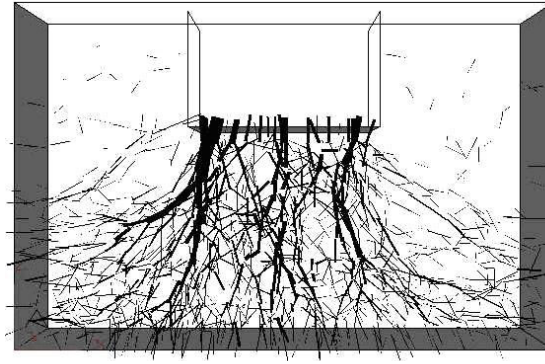
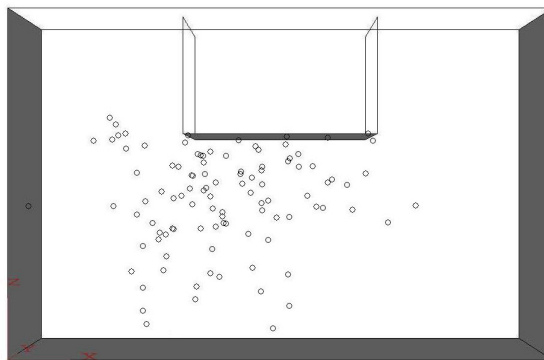


Figure 5.6. Stiffness plotted against number of load cycles for all three simulations.

Figure 5.7(a) shows a typical contact force distribution at maximum load during cyclic loading in Simulation 5.3, and Figure 5.7(b) shows the locations of where asperities break in the box during 20 load cycles for Simulation 5.3. It can be seen that particle abrasion has occurred in (and around) the main contact force chains, and that most of the abrasion has occurred beneath the sleeper, as opposed to in the crib ballast or in the ballast near the sides of the box, in agreement with the observations made from the laboratory box tests (McDowell *et al.*, 2005).



(a)



(b)

Figure 5.7. (a) Typical contact force distribution during cyclic loading in Simulation 5.3 and (b) locations of where asperities break during 20 load cycles in Simulation 5.3.

5.4 Conclusions

The abrasion of ballast particles in box test has been modelled to observe the effect of abrasion on permanent deformation. A ballast particle has been modelled as a two-ball clump with two smaller spheres bonded using parallel bonds to simulate asperities. When significant asperity breakage occurs, a realistic response is observed such that permanent settlement is related to bond breakage, and the permanent settlement is approximately proportional to the logarithm of the number

of cycles of load, albeit for only a small number of cycles. Although this observation is only confined to the first few cycles, this is believed to be due to the lack of particle interlock, in addition to the small number of asperities used. Nevertheless, this chapter has shown the importance of modelling abrasion using DEM if the correct response is to be achieved. It has also been shown that most of the particle abrasion occurs beneath the sleeper, in agreement with laboratory experiments (McDowell *et al.*, 2005). An improved ballast particle model which provides more particle interlocking and greater possibility for asperity breakage will be presented in Chapters 6 and 7.

It should be noted that the work described in this chapter has been published in the form of a paper in *Geotechnique* (Lu and McDowell, 2006).

CHAPTER 6

MONOTONIC TRIAXIAL TEST SIMULATIONS

6.1 Introduction

The monotonic triaxial test is one of the most important laboratory tests for the investigation of the mechanical behaviour of railway ballast. Indraratna *et al.* (1998), for example, performed large-scale triaxial tests on latite basalt to study the stress-strain behaviour, strength and degradation characteristics of railway ballast. The porosities of the compacted specimens were in the range from 0.44 to 0.46. The specimens were tested under various confining pressures σ_c' ranging from 15 kPa to 240 kPa (which simulate the typical confining pressures generated within ballasted track by the passage of unloaded to fully loaded trains). The key results from their study are shown in Figure 6.1. Very high principal stress ratios σ_1' / σ_3' were observed in their triaxial tests at low confining pressures. Small changes in the particle size distribution were observed in their tests and particle breakage was more pronounced at higher confining pressures.

McDowell *et al.* (2006) used an eight-ball cubic clump to represent each single ballast particle in large-scale triaxial test simulations and compared the results

with experimental results (Indraratna *et al.*, 1998). They pointed out that, as breakage was not considered in their simulations, comparing to the experimental results (Indraratna *et al.*, 1998), dilation rather than contraction was observed at high confining pressures. Chapter 5 and Lu and McDowell (2006) have shown the importance of modelling ballast abrasion in box test simulations. However, the results showed that the two-ball clump with two smaller asperities is insufficient to provide particle interlocking and extensive asperity breakage for a large number of cycles. Therefore, an improved ballast particle model is studied in this chapter.

In this chapter, the discrete element method is used to simulate the mechanical behaviour including particle abrasion of railway ballast under the monotonic triaxial test conditions and the results are compared with the experimental data (Indraratna *et al.*, 1998), so that the effects of micro properties can be related to the macro behaviour of ballast. A confining pressure of 120 kPa has been used in a series of simulations to study the effect of different factors (i.e. particle shape, particle friction coefficient and particle abrasion) on the stress-strain behaviour of railway ballast. Three different particle shapes and friction coefficients are studied first. Parallel bonds are then introduced between clumps to simulate the interlocking of very small asperities and increase the shear strength of the assembly. In addition, the effect of particle abrasion is shown by introducing bonded asperities. The stress-strain behaviour for the developed particle model for railway ballast under a range of confining pressures is then compared with that for experimental results; and the micro mechanical behaviour in the simulations is also investigated.

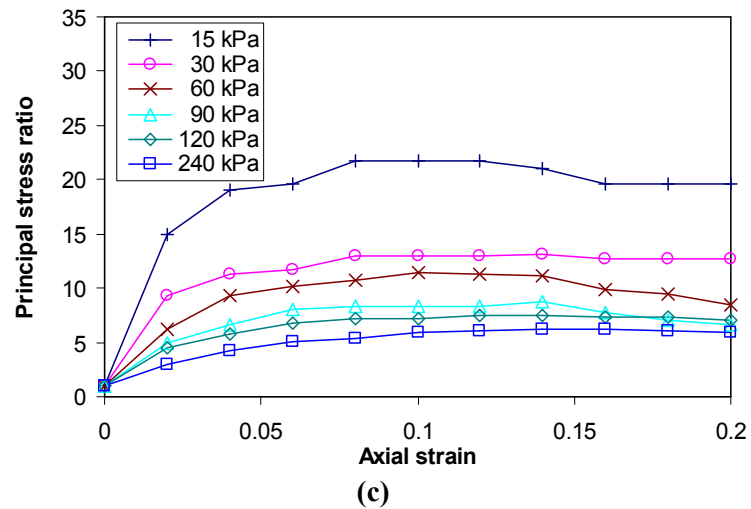
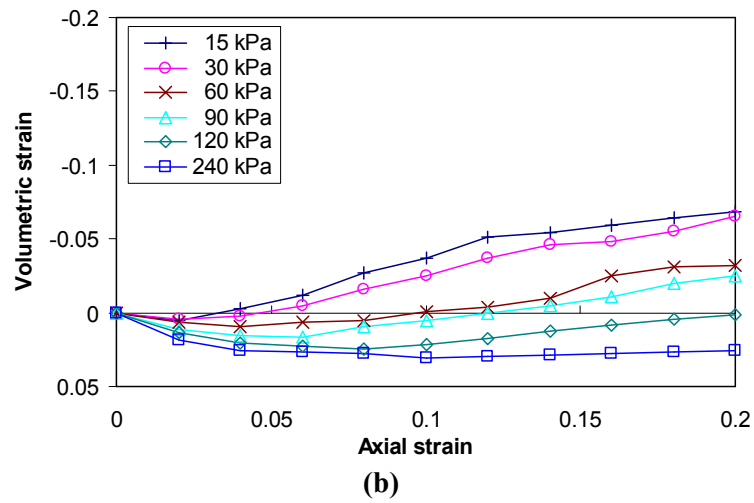
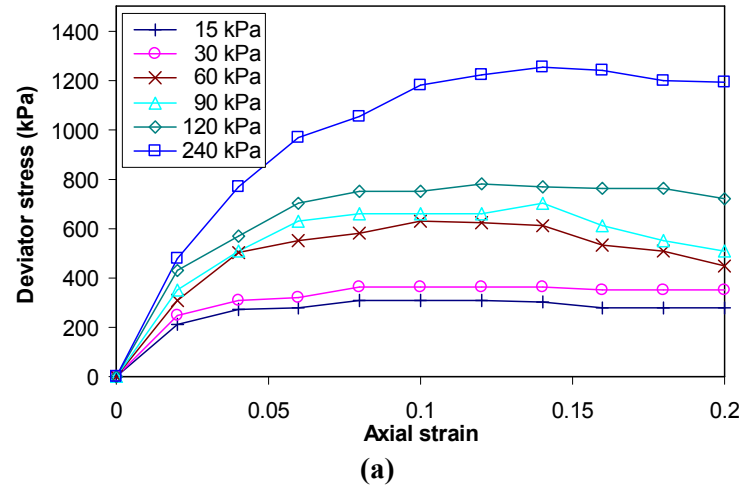


Figure 6.1. Experiment results of drained compression tests on ballast under different confining pressures (Indraratna *et al.*, 1998).

6.2 Modelling Procedure

Indraratna *et al.* (1998) described large-scale triaxial tests on railway ballast involving applied monotonic axial loads under different confining pressures. The large-scale triaxial equipment used in their tests was shown in Figure 2.8. The size of the specimen was 300 mm diameter \times 600 mm high. Figure 6.2 shows simulated ballast particles using single spheres, eight-ball cubic clumps, ten-ball triangular clumps and ten-ball triangular clumps with eight small balls (asperities) bonded in the triaxial cell. Single-sized particles of approximately 40 mm diameter were used in order to model the particle size distribution considered by Indraratna *et al.* (1998) with $D_{50} = 38.9$ mm, $\alpha = 0.5$ (uniformity coefficient 1.6), since ballast is usually a reasonably uniformly graded material. The sizes of the balls in the clumps and the numbers of particles used in each sample are shown in Table 6.1. The total number of clumps in the triaxial test model ranges from 618 to 1006. The volume of each clump was obtained by drawing the peripheral shape of the clump in Autocad and calculating its volume. In these triaxial test models, a cylindrical vertical wall was used to simulate a flexible membrane and two horizontal walls were placed at the top and bottom of the sample, respectively. The normal and shear stiffnesses of the balls were set to be 1×10^9 N/m and the density of the balls was set to be 2,500 kg/m³. A friction coefficient of 0.5 was used for all balls. The walls were set to be frictionless with zero shear stiffness during each simulation (during both sample preparation procedure and loading). The two horizontal walls had the same normal stiffness as the particles (1×10^9 N/m); the normal stiffness of the cylindrical vertical wall (1×10^8 N/m) was set to

be one tenth of the normal stiffness of the particles in order to simulate the effect of the flexible membrane. It should be noted that when the normal stiffness of the cylindrical vertical wall is low, small spheres would penetrate through the wall as a result of the high contact forces induced between the spheres and the wall and that the effect of normal stiffness of the wall on the behaviour of the assembly is negligible. It is possible to simulate a flexible membrane using a large number of bonded balls, however, this makes the computations much too time-consuming.

	Number of clumps	Volume of clumps (mm ³)	Diameter of spheres/balls in clumps (mm)	Diameter of asperities (mm)	Porosity of the samples
Loose sample of single spheres	678	3.35×10^4	40	-	0.47
Dense sample of single spheres	742	3.35×10^4	40	-	0.41
Loose sample of eight-ball cubic clumps	840	2.57×10^4	20	-	0.48
Dense sample of eight-ball cubic clumps	1006	2.57×10^4	20	-	0.40
Loose sample of ten-ball triangular clumps	713	3.26×10^4	16.33	-	0.44
Dense sample of ten-ball triangular clumps	859	3.26×10^4	16.33	-	0.32
Sample of ten-ball triangular clumps with eight asperities	618	3.35×10^4	16.33	6	0.49

Table 6.1. Number of particles, sizes of the particles and porosity of the samples.

The assemblies were generated using the dynamic method (following McDowell *et al.*, 2006). During the generation procedure, an assembly of spheres was first generated within the cell randomly without overlapping. These spheres were

initially generated with half their final diameter. The number of spheres generated in the cell was calculated from a porosity, which is set by the user. It should be noted that the porosity set by the user may differ from the final porosity obtained in sample preparation and just before shearing shown in Table 6.1, since the final size of the triaxial cell may change slightly during sample preparation and the spheres may be replaced by other shaped particles (e.g. eight-ball cubic clumps and ten-ball triangular clumps). The spheres were then expanded to their final size and the system was cycled to equilibrium with the locations of walls remaining fixed. The system was considered to be in equilibrium when the ratio of the mean unbalanced force to the mean contact force became smaller than a set tolerance (e.g. 10^{-3}). In order to minimise the computational time during this procedure by making particle rearrangement easier, the coefficients of friction for all particles were set to zero. The spheres could then be replaced by clumps with random orientation when using non-spherical shaped particles. For the clumps, the system was cycled to equilibrium again to reduce the high contact forces produced by overlapping due to the particle replacement. In order to achieve an initial state free of internal forces, all walls were moved outwards at the same slow rate (e.g. 10^{-4} m/s). The system was cycled to equilibrium (with no wall movement) after every 50 cycles (of wall movement) until internal forces were completely released and the system was in equilibrium. It is important to note that for all the simulations, the final dimensions of the cell were approximately equal to 300 mm \times 600 mm. This was achieved by trial and error using different initial sizes for the cell.

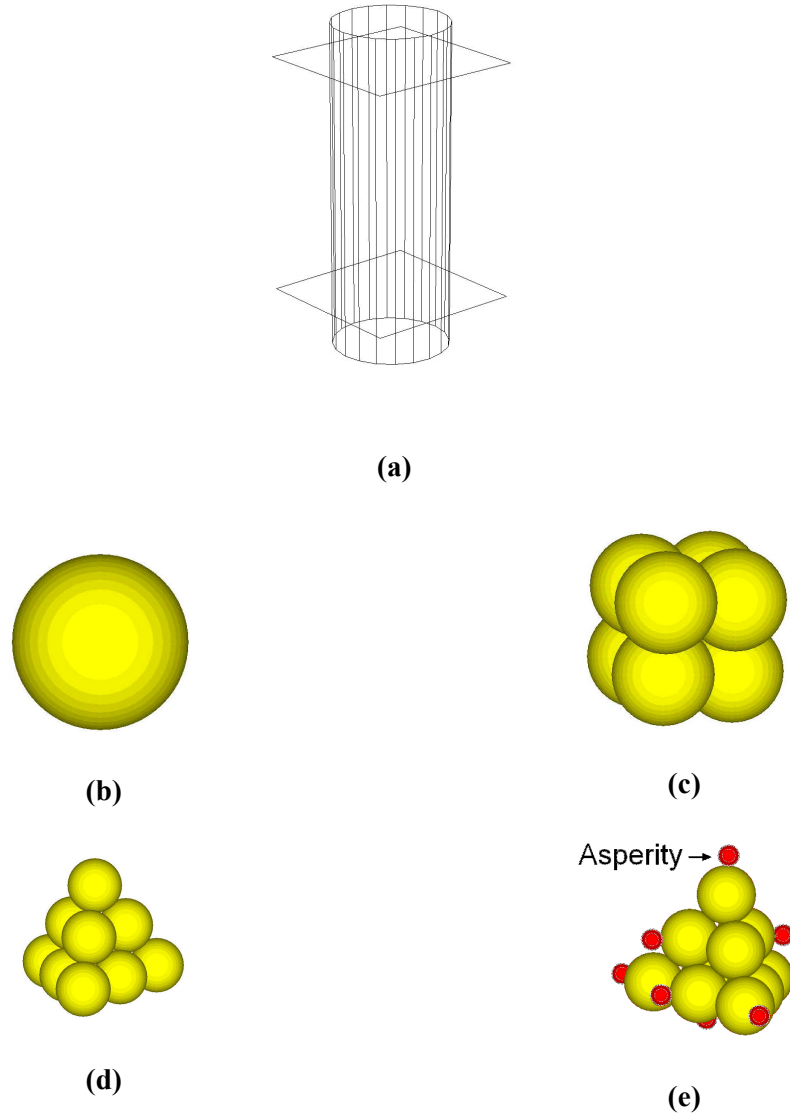


Figure 6.2. PFC^{3D} model (a) triaxial cell; (b) single sphere as a ballast particle; (c) eight-ball cubic clump as a ballast particle; (d) ten-ball triangular clump as a ballast particle and (e) ten-ball triangular clump with eight small balls (asperities) bonded as a ballast particle.

After the procedure of assembly generation was completed, isotropic compression was applied to achieve the required stress state. The servo-control mechanism was applied to all walls, so that the required confining pressures were obtained. The normal stress on each wall was calculated by the summation of the normal contact

forces on the wall divided by the area of the wall. Different porosities were prepared using single spheres, eight-ball cubic clumps and ten-ball triangular clumps, respectively. Friction coefficients from 0.0 to 1.0 were used to control the porosities of assemblies during isotropic compaction; after compaction the friction coefficient was changed back to 0.5 for the shearing stage of the simulation. Once the required stress state was achieved, monotonic loading was applied to both the top and bottom walls with a constant speed of 0.02 m/s, so that the rate of loading was slow enough for the samples to remain under static loading conditions, but the fastest rate which could be used without affecting the results.

6.3 Selecting Particle Shape

Particle shape plays a key role in the behaviour of railway ballast. Using complex irregular shaped clumps to represent each ballast particle in the large-scale triaxial test simulation is not practical due to the calculations being too time-consuming. In this section, three different simple shapes were used to represent each ballast particle in the triaxial test simulations to obtain an acceptable shape for modelling railway ballast.

Table 6.1 lists the porosity of the samples produced by using different friction coefficients (e.g. $\mu = 0.0$ for dense samples and $\mu = 1.0$ for loose samples) for each particle shape model under 120 kPa isotropic compaction. It should be noted that the internal voids of clump were not included in the calculation of porosity, as the volume of clump was calculated by Autocad (as mentioned in section 6.2). Monotonic loading was applied to each sample under a confining pressure of 120

kPa. The stress-strain behaviour and the volume change during the shearing of these samples are plotted in Figure 6.3.

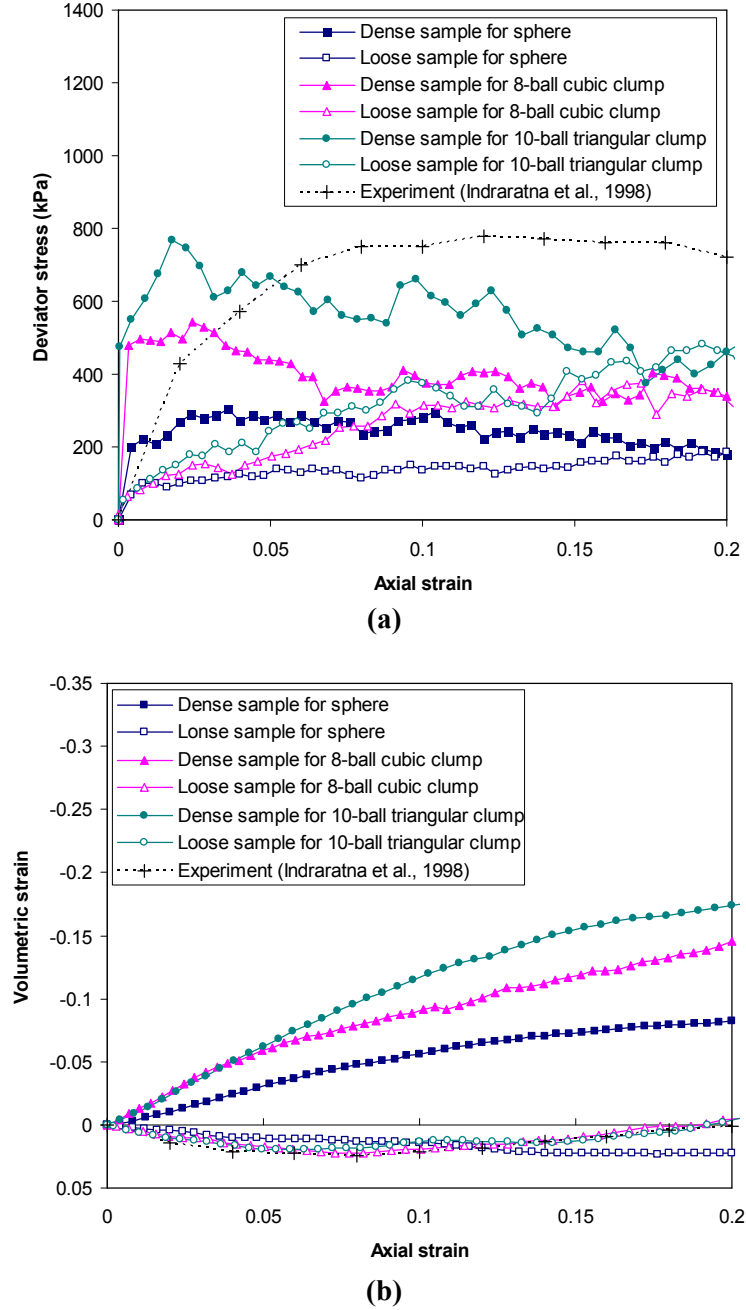


Figure 6.3. Results of triaxial simulations on both loose and dense samples for spheres, eight-ball cubic clumps and ten-ball triangular clumps under a confining pressure of 120 kPa.

As can be seen from Figure 6.3, both peak strength and ultimate strength increase with increasing particle angularity, and increasing particle angularity gives a higher initial stiffness. This is in agreement with the experimental findings of many researchers cited by Selig and Waters (1994) and Lekarp *et al.* (2000a). The ultimate strengths of loose and dense samples agree, which means that all these samples reached a critical state. The loose samples have approximately the correct porosity, comparing with the experimental data, and the correct volumetric response, but the shearing resistances are too low, so further modifications were made to try to correct this. The ten-ball triangular clumps were used in the following simulations, as they provided a higher shear strength compared to the two other shaped particle models.

It is noted that the stress-strain response of an assembly not only depends on the particle shape but also on interparticle friction. A series of simulations was carried out to investigate the effect of friction coefficient. Both loose and dense samples for the ten-ball triangular clump were used in these simulations, and different friction coefficients (varying from 0.3 to 1.0) were applied. The effect of friction coefficient on the shear strength and volumetric strain is shown in Figure 6.4 for the dense samples and in Figure 6.5 for the loose samples. It can be seen in Figures 6.4 and 6.5 that the friction coefficient has a large effect on shear strength when the friction coefficient is lower than 0.8. However, it makes little difference to the shear strength when the friction coefficient is increased from 0.8 to 1.0. Therefore, the shear strength of assembly cannot keep increasing by increasing interparticle friction. Similar findings for simple particle shapes were reported by

Ni (2003) and Suiker and Fleck (2004), as shown in Figure 3.13. As for the volumetric behaviour, increasing the friction coefficient causes the assembly to be more dilative. This is also in agreement with the findings from Ni (2003) and Suiker and Fleck (2004).

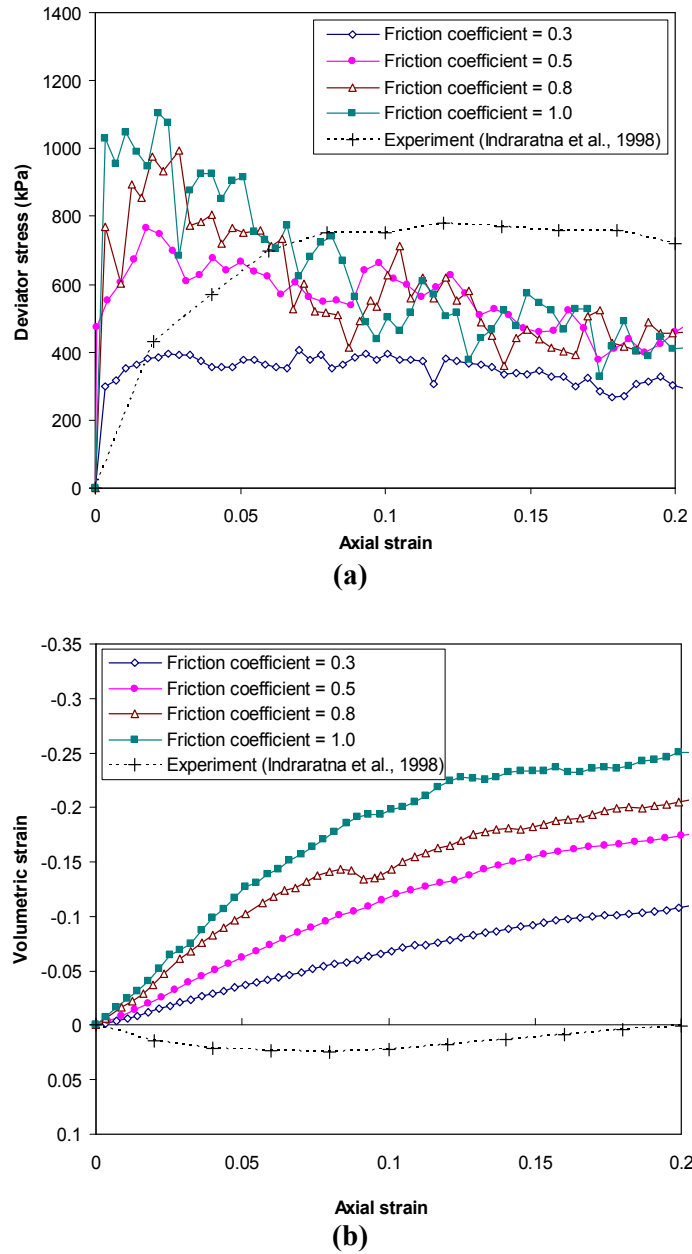
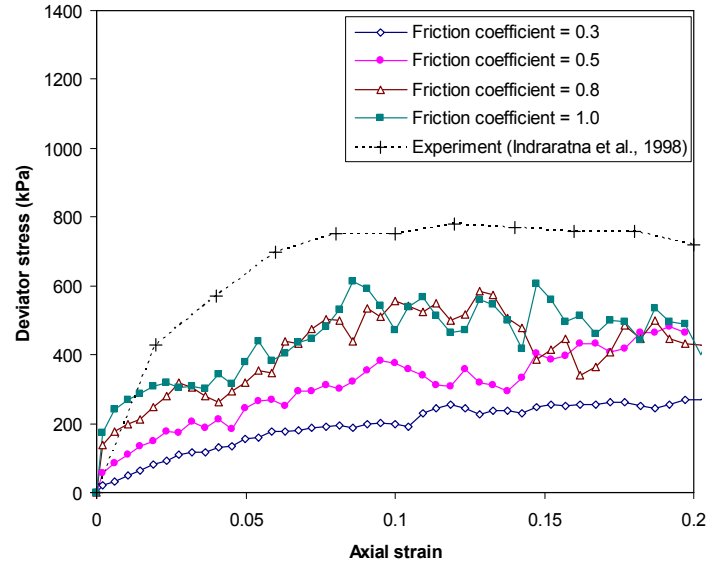
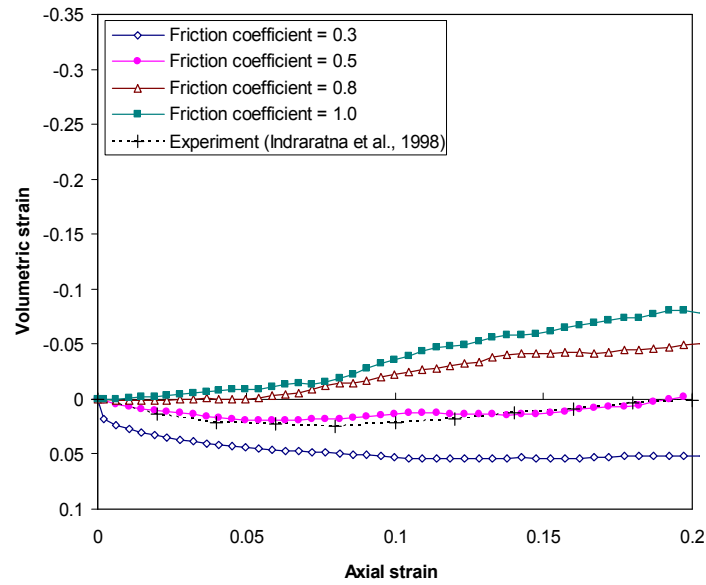


Figure 6.4. Effect of friction coefficient on (a) shear strength and (b) volumetric strain (contraction positive) for dense sample of ten-ball triangular clumps.



(a)



(b)

Figure 6.5. Effect of friction coefficient on (a) shear strength and (b) volumetric strain (contraction positive) for loose sample of ten-ball triangular clumps.

Comparing with experimental data (as shown in Figures 6.4 and 6.5), the ultimate strengths of the assemblies in the simulations are still far lower than that of the real ballast, even when a high friction coefficient is used. For the loose sample, when the friction coefficient is higher than 0.5, the assembly is more dilative than the

real ballast. Thus, the correct ultimate shear strength cannot be modelled by purely increasing the friction coefficient.

6.4 Modelling Particle Abrasion

6.4.1 Parallel bond contact law between clumps

A real ballast particle is typically angular with a rough surface texture and particle interlocking plays an important role in the shear behaviour of a ballast assembly. Selig and Waters (1994) reviewed experimental data for granular materials and pointed out that increasing both angularity and particle surface roughness increases the shear strength of the assembly. Particle interaction (e.g. sliding and rolling of individual particles) is very complex. Interlocking at a contact between two ballast particles resulting from the rough surface texture or asperities provides extra shearing resistance. The effect of rough surface texture is hard to model by using very small balls to form the real ballast particle surface, and modelling fine particle shape requires a large number of balls, which would lead to unrealistic computational time. Because of the idealised smooth surface of balls in the numerical model, shearing resistance provided by friction (via the sliding model) is insufficient in modelling railway ballast. In order to increase the shear strength of an assembly to that of real ballast measured in the laboratory tests, a parallel bond contact law provided by PFC^{3D} (Itasca, 1999) was introduced at each contact between clumps to model the interlocking of ballast particles resulting from very small asperities (i.e. the rough surface texture) without cementation. The parallel bond breaks when the stress in any part of the bond exceeds the specified (weak)

parallel bond strength. Compared to the shear strength of a parallel bond, a very low normal strength of parallel bond was used, so that the tensile force sustainable between clumps is so small that it can be ignored. The parallel-bond model is active in conjunction with the slip model at each contact between two clumps and shearing resistance at the contact is provided by both friction and the parallel bond. The purpose of using the parallel bond between clumps in modelling railway ballast is simply to simulate the shear and rotational resistance provide by interlocking small asperities. Parallel bonds were created at each particle contact between two clumps before isotropic compaction was applied to the samples. During isotropic compaction and shearing, a new parallel bond was created immediately when a new contact between two clumps was formed.

The loose sample for ten-ball triangular clumps (used in section 6.3 and Figure 6.5) was used in the following simulations. The initial porosity of this sample is 0.44; the friction coefficient is 0.5. A series of four simulations with constant ratio of shear to normal parallel bond strength between clumps (i.e. ratio of 50) was performed to investigate the effect of bond strength. In order to prevent large relative displacement of two contacted clumps (i.e. the displacement of parallel bond) occurring, the stiffnesses of parallel bonds have constant ratio with the parallel bond strengths (i.e. parallel bonds break at the same bond strain). The parameters for the parallel bonds between clumps used in these simulations are listed in Table 6.2.

	Normal bond strength (kPa)	Shear bond strength (kPa)	Normal bond stiffness (MPa/m)	Shear bond stiffness (MPa/m)
Simulation 6.1	10	5×10^2	10	10^2
Simulation 6.2	10^2	5×10^3	10^2	10^3
Simulation 6.3	10^3	5×10^4	10^3	10^4
Simulation 6.4	5×10^3	2.5×10^5	5×10^3	5×10^4

Table 6.2. Parameters of parallel bonds between clumps used in the series of simulations to investigate the effect of increasing bond strengths and stiffnesses for parallel bonds between clumps.

The results of these simulations are shown in Figure 6.6. The experimental result under a confining pressure of 120 kPa is shown on the same figure for comparison. Comparing with the experimental result, the shear strength of the assembly in Simulation 6.2 matches the experimental result under a confining pressure of 120 kPa, though there is too much dilation compared to the experiment data. It can be seen from Figure 6.6(a) that the shear strength, particularly peak strength, increases with increasing bond strength between clumps. More dilation is observed (as shown in Figure 6.6(b)) when the parallel bond strength increases. Although increasing the bond strength between clumps increases the peak strength of the assembly, the behaviour becomes more brittle.

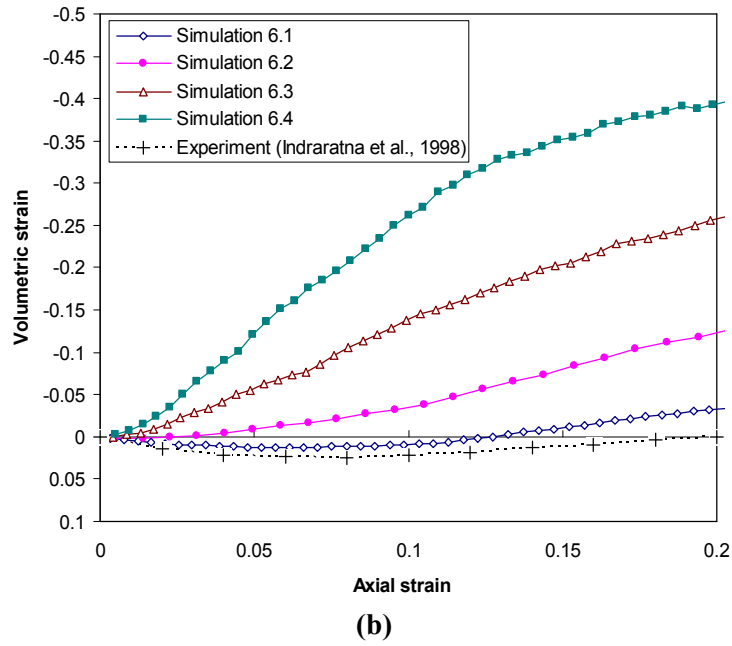
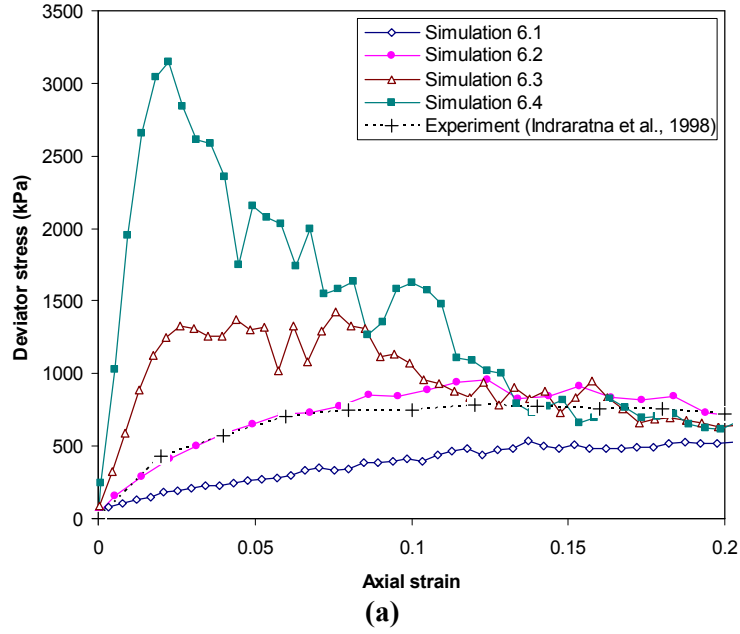


Figure 6.6. Effect of increasing parallel bond strength and stiffness between clumps on (a) shear strength and (b) volumetric strain (contraction positive).

Figure 6.7 shows the average coordination number of clumps with different parallel bond strengths during loading. It can be seen from Figure 6.7 that the assembly with higher bond strength has lower mean coordination number and the

mean coordination number decreases when the assembly dilates. This indicates that higher bond strengths lead to more particle rolling instead of sliding, more dilation of the assembly and lower coordination number.

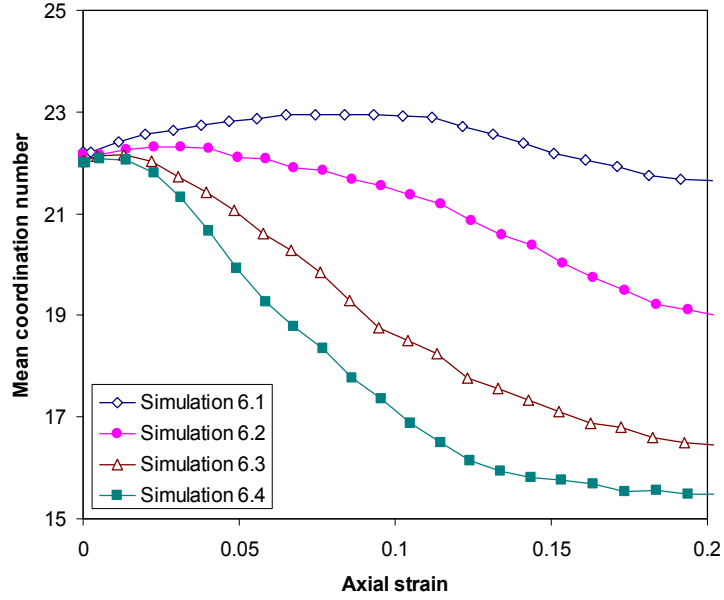


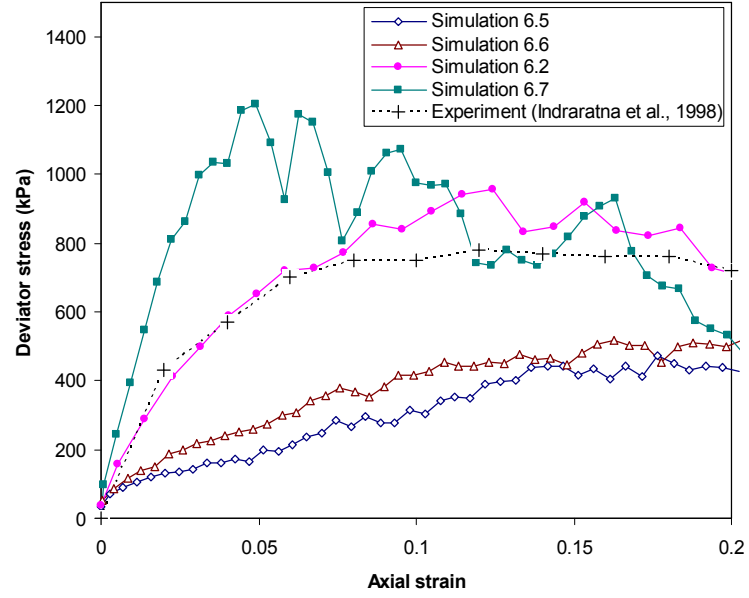
Figure 6.7. Effect of increasing parallel bond strength and stiffness between clumps on average coordination number of clumps.

A series of tests (Simulations 6.5-6.7) with constant normal bond strength (10^2 kPa) and normal stiffness (10^2 MPa) was performed to study the effect of the ratio of shear to normal strength. The parameters for the parallel bonds between clumps used in these simulations are listed in Table 6.3. Shear bond strengths and stiffnesses within the range of 0.01 to 5 times the values used in Simulation 6.2 were applied and the normal bond strength and stiffness used in this series of tests were the same as those in Simulation 6.2.

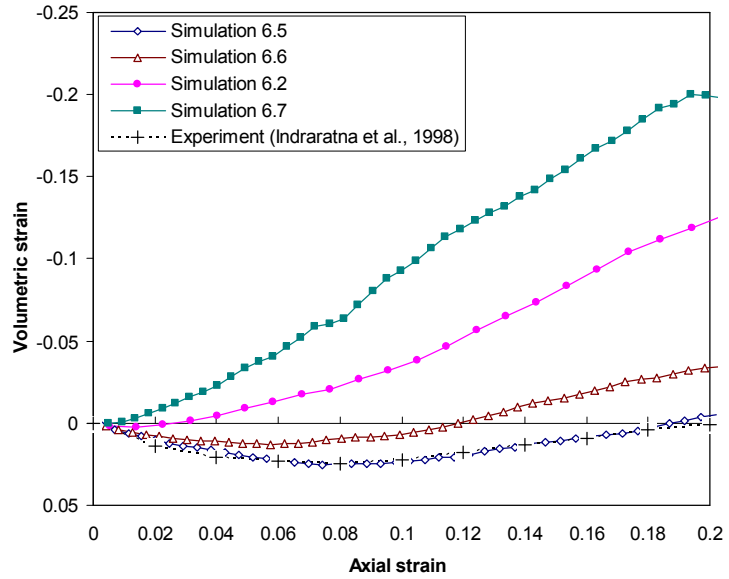
	Normal bond strength (kPa)	Shear bond strength (kPa)	Normal bond stiffness (MPa)	Shear bond stiffness (MPa)
Simulation 6.5	10^2	50	10^2	10
Simulation 6.6	10^2	5×10^2	10^2	10^2
Simulation 6.2	10^2	5×10^3	10^2	10^3
Simulation 6.7	10^2	2.5×10^4	10^2	5×10^3

Table 6.3. Parameters of parallel bonds between clumps used in the series of simulations to investigate the effect of increasing ratio of shear to normal bond strength and stiffness for parallel bonds between clumps.

Figure 6.8 shows the shear stress-strain relationship and volumetric strain behaviour for this series of tests. It can be seen from this figure that the shear strength of the assembly, in particularly peak strength, increases with increasing ratio of shear to normal bond strength and stiffness. Well-defined post-peak softening occurs when the shear parallel bond strength is high. It should be noted that if the shear bond strength is set too high, the parallel bond would break due to the normal stress exceeding the normal strength rather than the shear stress exceeding the shear strength. Figure 6.9 shows the average coordination number of clumps with different parallel bond strengths during loading. It can be seen from this figure that the average coordination number of clumps decreases with increasing shear bond strength. These results are similar to the results shown in Figures 6.6 and 6.7.



(a)



(b)

Figure 6.8. Effect of increasing the ratio of shear parallel bond strength and stiffness to normal parallel bond strength and stiffness between clumps on (a) shear strength and (b) volumetric strain (contraction positive).

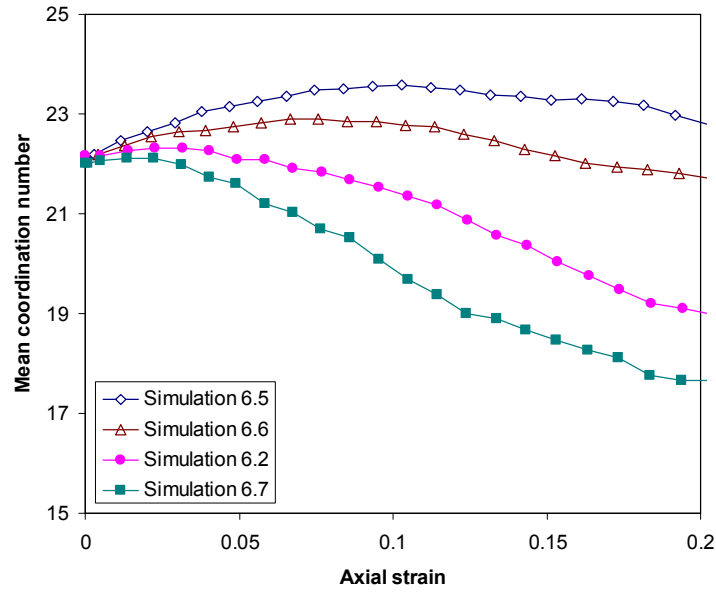


Figure 6.9. Effect of increasing the ratio of shear parallel bond strength and stiffness to normal parallel bond strength and stiffness between clumps on average coordination number of clumps.

6.4.2 Using asperities

In the previous subsection, although the shear strength and stiffness of the ballast assembly could be modelled by adding weak parallel bonds between clumps to model small-scale asperities interlocking, dilation rather than contraction was observed during loading with 120 kPa confining pressure. Particle breakage was observed in the laboratory experimental work (Indraratna *et al.*, 1998). McDowell *et al.* (2006) therefore suggested that particle breakage should be considered in DEM simulations on ballast. Although, bulk fracture may occur under high stress levels, laboratory tests (Indraratna *et al.*, 2005 and Aursudkij, 2007) have been shown that most ballast degradation is attributed to corner breakage and that bulk fracture is not significant. Therefore, the effect of bulk fracture is not considered

here. Chapter 5 has shown that modelling abrasion is necessary to give the correct response in terms of settlement as a function of number of loading cycles for ballast subjected to cyclic loading in the box test simulations. Therefore, here only abrasion is considered.

In order to model the correct response of volume change during compaction, eight small balls were bonded to each ten-ball triangular clump at the corners and edges using contact bonds and parallel bonds to model small asperities, as shown in Figure 6.2(e). The diameter of these small balls is 6 mm. A sample with a porosity of 0.49 was made. A series of simulations was carried out to study the influence of the asperity breakage – i.e. particle abrasion. The parameters of the contact and parallel bonds used in these simulations for bonding the small balls are listed in Table 6.4 and the parameters of the weak parallel bonds between clumps, used to model the particles interlocking at very small asperity contacts, were set to be the same as those in Simulation 6.2 (listed in Table 6.2): i.e. much weaker than the asperity bond strengths.

Figure 6.10 shows the results in terms of deviator stress and volumetric strain against axial strain. It can be seen in Figure 6.10 that with decreasing asperity bond strength, shear strength of the assembly decreases and the assembly becomes more contractive. Figure 6.11 shows the number of asperities broken off during the monotonic loading. As expected, the number of asperities broken off increases with a decrease in the bond strength of asperities. Hence, it can be seen that the number of broken asperities during shearing affects both the shear strength and the volumetric response of the assembly. The higher the number of broken asperities

during shearing, the lower the shear strength and the less dilative the assembly. Particle abrasion therefore plays an important role in the shear stress-strain relationship and volumetric behaviour. In order to achieve both an acceptable shear stress-strain response and an acceptable volumetric strain response, Simulation 6.11 seems to offer the best compromise. Figure 6.12 shows the locations of broken asperities during monotonic loading in Simulation 6.11. As can be seen from the figure, no particular zone where asperities break a lot is observed. In other words, as asperities break and particle columns buckle, the applied boundary stresses cause a redistribution of contacts and new asperities break.

	Normal parallel bond strength (MPa)	Shear parallel bond strength (MPa)	Normal parallel bond stiffness (GPa/m)	Shear parallel bond stiffness (GPa/m)	Normal contact bond strength (kN)	Shear contact bond strength (kN)	Normal contact bond stiffness (GN/m)	Shear contact bond stiffness (GN/m)
Simulation 6.8	6×10^2	6×10^2	1.768×10^3	1.768×10^3	1.7×10^2	1.7×10^2	1	1
Simulation 6.9	1.2×10^3	1.2×10^3	3.536×10^3	3.536×10^3	1.7×10^2	1.7×10^2	1	1
Simulation 6.10	3×10^3	3×10^3	8.840×10^3	8.840×10^3	1.7×10^2	1.7×10^2	1	1
Simulation 6.11	6×10^3	6×10^3	1.768×10^4	1.768×10^4	1.7×10^2	1.7×10^2	1	1
Simulation 6.12	6×10^4	6×10^4	1.768×10^5	1.768×10^5	1.7×10^2	1.7×10^2	1	1

Table 6.4. Parameters for parallel bonds and contact bonds used to bond asperities with clumps used in the series of simulations to investigate the effect particle abrasion.

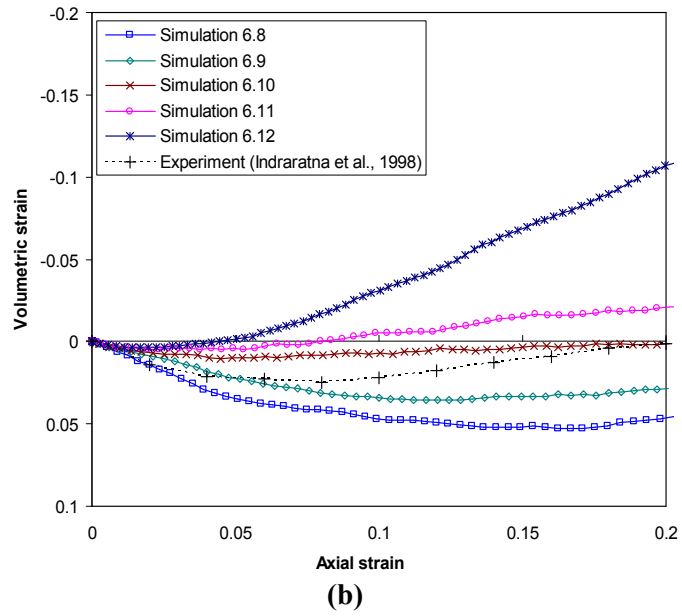
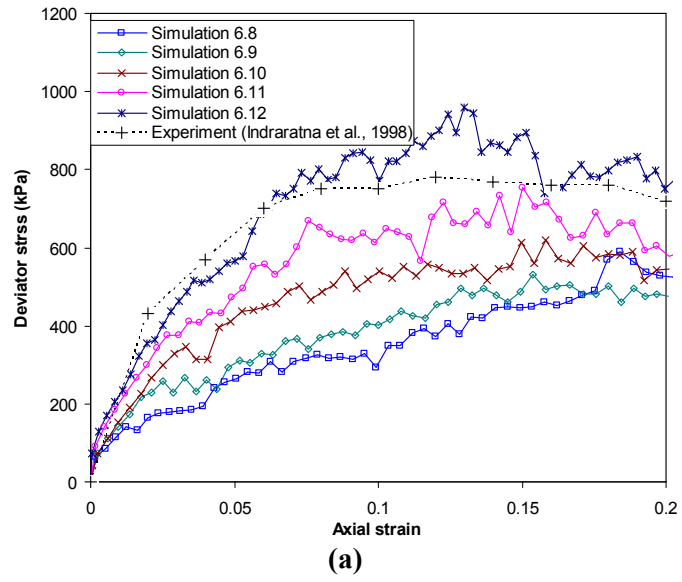


Figure 6.10. Effect of increasing bond strength and stiffness between clump and asperity on (a) shear strength and (b) volumetric strain (contraction positive).

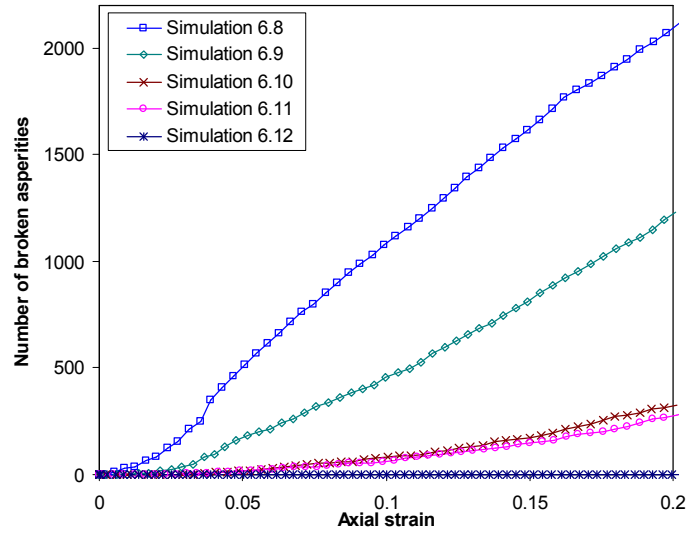


Figure 6.11. Number of asperities broken off during monotonic loading.

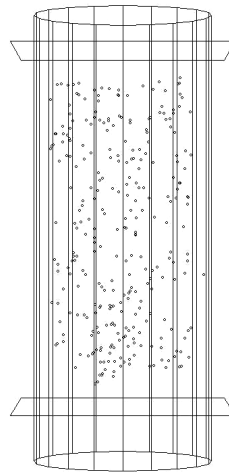


Figure 6.12. Locations of broken bonds between clumps and asperities during monotonic loading in Simulation 6.11.

6.5 Modelling Railway Ballast Behaviour under a Large Range of Confining Pressures

Triaxial test simulations using ten-ball triangular clumps bonded with eight small balls were carried out under a range of confining pressures (from 15 kPa to 240

kPa) used by Indraratna *et al.* (1998). The parameters of the weak parallel bonds used between clumps were those in Simulation 6.2 (the same as those in Simulation 6.11) and the contact and parallel bonds used to bond asperities with clumps were those in Simulation 6.11 as the shear strength and volumetric behaviour were deemed to be acceptably close to the experimental result. A series of simulations using unbreakable ten-ball triangular clumps with eight small balls (i.e. asperities which cannot break off and are treated as part of the clump) were also carried out under a range of confining pressures (from 15 kPa to 240 kPa) for comparison. For the unbreakable assembly, the parameters of the weak parallel bonds used between clumps were also those in Simulation 6.2.

6.5.1 Axial and volumetric strain

Figure 6.13 shows the simulation and experimental results, in terms of deviator stress against axial strain; Figure 6.14 shows the simulation and experimental results, in terms of volumetric strain against axial strain. Figures 6.15(a) and (b) show the numbers of asperities broken off under different confining pressures against axial strain and volumetric strain, respectively. As can be seen from Figures 6.13, 6.14 and 6.15, particle abrasion plays an important role in correctly modelling both shear strength and volumetric change of the assembly of ballast.

Comparing the experimental results with the simulation results which incorporated abrasion, the stress-strain relationship is well simulated at low stress levels (15 kPa – 120 kPa), however, for the simulation under a confining pressure of 240 kPa, the shear strength of the assembly simulated is a little lower than the experimental one.

Comparing the shear strengths of the breakable assembly to those of the unbreakable assembly (as shown in Figures 6.13(a) and (b)), the shear strength has decreased to some degree as a result of particle breakage (as shown in Figure 6.15).

As for the volumetric behaviour, more dilation is observed in the simulations for both breakable assembly and unbreakable assembly at the low stress levels. High dilation is still pronounced at high confining pressures, when the particle breakage is not considered, as shown in Figure 6.14(b). However, it can be seen in Figure 6.14(a) that for the sample with simulated abrasion, dilation has reduced much more with increasing confining stress as more asperities break. Volumetric strain agrees reasonably with the experimental results under a high confining pressure (240 kPa) where asperity breakage is pronounced. This is probably due to the arbitrary number of asperities bonded on each clump and the asperity size. Smaller balls may break at lower stress levels, giving more asperity breakage and less dilation. Using more and smaller balls bonded to the clumps as asperities may give more realistic volumetric strains at lower confining pressures. Therefore, further investigation of the effect of number and size of asperities is needed; this is suggested for further research.

It can be seen from Figure 6.15 that particle abrasion occurs at both low and high stress levels. With increasing confining pressure, more asperities are broken off. This finding agrees with Indraratna *et al.* (1998).

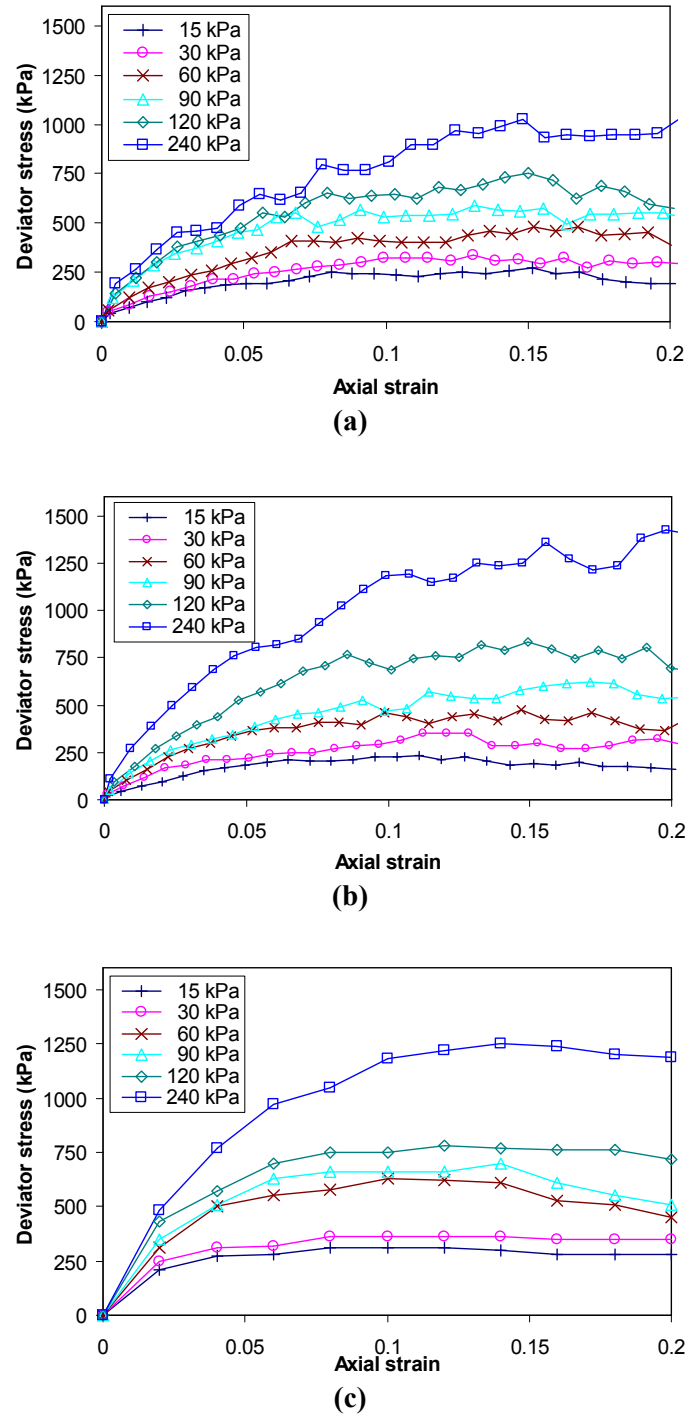
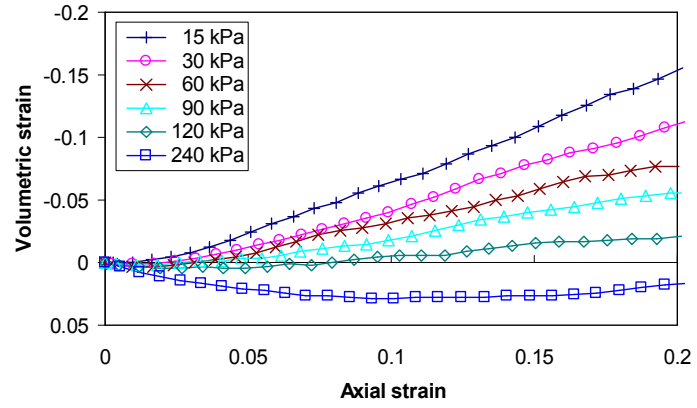
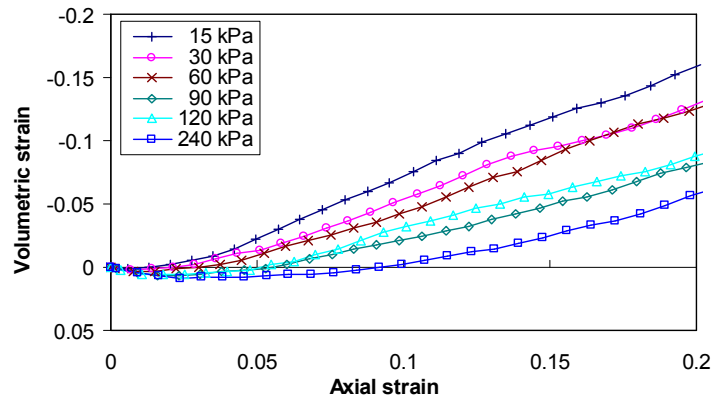


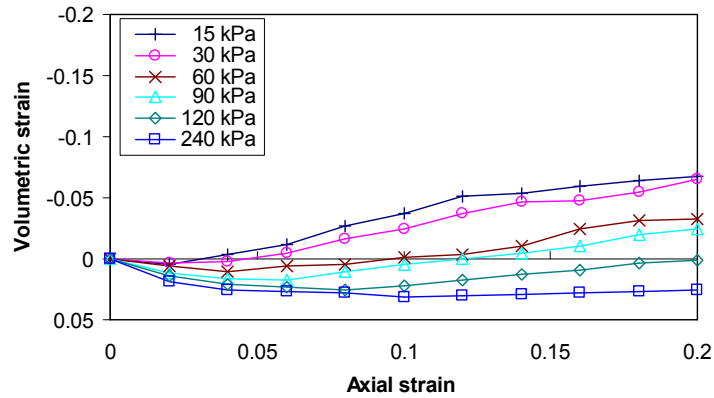
Figure 6.13. Results of deviator stress against axial strain under a range of confining pressures (a) using ten-ball triangular clumps bonded with eight small balls as asperities; (b) using ten-ball triangular clumps with eight small balls (unbreakable asperities) and (c) experimental results (Indraratna *et al.*, 1998).



(a)



(b)



(c)

Figure 6.14. Results of volumetric strain against axial strain under a range of confining pressures (a) using ten-ball triangular clumps bonded with eight small balls as asperities; (b) using ten-ball triangular clumps with eight small balls (unbreakable asperities) and (c) experimental results (Indraratna *et al.*, 1998).

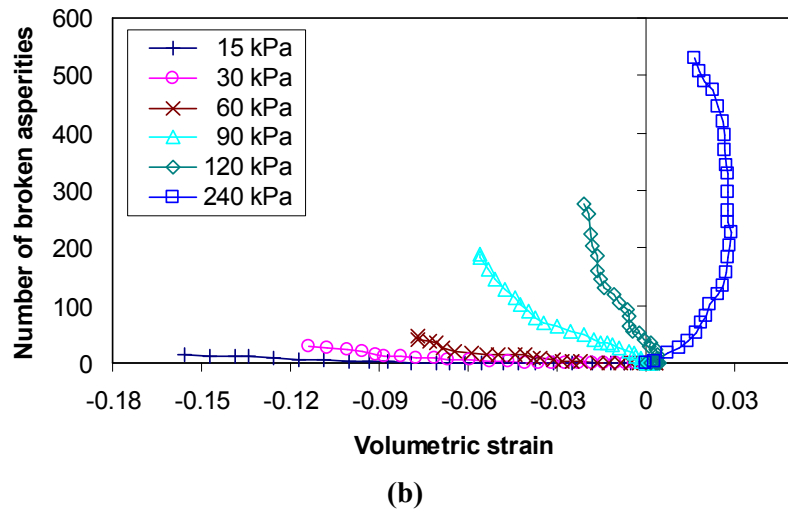
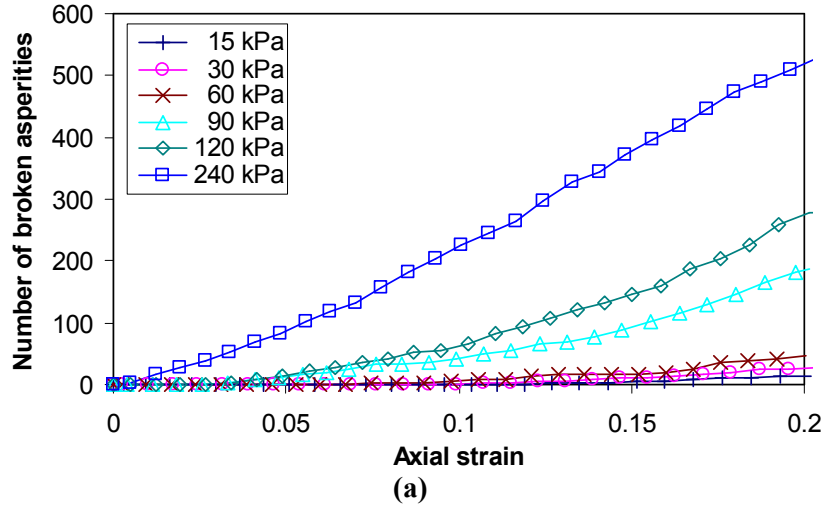


Figure 6.15. Number of asperities broken off during monotonic loading under a range of confining pressures against (a) axial strain and (b) volumetric strain.

6.5.2 Number of contacts

Figure 6.16 shows a plot of the number of contacts prior to shearing and after shearing (i.e. axial strain = 0.2) for the breakable and unbreakable assemblies against confining pressure. As can be seen from the figure, the assemblies under different isotropic compaction pressures (prior to shearing) have similar numbers

of contacts (approximately 7000); after shearing to 0.2 axial strain, the number of contacts for both the breakable and unbreakable assemblies increases with increasing confining pressure. For the unbreakable assembly after shearing, the number of contacts under different confining pressures is always lower than the initial number of contacts as the sample dilates; however, for the breakable assembly after shearing, the number of contacts is lower than the initial number of contacts under lower confining pressures (15 kPa – 60 kPa) as the sample dilates and higher than the initial numbers of contacts under higher confining pressures (90 kPa – 240 kPa), as the sample contracts.

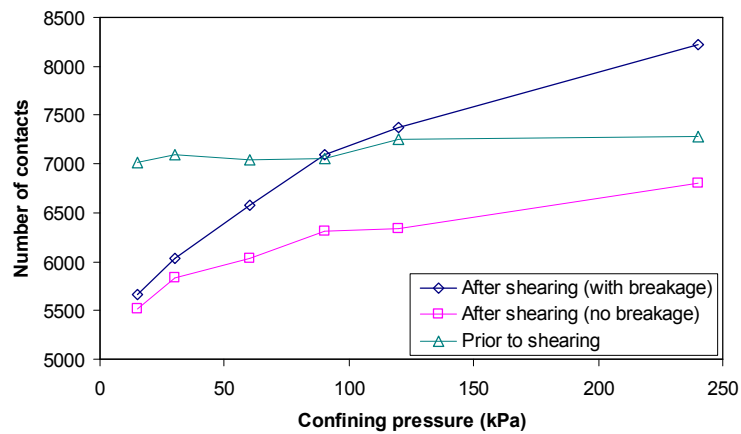


Figure 6.16. Number of contacts prior to shearing and after shearing for the breakable and unbreakable assemblies.

The important finding here is that without particle abrasion, discrete element modelling shows that increasing the confining pressure does not sufficiently suppress the dilatancy under monotonic shear loading. However, when asperity abrasion is included, the volumetric response under increasing confining stress is much more promising. Comparing with the unbreakable assembly, asperity

abrasion leads to a higher number of contacts, and particle rotations and dilatancy are more suppressed. Therefore, abrasion provides a key micro mechanical explanation for the elimination of dilatancy with increasing confining pressure under monotonic loading.

6.6 Conclusions

The stress-strain behaviour of railway ballast under monotonic loading has been modelled using the discrete element method. The results have shown that particle shape, interparticle friction, interlocking and asperity fracture all play an important role in determining the mechanical behaviour of railway ballast. The shear strength of an assembly of spheres is very low compared to that of real ballast. Even using more angular particles with an increased coefficient of friction is not enough to increase the shear strength of the assembly to be as high as that of real ballast. By adding weak parallel bonds between clumps to simulate surface texture and enhance the shear resistance of each particle contact, the correct shear strength of railway ballast can be simulated. However, introducing particle shape, increasing the coefficient of friction and introducing parallel bonds between clumps each produce more dilation, so that too much dilation is observed. Realistic volumetric change behaviour can be obtained if particle abrasion is modelled. It has been shown that by introducing parallel bond contact law between clumps and bonded asperities, approximately the correct response in terms of shear stress and volumetric strain can be observed for a range of confining pressures.

CHAPTER 7

CYCLIC TRIAXIAL TEST SIMULATIONS

7.1 Introduction

Since the mechanical behaviour of railway ballast under cyclic loading differs from that under monotonic loading, large-scale cyclic triaxial test equipment has been used by various researchers (e.g. Indraratna *et al.*, 2005; Suiker *et al.*, 2005; Lackenby *et al.*, 2007) to investigate the permanent strain and particle degradation of ballast under a variety of repeated loading conditions. Chapter 6 examined the modelling of the mechanical behaviour, including particle breakage, in the monotonic triaxial test simulations under a range of confining pressures. The simulation and experimental results were in broad agreement. In this chapter, the ten-ball triangular clumps bonded with eight small balls described in Chapter 6 are used. A series of simulations using both a breakable assembly and an unbreakable assembly under a confining pressure of 120 kPa are carried out to study the effect of particle abrasion under different cyclic loads. A series of simulations using breakable assemblies were then conducted to investigate the effect of confining pressure, cyclic deviator stress magnitude and the number of cycles on the permanent strain and breakage of ballast. The results are compared with the

experimental data (Lackenby *et al.*, 2007). Simulation results under cyclic loading are also compared with those under monotonic loading conditions obtained in Chapter 6. In addition, the effect of parallel bonds between clumps (used to simulate interlocking of very small asperities) is studied by using different bond strengths.

7.2 Modelling Procedure

The particle model used in this chapter is the ten-ball triangular clump with eight asperities described in Chapter 6, as shown in Figure 6.2(e). The geometry and construction of the simulated triaxial cell is also the same. The samples had dimensions of approximately 300 mm diameter \times 600 mm high, with each sample having 618 particles (a particle being a ten-ball triangular clump with eight asperities). Figure 7.1 shows a sample with 618 particles of ten-ball triangular clumps under 120 kPa confining pressure prior to loading. The initial porosity of this sample was 0.44. The properties of the particles were the same as those of the ten-ball triangular clump with eight asperities in section 6.5. The normal and shear stiffnesses of the balls were both 1×10^9 N/m and the density of the particles was $2,500 \text{ kg/m}^3$. The coefficient of friction for the balls was set to 0.5. The walls were set to be frictionless with zero shear stiffness during each simulation. The two horizontal walls had the same normal stiffness as the particles (1×10^9 N/m); the normal stiffness of the cylindrical vertical wall (1×10^8 N/m) was set to be one tenth of the normal stiffness of the particles. The parameters of the contact and parallel bonds for bonding the small balls (asperities) are listed in Table 7.1 and

the parameters of the weak parallel bonds between clumps (used to model the interlocking at very small asperity contacts) are listed in Table 7.2.

Simulation number	Normal parallel bond strength (MPa)	Shear parallel bond strength (MPa)	Normal parallel bond stiffness (GPa/m)	Shear parallel bond stiffness (GPa/m)	Normal contact bond strength (kN)	Shear contact bond strength (kN)	Normal contact bond stiffness (GN/m)	Shear contact bond stiffness (GN/m)
Simulation 7.4-7.19	6×10^3	6×10^3	1.768×10^4	1.768×10^4	1.7×10^2	1.7×10^2	1	1

Table 7.1. Parameters for parallel bonds and contact bonds used to bond asperities with clumps used in the simulations.

Simulation number	Normal parallel bond strength (kPa)	Shear parallel bond strength (kPa)	Normal parallel bond stiffness (MPa/m)	Shear parallel bond stiffness (MPa/m)
Simulation 7.1-7.17	100	5,000	100	1,000

Table 7.2. Parameters for parallel bonds between clumps used in the simulations.

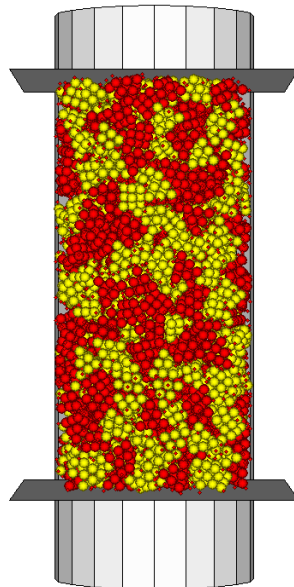


Figure 7.1. Assembly of ten-ball triangular clumps with eight small balls (asperities) bonded in the triaxial cell.

The normal stress on each wall was calculated by the summation of the normal contact forces on the wall divided by the area of the sample where the wall was located. The servo-control mechanism was applied to all walls to maintain the required confining pressures and cyclic loading. Following Lackenby *et al.* (2007), samples under confining pressures ranging from 10 kPa to 240 kPa were simulated and sinusoidal load pulses were applied to the samples with a minimum load of 45 kPa being set for each test. Three different magnitudes of maximum load were used: 230 kPa, 500 kPa and 750 kPa. The frequency of the cyclic load was 4 Hz. Limitations in computing time make it unrealistic to perform simulations with as many cycles as in the experimental tests, so one hundred loading cycles were applied in each simulation. The axial strain and the overall volumetric strain of the sample were monitored, and the location of asperity breakage was recorded. Following Lackenby *et al.* (2007), failure of ballast specimens under repeated loading is defined by an arbitrary level of strain accumulation (e.g. axial strain is higher than 0.25).

The cyclic triaxial test simulations were divided into three test series. Series 7.1 was to study the effect of particle abrasion (asperity breakage) with a confining pressure of 120 kPa being used with both the breakable and unbreakable assemblies prepared in the monotonic triaxial test simulations in section 6.5. The simulations in Series 7.1 are summarised in Table 7.3.

The simulations in Series 7.2 used the crushable assembly and were carried out under different loading conditions, as listed in Table 7.4. The results were compared with experimental data (Lackenby *et al.*, 2007). The aim of these

simulations was to study the effect of confining pressure and cyclic deviator stress magnitude on the micro mechanical behaviour of railway ballast, including degradation. The breakable assemblies prepared in the monotonic triaxial test simulations in section 6.5 under a range of confining pressures (from 30 kPa to 240 kPa) were used here. A breakable assembly with a confining pressure of 10 kPa was also prepared using the same procedure as described in section 6.2. The parameters of the weak parallel bonds between clumps and the contact and parallel bonds used to bond asperities with clumps were the same as those used in section 6.5 (as listed in Table 7.1 and 7.2).

Simulation number	Confining pressure (kPa)	Maximum deviator stress (kPa)	Asperities
Simulation 7.1	120	230	unbreakable
Simulation 7.2	120	500	unbreakable
Simulation 7.3	120	750	unbreakable
Simulation 7.4	120	230	breakable
Simulation 7.5	120	500	breakable
Simulation 7.6	120	750	breakable

Table 7.3. List of cyclic triaxial test simulations in Series 7.1.

Different parallel bond strengths between clumps were used in Series 7.3 to investigate the effect of parallel bonds between clumps (used to simulate small-scale asperity interlocking) on the behaviour of the assembly. The parallel bond strengths between clumps are listed in Table 7.5. A confining pressure of 30 kPa and a maximum deviator stress of 750 kPa were used in this series.

Simulation number	Confining pressure (kPa)	Maximum deviator stress (kPa)	Asperities
Simulation 7.7	10	230	breakable
Simulation 7.8	10	500	breakable
Simulation 7.9	30	230	breakable
Simulation 7.10	30	500	breakable
Simulation 7.11	30	750	breakable
Simulation 7.12	60	230	breakable
Simulation 7.13	60	500	breakable
Simulation 7.14	60	750	breakable
Simulation 7.4	120	230	breakable
Simulation 7.5	120	500	breakable
Simulation 7.6	120	750	breakable
Simulation 7.15	240	230	breakable
Simulation 7.16	240	500	breakable
Simulation 7.17	240	750	breakable

Table 7.4. List of cyclic triaxial test simulations in Series 7.2.

Simulation number	Normal parallel bond strength (kPa)	Shear parallel bond strength (kPa)	Normal parallel bond stiffness (MPa/m)	Shear parallel bond stiffness (MPa/m)
Simulation 7.18	50	2,500	50	500
Simulation 7.11	100	5,000	100	1,000
Simulation 7.19	300	15,000	300	3,000

Table 7.5. Parameters for parallel bonds between clumps used in the simulations in Series 7.3.

7.3 Effect of Particle Abrasion under Cyclic Loading

A series of simulations (Series 7.1) using the breakable and unbreakable assemblies under a confining pressure of 120 kPa were carried out, with maximum deviator stresses of 230 kPa, 500 kPa and 750 kPa being applied.

Figure 7.2 shows the experimental results from Lackenby *et al.* (2007), in terms of both axial and volumetric strain against number of loading cycles. For comparison with the simulation results, the experimental results for the first 1,000 cycles are shown in Figure 7.3. Figure 7.4 shows the axial and volumetric strain against number of loading cycles for the simulations, using the breakable and unbreakable assemblies. The number of asperities broken off as a function of the number of cycles under different maximum deviator stresses in the simulations is shown in Figure 7.5.

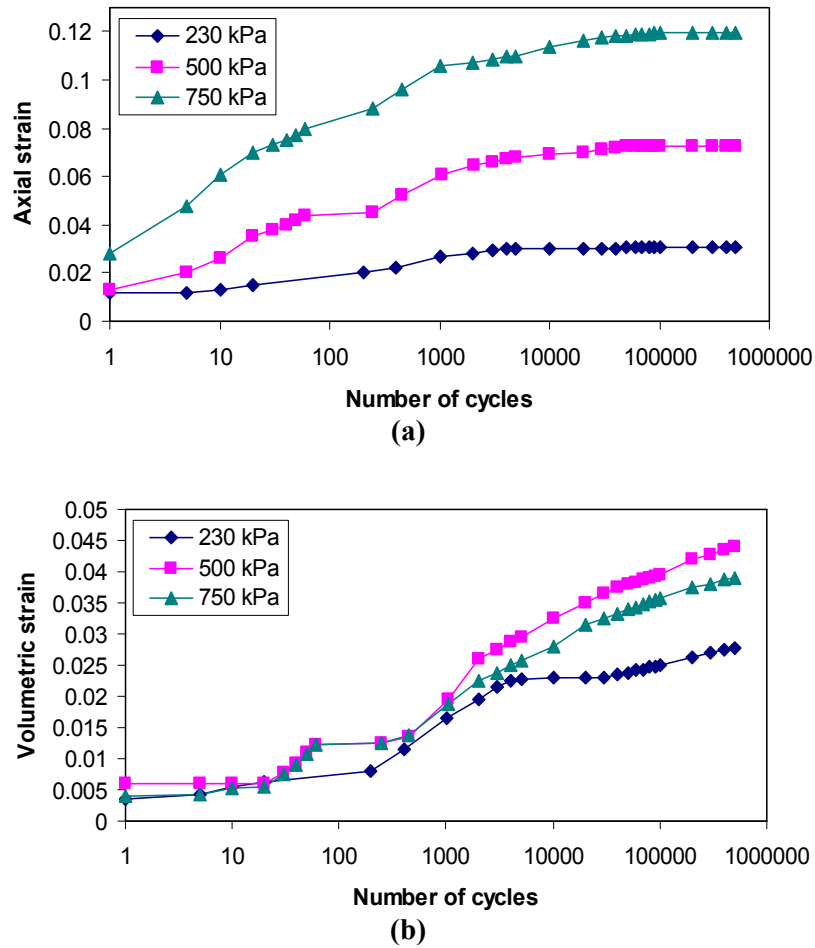
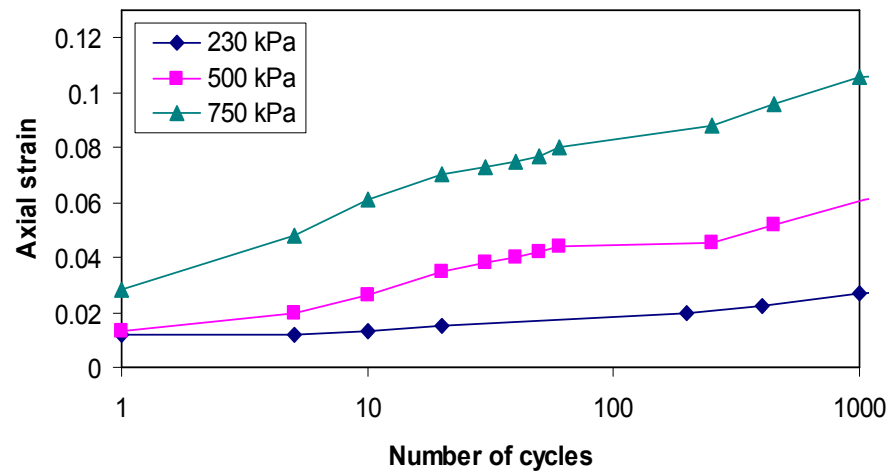
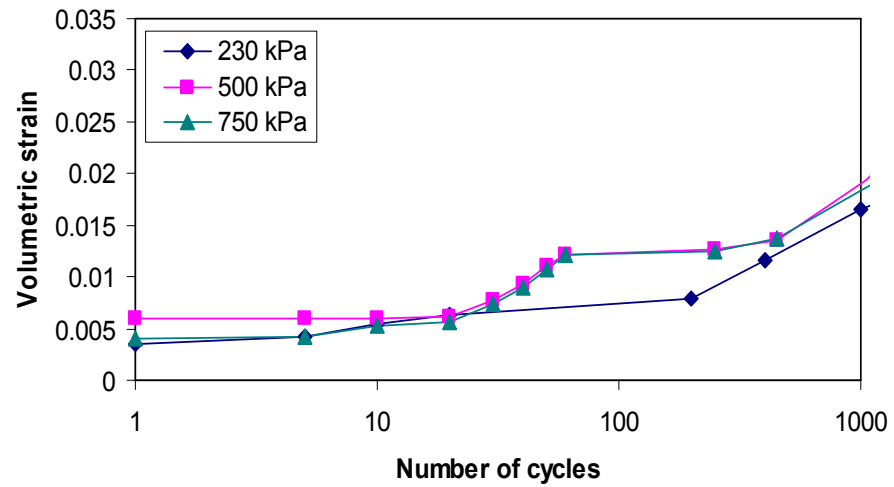


Figure 7.2. (a) Axial strain and (b) volumetric strain (contraction positive) under a confining pressure of 120 kPa against number of cycles (Lackenby *et al.*, 2007).

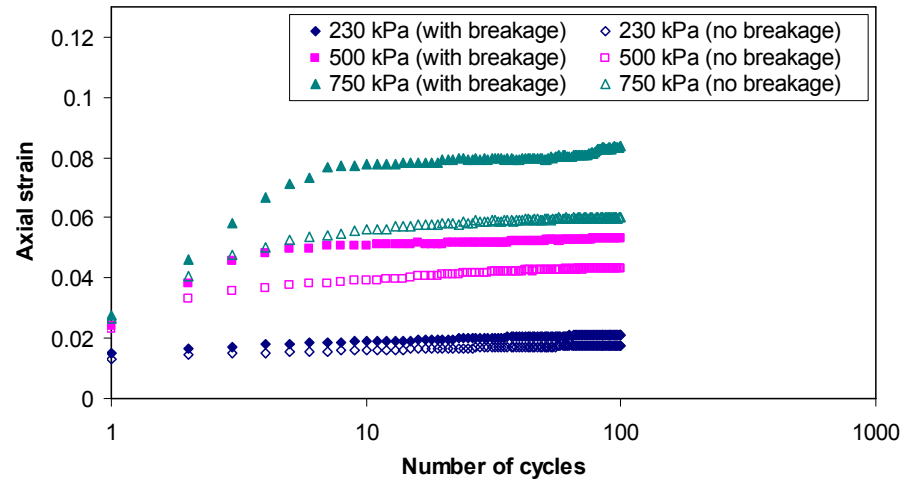


(a)

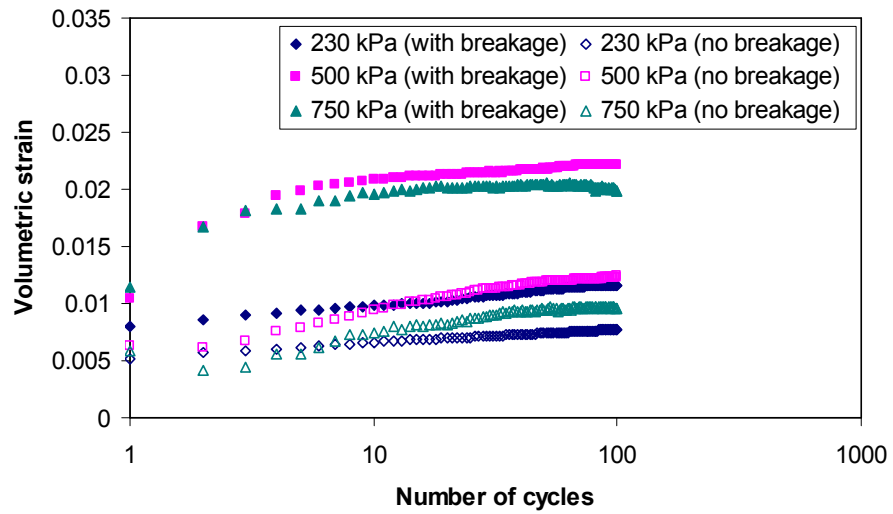


(b)

Figure 7.3. (a) Axial strain and (b) volumetric strain (contraction positive) under a confining pressure of 120 kPa during the first 1,000 cycles (Lackenby *et al.*, 2007).



(a)



(b)

Figure 7.4. (a) Axial strain and (b) volumetric strain (contraction positive) for both breakable and unbreakable assemblies under a confining pressure of 120 kPa against number of cycles.

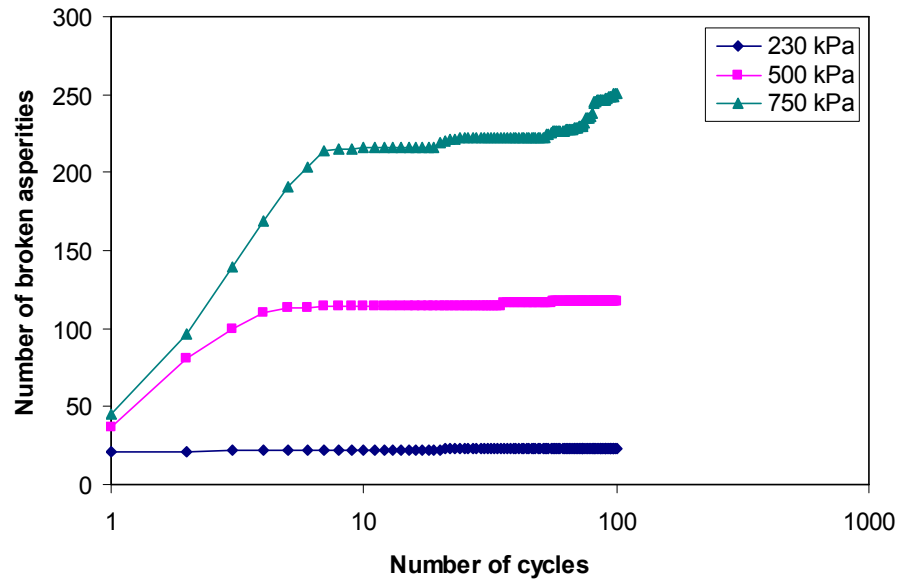


Figure 7.5. Number of asperities broken off under a confining pressure of 120 kPa against number of cycles.

It can be seen from Figure 7.3(a) that, for the real ballast assembly, the rate of increase of axial strain is very high in the first 1,000 cycles, especially for high maximum deviator stresses (i.e. $q_{\max, \text{cyc}} = 500 \text{ kPa}$ and 750 kPa). Lackenby *et al.* (2007) found that real ballast shakes down (i.e. there is an insignificant rate of increase of axial strain) within 10,000 cycles, as shown in Figure 7.2(a). However, it can be seen from Figure 7.4(a) that for the simulations, the main axial strain accumulated during the first 10 cycles, with only a few axial strain increments occurring during the remaining 90 cycles. It would appear that, for the simulations, permanent axial strain accumulation stabilises, and the assembly shakes down within 100 cycles, presumably because of the limited number of asperities. In addition, fatigue or slow crack growth is not considered in these simulations.

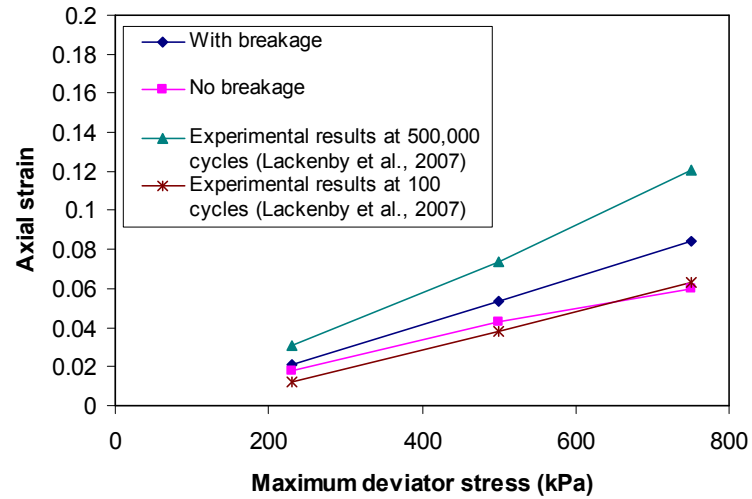
It can be seen from Figure 7.5 that the number of asperities broken off increases with increasing maximum deviator stress, with the number of asperities broken off under a maximum deviator stress of 750 kPa being about ten times higher than that under a maximum deviator stress of 230 kPa. For the simulation using a maximum deviator stress of 230 kPa, most asperity breakage occurs during the first few cycles. For the simulation using a maximum deviator stress of 750 kPa, a large number of asperity breakages occurs during the first 10 cycles with asperities still breaking off, however, during the remaining 90 cycles.

Comparing the breakable assembly with the unbreakable, a higher axial strain is observed for the breakable assembly for each of the different maximum deviator stresses (as shown in Figure 7.4(a)). Axial strain increases very little during the remaining 90 cycles when using the unbreakable assembly under a maximum deviator stress of 750 kPa. By comparison, a larger axial strain was observed during the remaining 90 cycles for the breakable assembly under a maximum deviator stress of 750 kPa due to asperities still breaking off during the remaining 90 cycles, leading to additional permanent axial strain. When particle abrasion is omitted from the simulation, particle rearrangement decreases and the assembly shakes down in a few cycles. However, when particle abrasion is modelled, asperity breakage leads to more particle rearrangement and hence extra permanent axial strain. Thus, a greater number of cycles is needed for the breakable assembly to shake down.

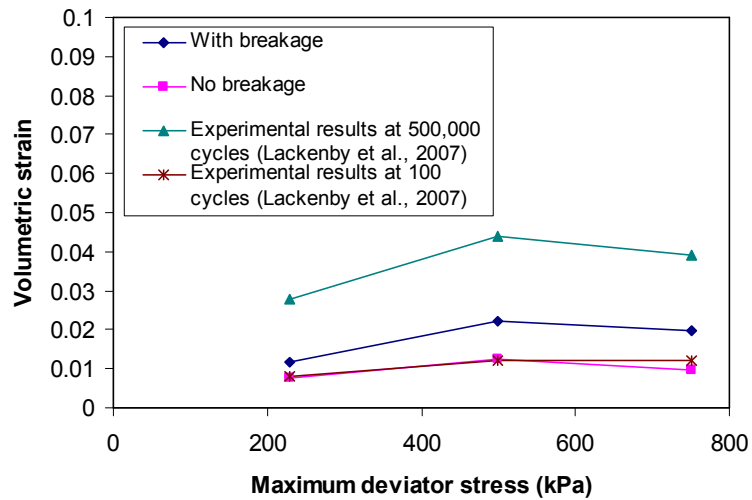
Figure 7.6 shows the axial and volumetric strain after 100 cycles for the simulations using the breakable and unbreakable assemblies. The axial and

volumetric strain after 100 cycles and the final axial and volumetric strain for the experimental results are also plotted in the same figure for comparison. It should be noted that the accumulated axial strain is a function of the number of cycles before an assembly shakes down and that the number of cycles required depends on the loading conditions. Due to the limitation of simulation (e.g. number of asperities, ignoring the effect of fatigue and slow cracking), the assembly in the simulations stabilises more quickly than the real ballast. After 100 cycles, the assembly in the simulations is stable, while real ballast is not (with accumulated axial strain still increasing significantly). It is clear from Figure 7.6 that a larger axial strain and greater contraction are observed when the breakable clumps are used comparing with those using unbreakable, particularly under high maximum deviator stresses where a large number of asperities breaks off. It can be seen from Figure 7.6 that the axial strain for both simulations and experimental tests increase with increasing maximum deviator stress and that the volumetric strain for both simulations and experimental tests peaks for a maximum deviator stress of 500 kPa and then decreases at $q_{\max, \text{cyc}} = 750$ kPa. Comparing the simulations using breakable clumps with those using unbreakable, the axial and volumetric strain for the unbreakable assemble are closer to the experimental results after 100 cycles, however, the axial and volumetric strain for the breakable assemble are closer to the final experimental results. This is due to the more rapid stabilising of the assembly in the simulation than in real ballast under the same number of cycles and the effect of particle abrasion on axial and volumetric strain. The rapid stabilising of the assembly in the simulation leads to a higher axial and volumetric

strain, while the unbreakable assembly causes insufficient permanent deformation (i.e. axial and volumetric strain).



(a)



(b)

Figure 7.6. (a) Axial strain and (b) volumetric strain (contraction positive) after 100 cycles for simulations and experimental tests, and after 500,000 cycles for experimental tests.

7.4 Modelling Railway Ballast Behaviour under a Large Range of Confining Pressures

7.4.1 Axial and volumetric strain

A series of triaxial test simulations using a crushable assembly were carried out under the different loading conditions used by Lackenby *et al.* (2007). The loading conditions are given in Table 7.4. Figures 7.7 and 7.8 show the experimental results, in terms of axial and volumetric strain against number of cycles. For comparison with the simulation results, the experimental results for the first 1,000 cycles are shown in Figures 7.9 and 7.10. Figures 7.11 and 7.12 show the axial and volumetric strain against number of cycles for the simulations under different loading conditions. The number of asperities broken off in the simulations as a function of the number of cycles is plotted in Figure 7.13.

As for the simulations in Series 7.1, most assemblies in Series 7.2 shake down within 100 cycles, apart from the assemblies with a relatively low confining pressure and high maximum deviator stress. It is clear from Figure 7.11 that only Simulation 7.11 (confining pressure of 30 kPa and maximum deviator stress of 750 kPa) failed within 100 cycles. This is consistent with the experimental data (Lackenby *et al.*, 2007) which shows that under a confining pressure of 30 kPa and maximum deviator stress of 750 kPa the specimen failed (i.e. axial strain > 0.25) rather than shook down.

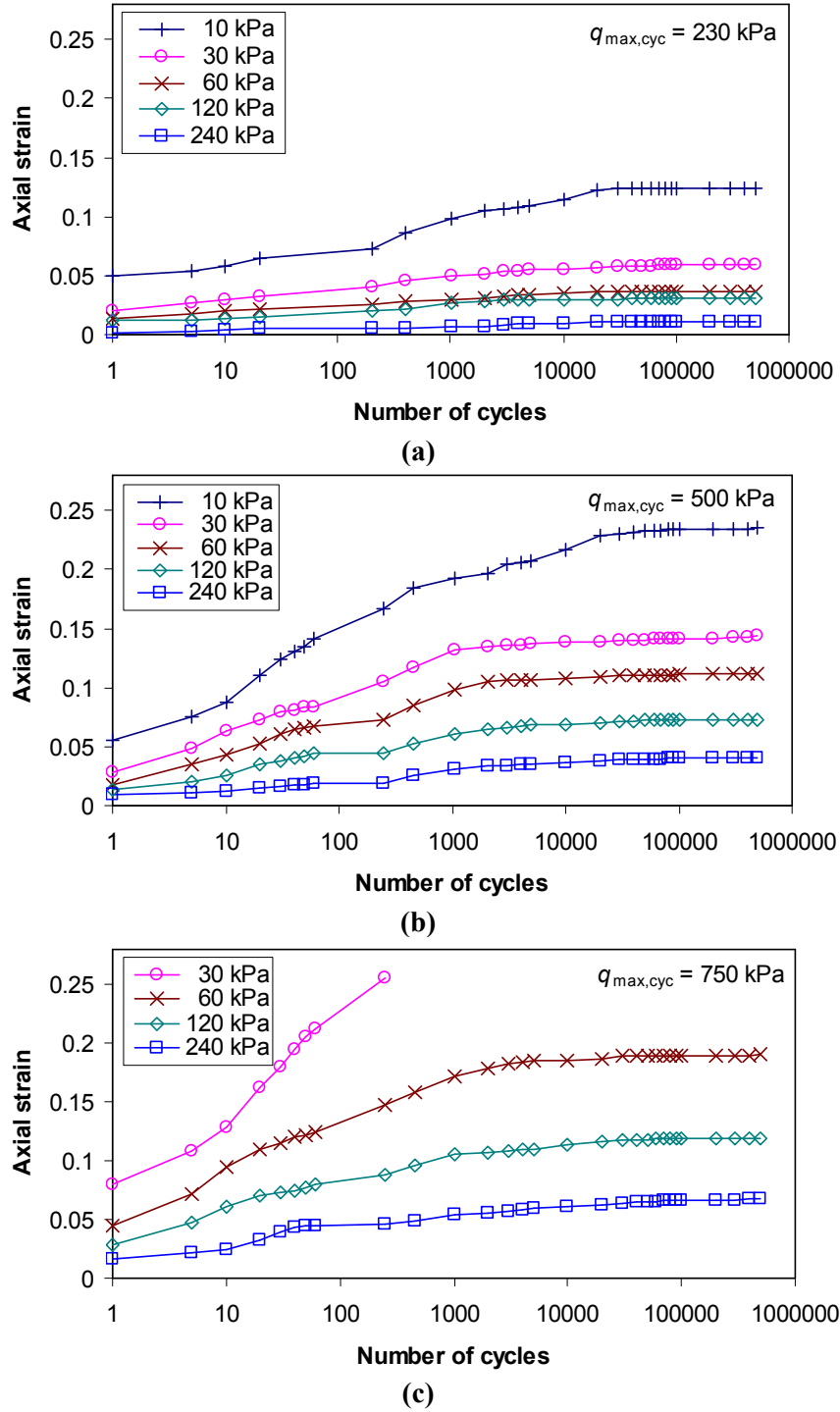
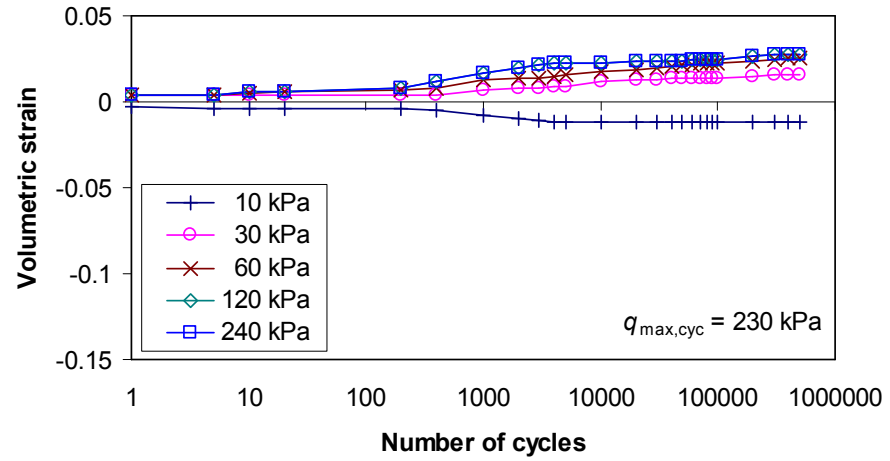
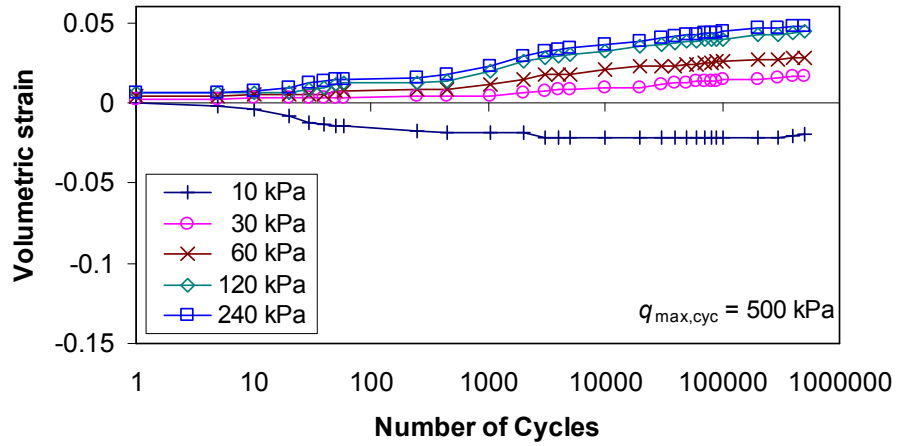


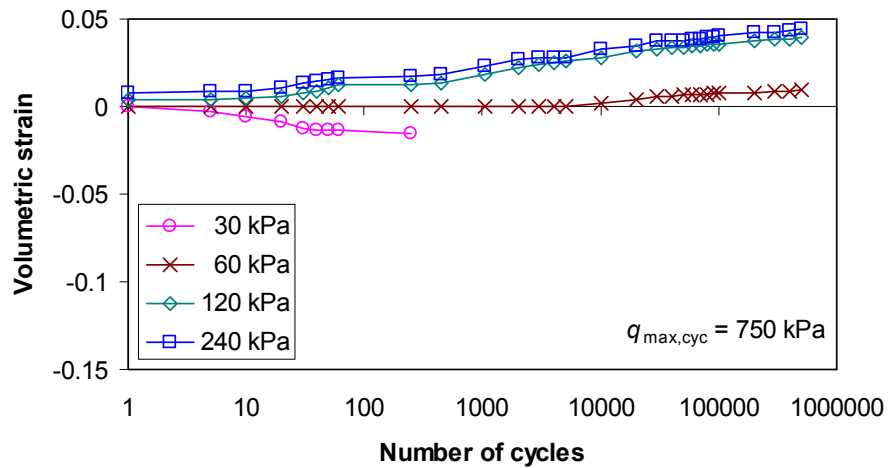
Figure 7.7. Axial strain as a function of the number of cycles (Lackenby *et al.*, 2007).



(a)

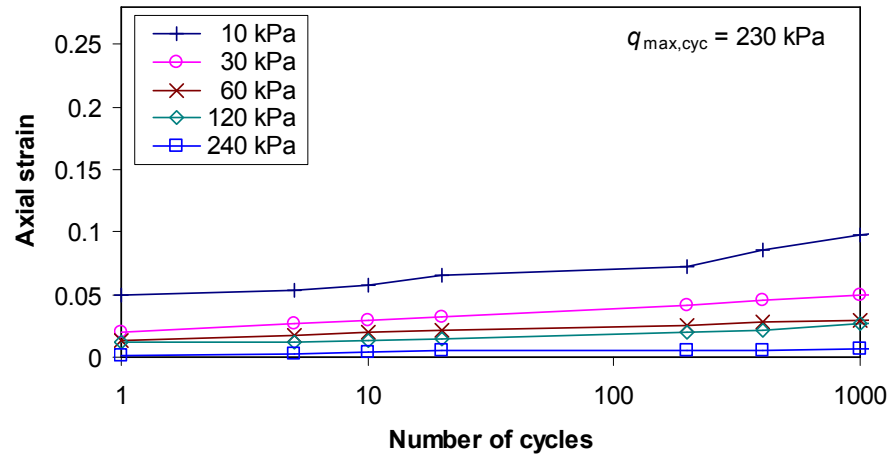


(b)

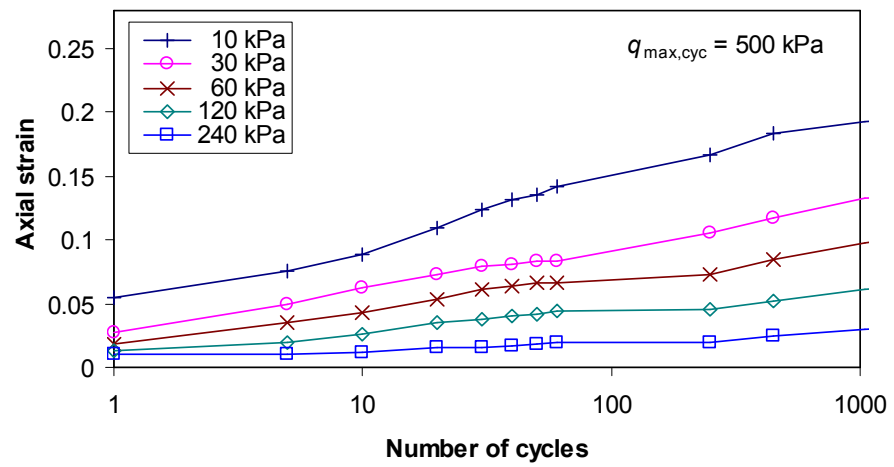


(c)

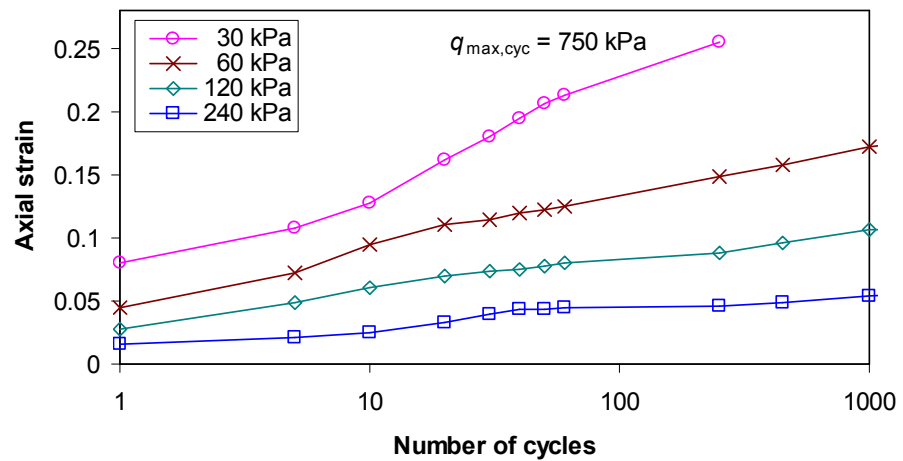
Figure 7.8. Volumetric strain (contraction positive) as a function of the number of cycles (Lackenby *et al.*, 2007).



(a)

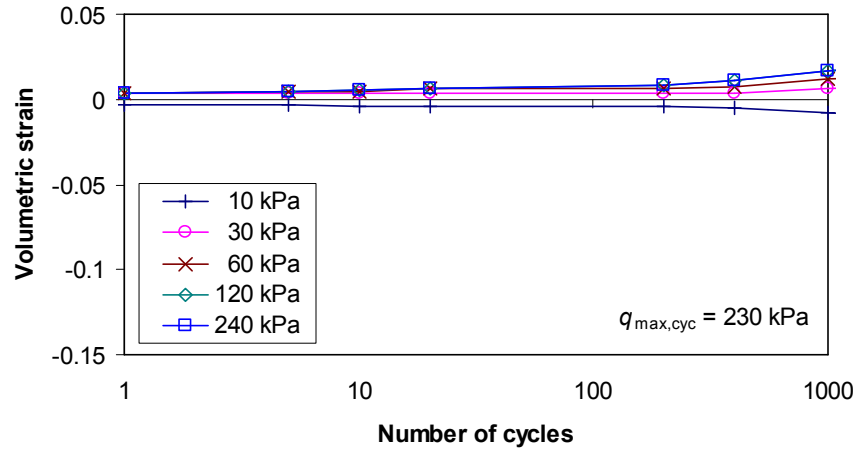


(b)

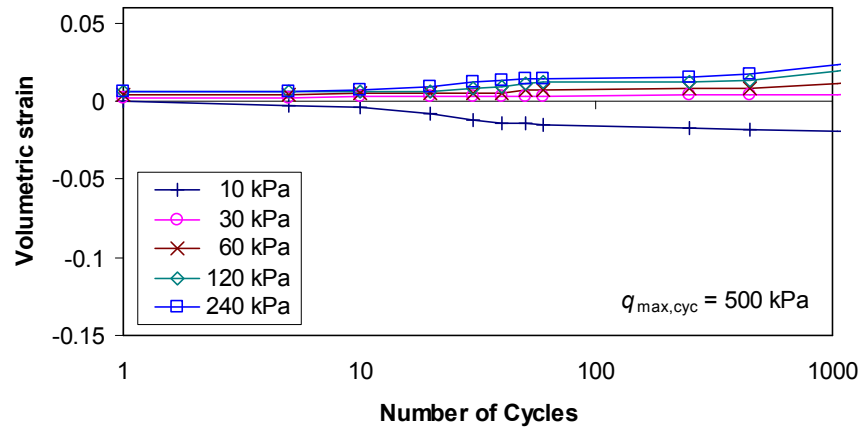


(c)

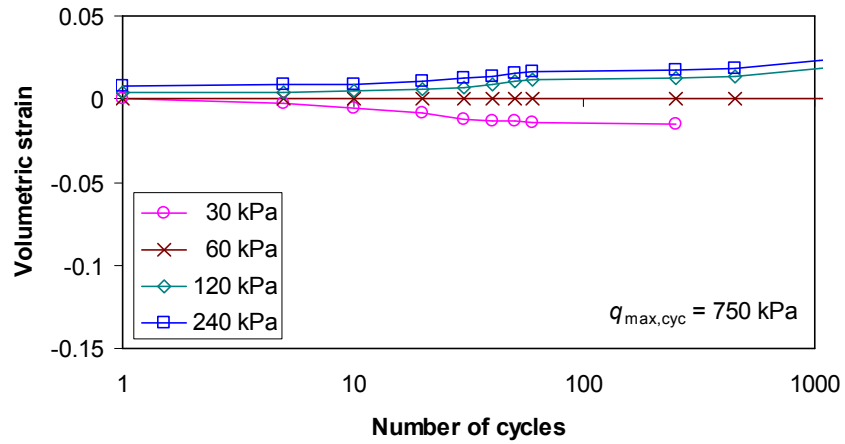
Figure 7.9. Axial strain during the first 1,000 cycles (Lackenby *et al.*, 2007).



(a)



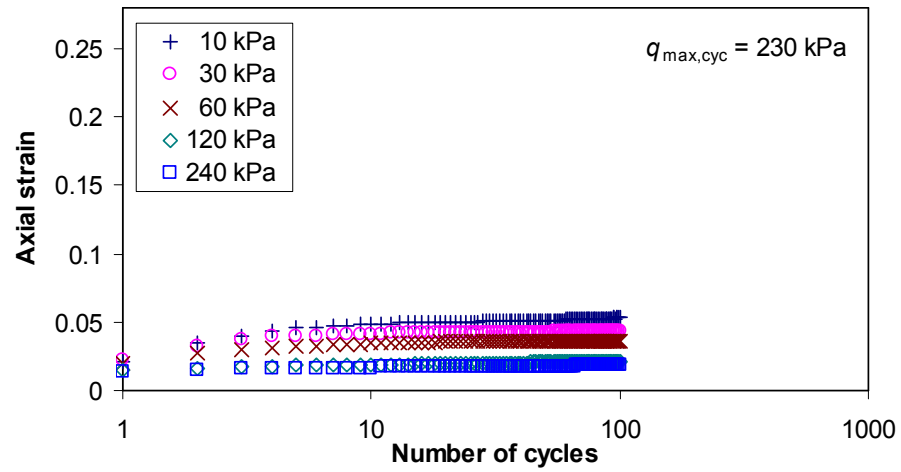
(b)



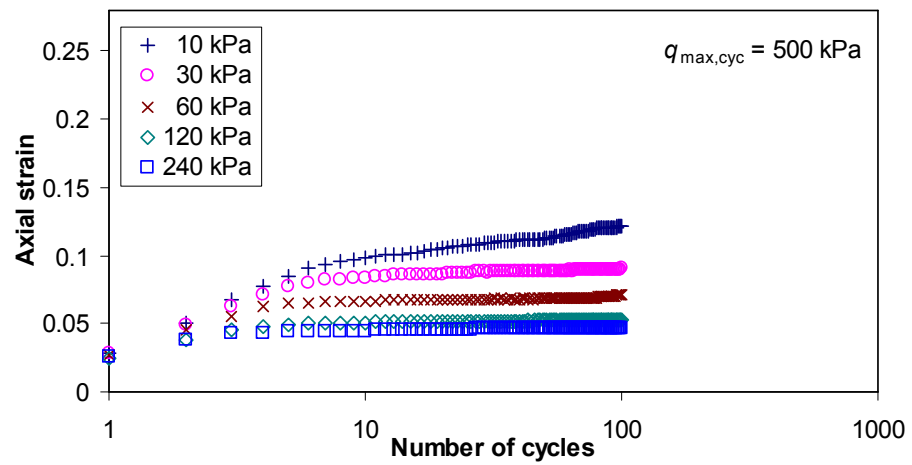
(c)

Figure 7.10. Volumetric strain (contraction positive) during the first 1,000 cycles

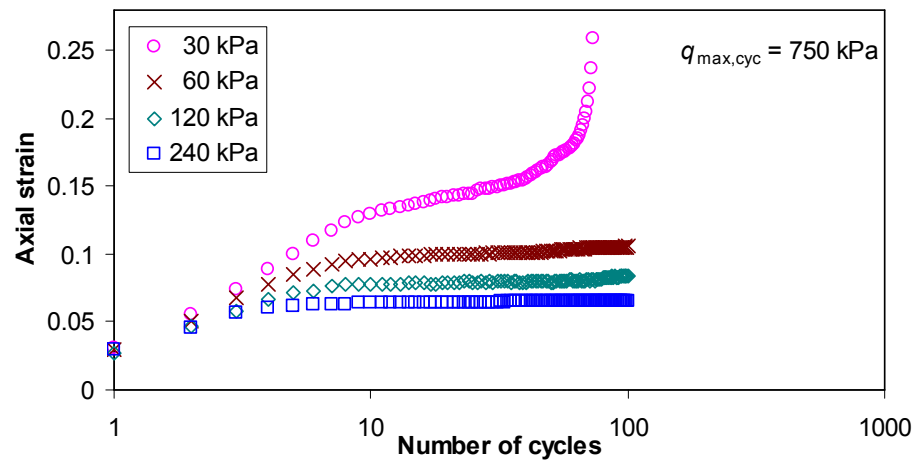
(Lackenby *et al.*, 2007).



(a)



(b)



(c)

Figure 7.11. Axial strain as a function of the number of cycles for the simulations.

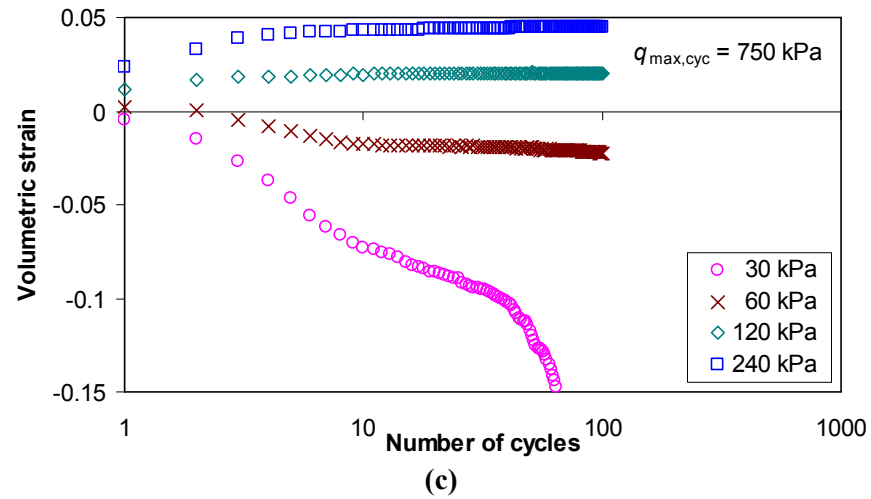
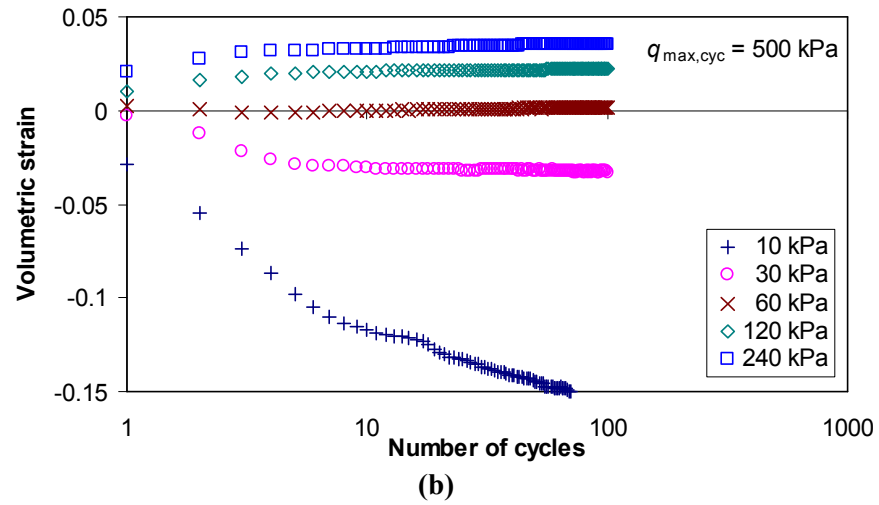
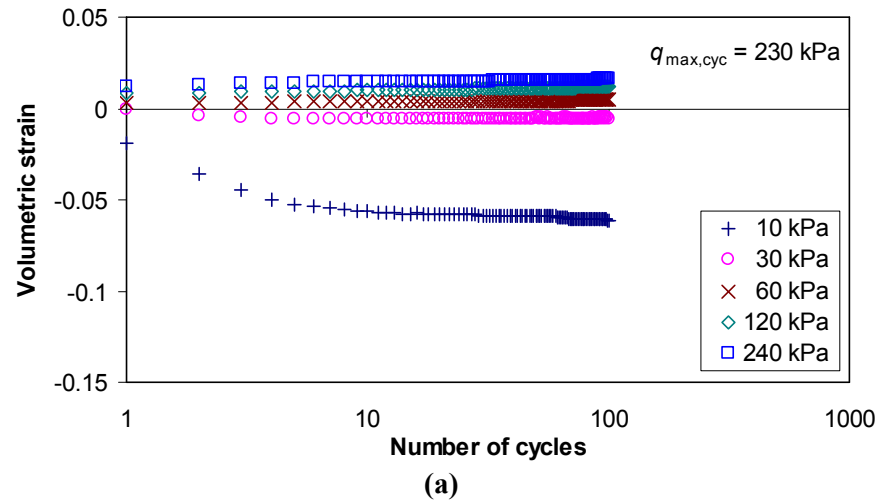


Figure 7.12. Volumetric strain (contraction positive) as a function of the number of cycles for the simulations.

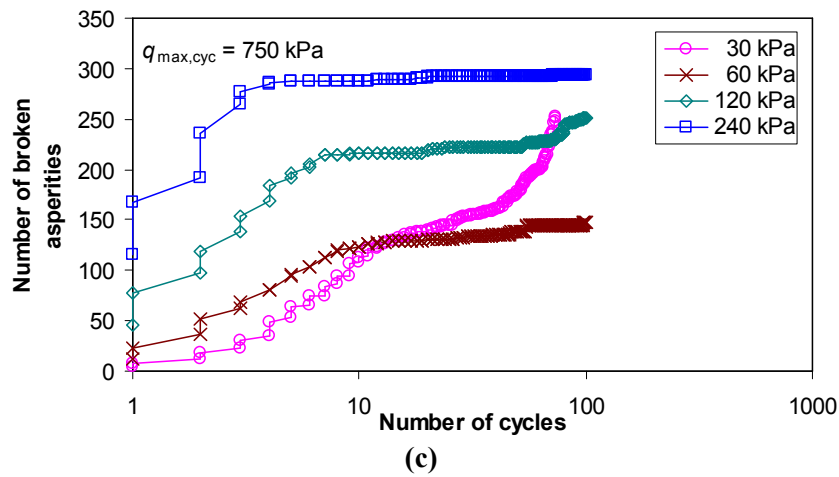
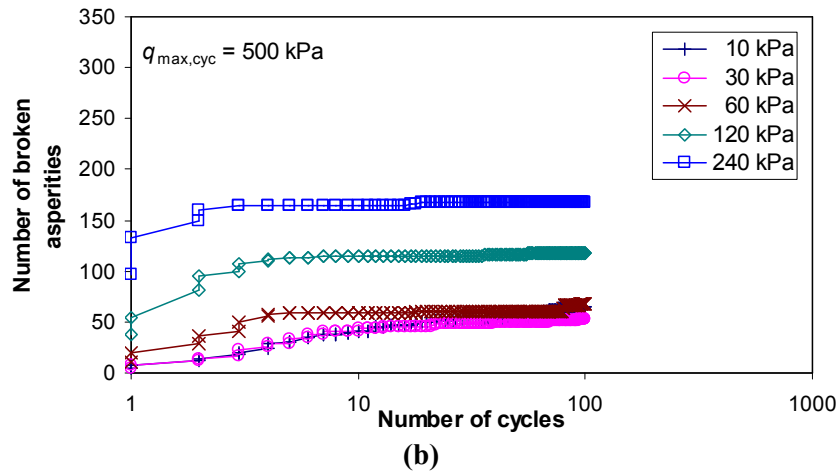
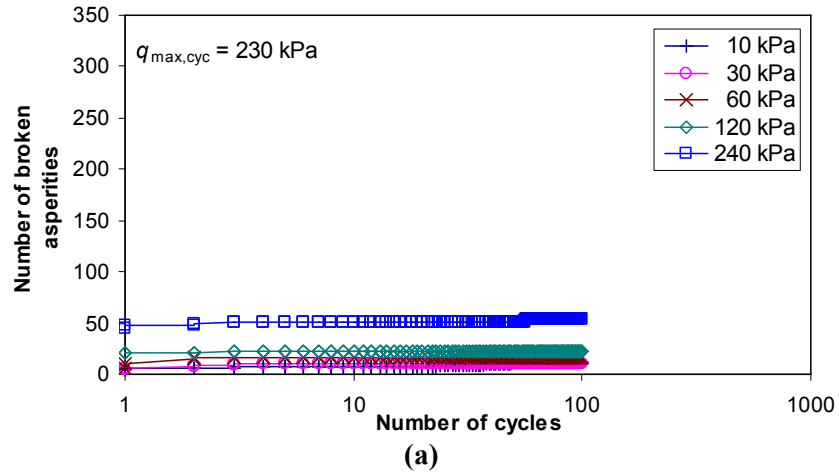


Figure 7.13. Number of asperities broken off against number of cycles.

It can be seen from Figure 7.11 that axial strain increases with increasing maximum deviator stress and decreasing confining pressure. Similar behaviour was reported in the experiments by Lackenby *et al.* (2007). Comparing the simulation results with the experimental results (as shown in Figure 7.7), permanent axial strain was simulated effectively. With reference to the volumetric strain (Figures 7.8 and 7.12, contraction positive), higher dilation was observed for the simulations with relatively low confining pressure and high maximum deviator stress than for the laboratory tests. This is similar to the results from the monotonic triaxial test simulations presented in Chapter 6, where higher dilation was observed under low confining pressures (i.e. 15 kPa and 30 kPa) than in the experimental data.

Figure 7.14(a) shows a plot of final axial strain after 500,000 cycles for experimental tests against confining pressure. Figures 7.14(b) and (c) show plots of axial strain after 100 cycles for experimental tests and simulations respectively, against confining pressure. Lackenby *et al.* (2007) used Equation 7.1 to describe the influence of confining pressure on axial strain.

$$\varepsilon_a = a\sigma_3'^{-b} \quad (7.1)$$

where a and b are regression coefficients listed in Table 7.6. Equation 7.1 with different regression coefficients are plotted as dotted lines in Figure 7.14. Figure 7.15(a) shows a plot of volumetric strain after 500,000 cycles for experimental tests against confining pressure. Figures 7.15(b) and (c) show plots of volumetric strain after 100 cycles for experimental tests and simulations respectively, against

confining pressure. It should be noted that for the experimental results after 100 cycles (as shown in Figures 7.14(b) and 7.15(b)), the specimens have not shaken down.

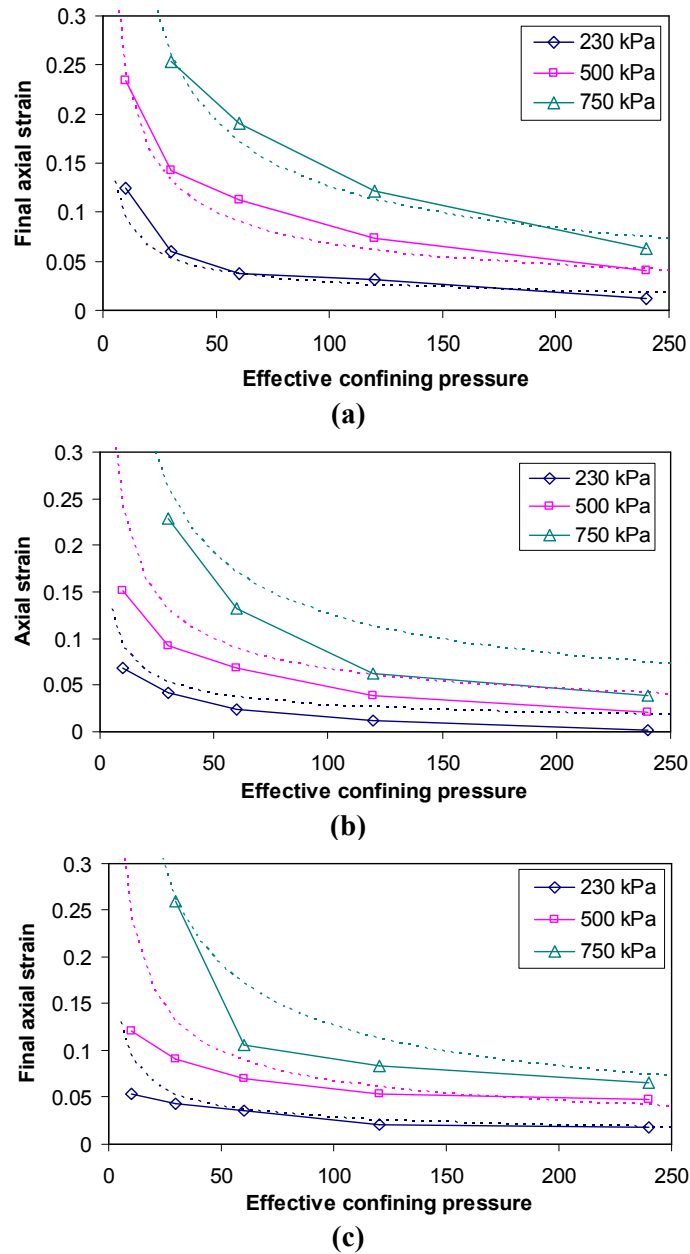
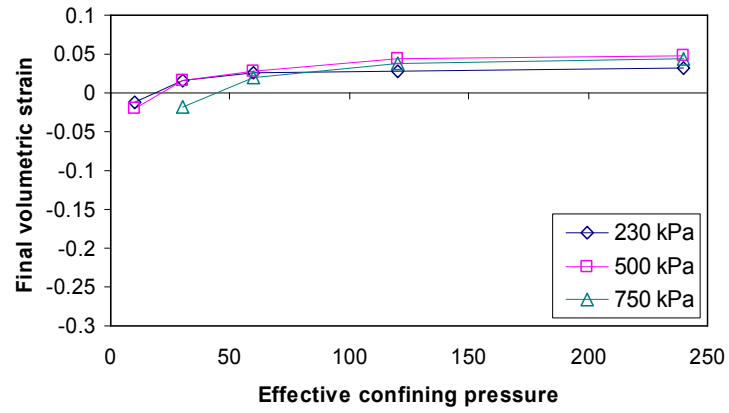
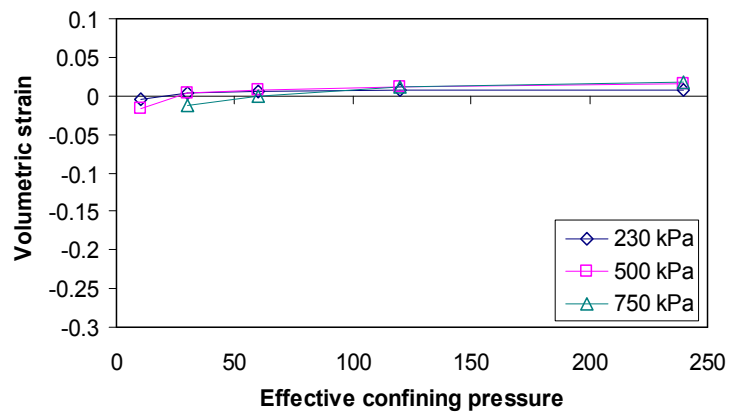


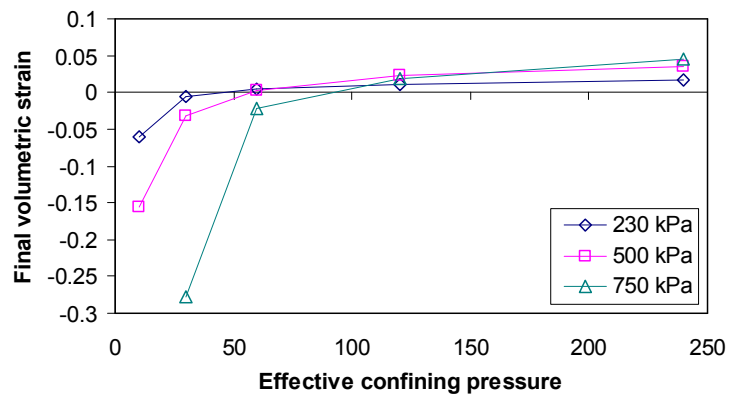
Figure 7.14. Axial strain against confining pressure: (a) experimental results at 500,000 loading cycles (Lackenby *et al.*, 2007); (b) experimental results at 100 loading cycles (Lackenby *et al.*, 2007) and (c) simulation results.



(a)



(b)



(c)

Figure 7.15. Volumetric strain (contraction positive) against confining pressure: (a) experimental results at 500,000 loading cycles (Lackenby *et al.*, 2007); (b) experimental results at 100 loading cycles (Lackenby *et al.*, 2007) and (c) simulation results.

$q_{\max, \text{cyc}}$ (kPa)	a	b
230	0.30	0.51
500	0.85	0.55
750	2.00	0.60

Table 7.6. Regression coefficients for Equation 7.1 (Lackenby *et al.*, 2007).

Comparing the simulation results with the experimental results after 100 cycles, it was found that axial strains for simulations are higher than for the experiment results, apart from the simulations with 10 kPa confining pressure. This is due to the more rapid stabilising of the assembly in the simulation than in real ballast under the same number of cycles. Simulation 7.11, for example, failed within 100 cycles, while the experimental specimen under the same loading condition failed after 200 cycles; therefore, the axial strain for Simulation 7.11 (as shown in Figure 7.14(c)) is found to be higher than in the experimental one (as shown in Figure 7.14(b)). Regarding volumetric strain, the assembly in the simulations is more contractive under high confining pressures and more dilative under low confining pressures in comparison with the experimental results after 100 cycles.

Comparing the simulation results after 100 cycles with the experimental results after 500,000 cycles, for high confining pressures (i.e. confining pressures of 120 kPa and 240 kPa), axial strains for simulations match those for the experimental results. For low confining pressures (i.e. confining pressures of 10 kPa to 60 kPa), axial strains for the simulations are lower than those for the experimental tests, particularly under high maximum deviator stresses. Regarding volumetric strain,

when the specimen is contractive (under higher confining pressures), the simulation results are consistent with the experimental results. However, when the specimen is dilative (under low confining pressure), higher dilation is observed in the simulations. As discussed in section 6.5.1, this is probably due to the arbitrary number of asperities bonded on each clump and the asperity size. Smaller asperities may break at lower levels giving more asperity breakage and less dilation.

7.4.2 Strain behaviour as a function of ψ

Lackenby *et al.* (2007) introduced the ratio of maximum deviator stress for cyclic loading to the peak strength obtained from monotonic triaxial tests ψ , as described in Equation 7.2.

$$\psi = q_{\max, \text{cyc}} / q_{\text{peak}, \text{sta}} \quad (7.2)$$

They found that final axial strain is confined within a narrow band of values when plotted against the ratio ψ . Equation 7.3 was used to describe this.

$$\varepsilon_a = \alpha + \beta\psi \quad (7.3)$$

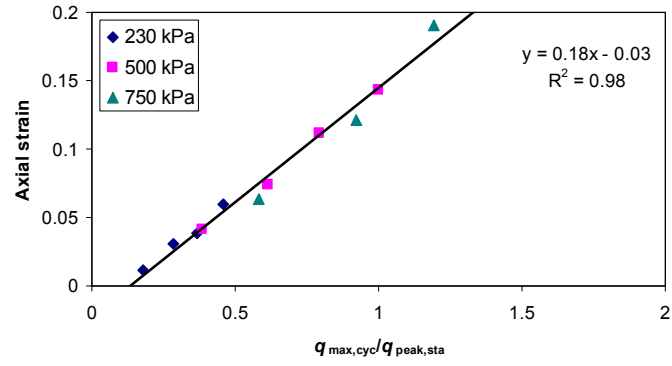
where α and β are regression coefficients.

Figures 7.16(a) and (b) show the plot of axial strain after 500,000 cycles and 100 cycles, respectively, against the ratio ψ for experimental tests. Figure 7.16(c) shows the plot of axial strain after 100 cycles against the ratio ψ for the simulations. It can be seen that for the simulations, the relationship between axial

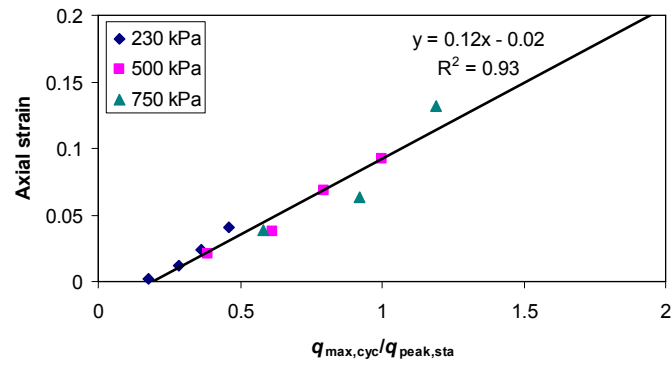
strain after 100 cycles and the ratio ψ is also confined within a narrow band. It should be noted that the slope of the narrow band is affected by the number of cycles (as shown in Figures 7.16(a) and (b)). Due to the peak strength obtained from the monotonic triaxial test simulations and the axial strain from the cyclic triaxial test simulations are slightly different from those of experimental results, the slope of the narrow band for simulations differs from that for experimental tests.

7.4.3 Number of contacts

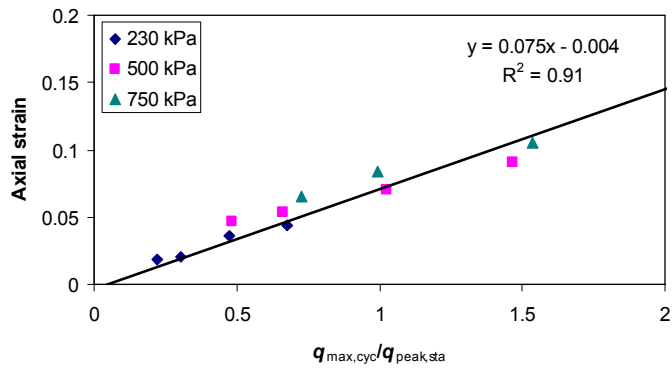
Figure 7.17 shows the number of contacts prior to cyclic loading and under different maximum deviator stresses and confining pressures at the 100th cycle. The number of contacts after shearing (i.e. axial strain = 0.2) for the monotonic triaxial test simulations is plotted in the same figure, and the ultimate strengths are also stated. It can be seen that, as in the monotonic triaxial test results, the number of contacts increases with increasing confining pressure. For the simulations under low confining pressure (<60 kPa), the number of contacts decreases with increasing maximum deviator stress; however, for the simulations under high confining pressure (>60 kPa), the number of contacts increases with increasing maximum deviator stress. It is interesting to compare the number of contacts with the volumetric strain, as shown in Figure 7.15(c). When the number of contacts after 100 cycles is lower than the initial number, the assembly has dilated. The reverse behaviour is observed when the number of contacts after 100 cycles is higher than the initial number: the sample has contracted.



(a)



(b)



(c)

Figure 7.16. Axial strain against the ratio of maximum deviator stress under cyclic loading to maximum deviator stress under monotonic loading (a) experimental results at 500,000 loading cycles (Lackenby *et al.*, 2007); (b) experimental results at 100 loading cycles (Lackenby *et al.*, 2007) and (c) simulation results.

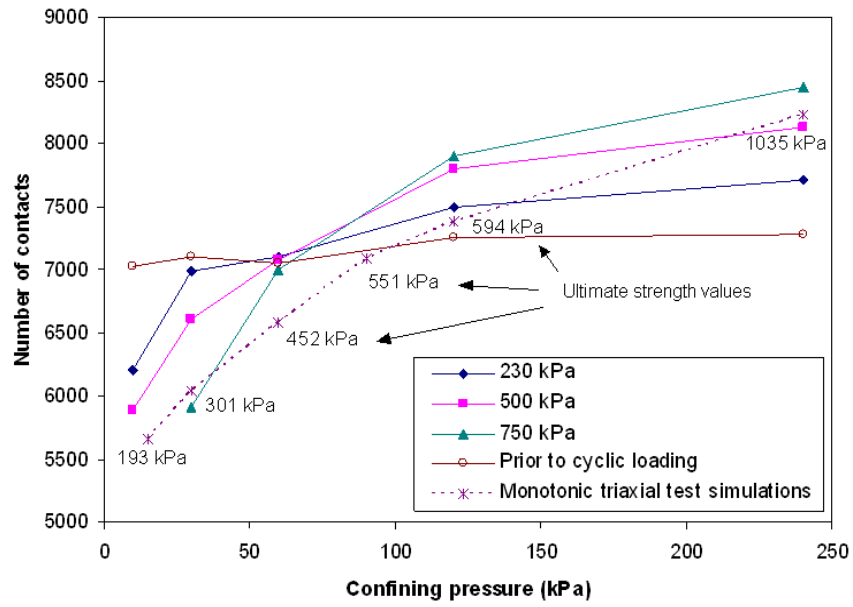


Figure 7.17. Number of contacts for both cyclic and monotonic triaxial test simulations.

As mentioned in section 6.5, the change in the number of contacts is due to the particle breakage and rearrangement. It is apparent from Figure 7.17 that, under low confining pressure, although more asperities break off under higher maximum deviator stress, the number of contacts is lower than that under lower maximum deviator stress. This indicates that under low confining pressure, asperity breakage permits further dilation.

Comparing with the number of contacts for the monotonic triaxial test simulations, as shown in Figure 7.17, more contacts form under cyclic loading with similar confining pressure and deviator stress (deviator stress at 0.2 axial strain for monotonic triaxial test simulations and maximum deviator stress for cyclic triaxial test simulations). Looking at the monotonic test with an ultimate strength of 193 kPa, for example, and the cyclic data at maximum deviator stress of 230 kPa and

500 kPa, it is evident that under a maximum cyclic deviator stress of 193 kPa, the number of contacts would be higher and the assembly would be less dilative, giving a lower average contact force.

7.4.4 Cyclic degradation behaviour

Figure 7.18 shows the ballast breakage index after 500,000 cycles for the experimental tests. This index indicates the breakage level based on a calculation of area under the particle size distribution before and after each test (the detail was described in Chapter 2). The higher the ballast breakage index, the more breakage in the specimen. Figure 7.19 shows the number of asperities broken off after 100 cycles for the simulations. Figure 7.20 shows the number of broken parallel bonds between clumps (modelling very small asperities) after 100 cycles for the simulations.

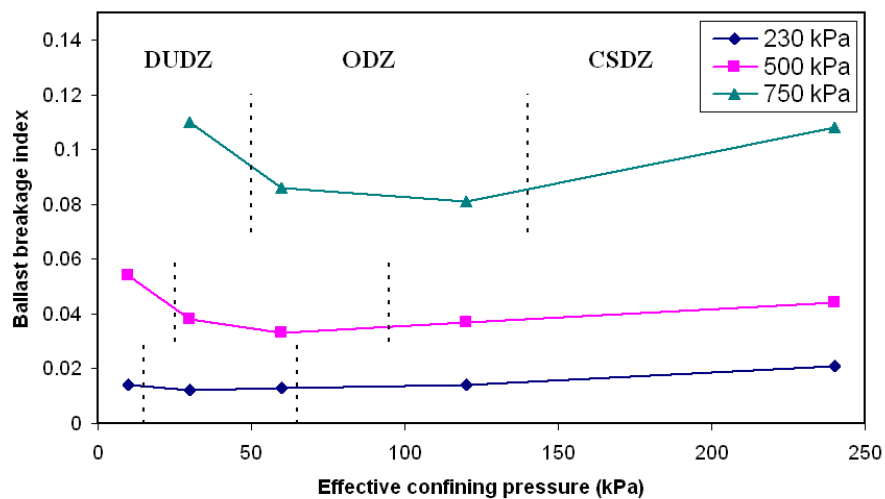


Figure 7.18. Effect of confining pressure and maximum deviator stress on ballast breakage index (Lackenby *et al.*, 2007).

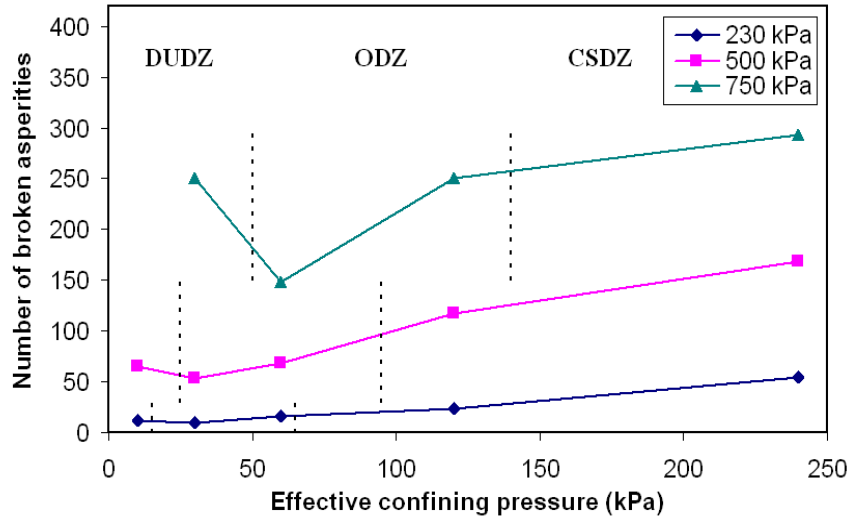


Figure 7.19. Number of broken asperities against confining pressure.

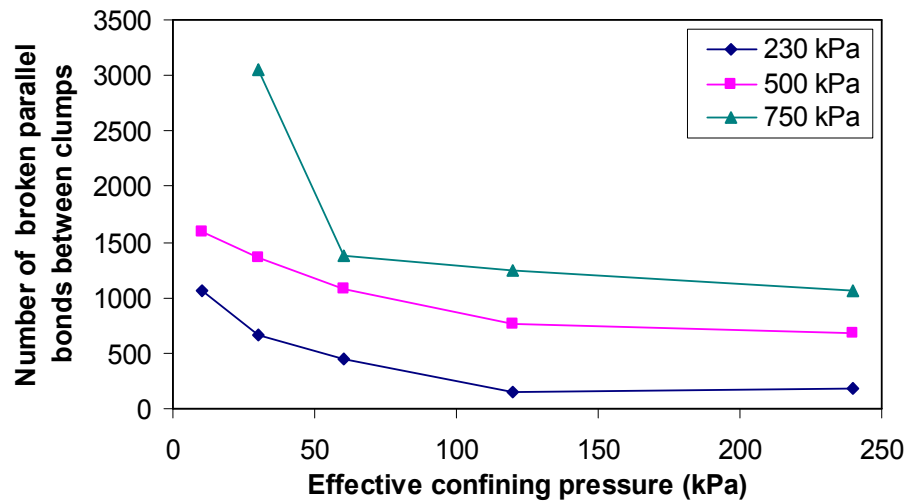


Figure 7.20. Number of broken parallel bonds between clumps against confining pressure.

Indraratna *et al.* (2005) indicated that ballast degradation behaviour under cyclic loading can be categorised into three distinct zones: the dilatant unstable degradation zone (DUDZ), the optimum degradation zone (ODZ), and the

compressive stable degradation zone (CSDZ), as shown in Figure 7.18. These zones are dependent on both confining pressure and maximum deviator stress acting on the specimen (Lackenby *et al.*, 2007). The upper limits of confining pressure for DUDZ and ODZ are listed in Table 7.7. These three distinct zones are also apparent in the simulation, as shown in Figure 7.19 (which has the Lackenby *et al.* (2007) zones superimposed). Regarding parallel bonds between clumps (which simulate the small-scale asperities), it can be seen from Figure 7.20 that a large number of parallel bonds between clumps have broken under a low confining pressure (DUDZ) and that the number of broken parallel bonds decreases with decreasing maximum deviator stress and increasing confining pressure.

$q_{\max, \text{cyc}}$ (kPa)	σ'_3 upper limits (kPa)	
	DUDZ	ODZ
230	15	65
500	25	95
750	50	140

Table 7.7. Upper limits of confining pressure for DUDZ and ODZ (Lackenby *et al.*, 2007).

Lackenby *et al.* (2007) found that most of the degradation in DUDZ was due to the breakage of angular corners or projections, rather than particle splitting. They indicated that this is due to internal deformation mechanisms, such as sliding or rolling, which inhibit the formation of permanent interparticle contacts, thus preventing splitting due to excessive stresses. With reference to the simulations, Figures 7.19 and 7.20 indicate that the fracture of small angular projections

(modelled by bonding asperities) and the grinding off of very small asperities (modelled by parallel bond between clumps) together dominate the behaviour in DUDZ. The considerable fracture of small angular projections and grinding off of small-scale asperities in DUDZ is accompanied by significant particle rolling and sliding.

In the ODZ, Lackenby *et al.* (2007) found that breakage reduces significantly as a result of the increase of confining pressure. In the simulations, both the number of broken asperities and the number of broken parallel bonds between clumps reduce considerably. The reduced particle breakage in this zone is accompanied by less dilation and an increase in the number of contacts.

In the CSDZ, Lackenby *et al.* (2007) found that although corner degradation is still the foremost kind of breakage, some particle splitting takes place. In this research, particle splitting is not simulated as it is computationally very time-consuming to use agglomerates of bonded balls to model particle splitting, and only a little particle splitting is observed in the experimental tests (Lackenby *et al.*, 2007). Future research can address the modelling of particle splitting. Figure 7.20 shows that, in comparison with other zones, fewer parallel bonds between clumps break off. However, more asperities break off in the CSDZ, comparing with those in the ODZ (as shown in Figure 7.19). Under high confining pressure, since the particle movement (i.e. rolling and sliding) and the assembly dilation are largely suppressed as a result of high confinement and an increased number of contacts, the grinding off of very small asperities (modelled by the parallel bonding between clumps) is limited. However, since the mean contact force increases with

increasing confining pressure, the crushing of angular corners and sharp asperities is still significant.

In general, Figures 7.19 and 7.20 suggest that the behaviour observed in Figure 7.18 is dominated by asperity fracture (i.e. the fracture of small angular projections), simulated here by bonding small balls to the clumps.

Figures 7.21-7.25 show the number of broken asperities during 100 cycles for different maximum deviator stresses and confining pressures against axial strain. The number of asperities broken off under monotonic loading is also plotted in these figures in a solid line. As expected, under cyclic loading conditions, more breakage occurs at the same axial strain. It can be seen from these figures that, under the same confining pressure, the number of broken asperities under different maximum deviator stresses against axial strain follows the same curve. Equation 7.4 can be utilised to describe the relationship between number of broken asperities N_{asp} and axial strain ε_a .

$$N_{asp} = c\varepsilon_a^d \quad (7.4)$$

where c and d are regression coefficients listed in Table 7.8.

Confining pressure (kPa)	c	d
10	5,093	2.12
30	8,138	2.11
60	14,290	2.03
120	15,649	1.67
240	16,008	1.45

Table 7.8. Regression coefficients for Equation 7.4.

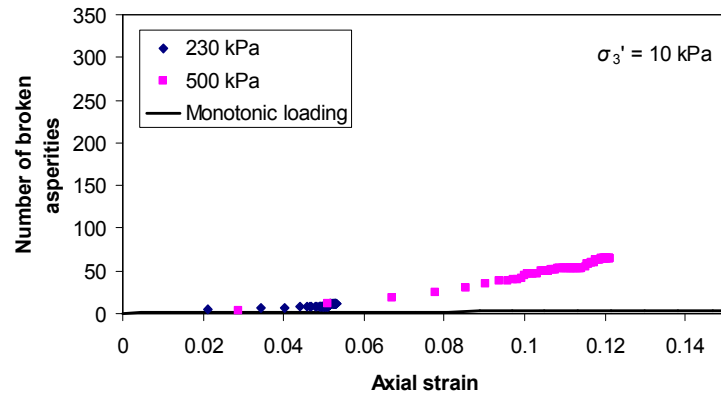


Figure 7.21. Number of broken asperities under a confining pressure of 10 kPa against axial strain.

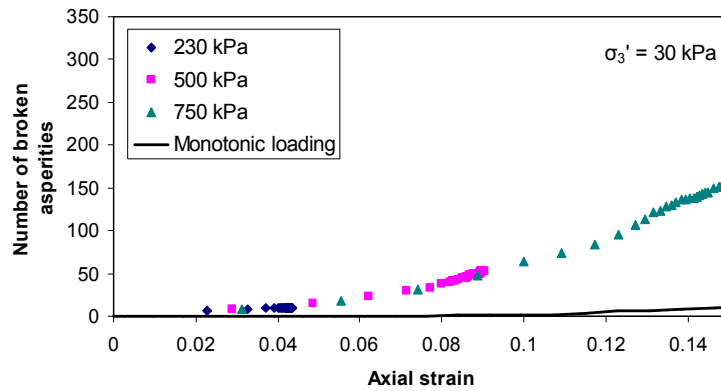


Figure 7.22. Number of broken asperities under a confining pressure of 30 kPa against axial strain.

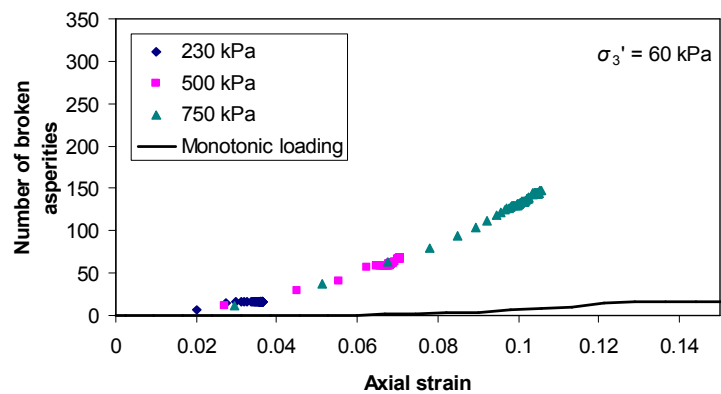


Figure 7.23. Number of broken asperities under a confining pressure of 60 kPa against axial strain.

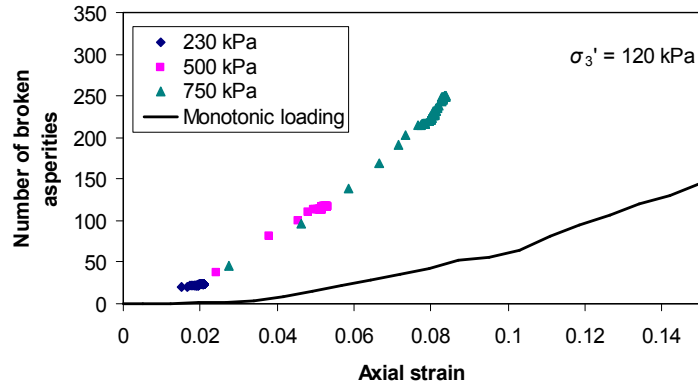


Figure 7.24. Number of broken asperities under a confining pressure of 120 kPa against axial strain.

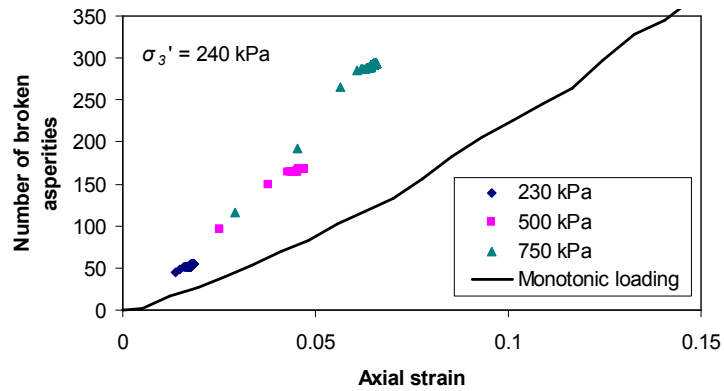


Figure 7.25. Number of broken asperities under a confining pressure of 240 kPa against axial strain.

Figure 7.26 shows Equation 7.4 and the number of broken asperities under different confining pressures. Given axial strain and confining pressure, it is possible to predict the number of broken asperities using Equation 7.4, as shown in Figure 7.27. The number of broken asperities under different confining pressures and maximum deviator stresses after 100 cycles are also plotted in Figure 7.27. By using Equations 7.3 and 7.4, given the confining pressure and the ratio ψ , it is possible to predict the total axial strain and number of broken asperities.

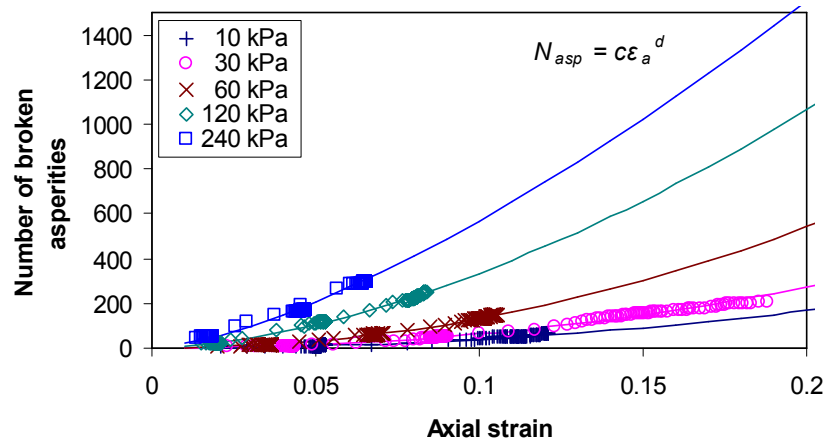


Figure 7.26. Number of broken asperities under confining pressures of 10 kPa to 240 kPa against axial strain.

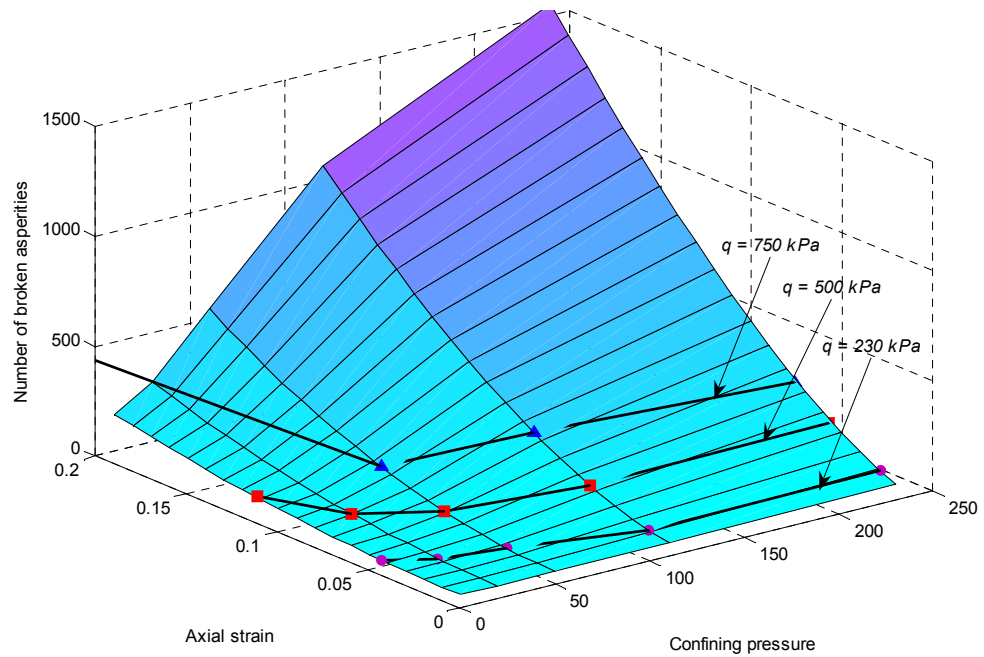


Figure 7.27. 3D plot showing the relationship between confining pressure, axial strain and number of broken asperities.

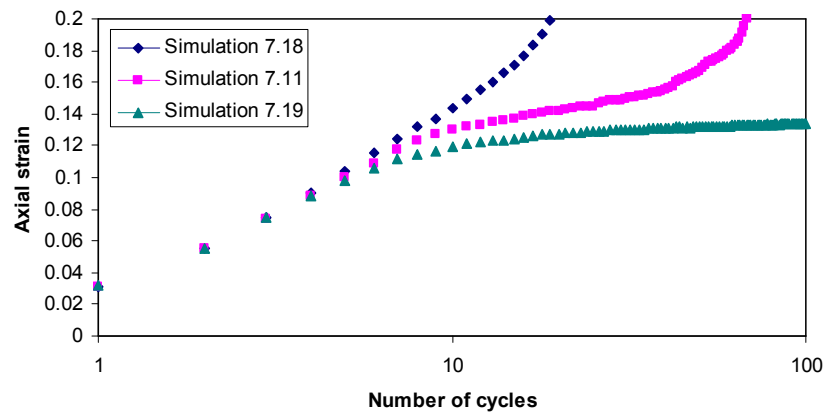
7.5 Effect of Parallel Bond between Clumps

Both the experimental and simulation results have shown that the assemblies fail under a confining pressure of 30 kPa and a maximum deviator stress of 750 kPa. This loading condition was used, therefore, in Series 7.3 to study the effect of parallel bonds between clumps. The parameters for parallel bonds between clumps used in this series of simulations are given in Table 7.5. Figure 7.28 shows the axial and volumetric strain for different parallel bond strengths between clumps against number of cycles. It can be seen that with decreasing parallel bond strength, the axial strain increases more rapidly. For the assembly with low parallel bond strength (Simulation 7.18), axial strain increases with the number of cycles and fails after about 20 cycles. Regarding volumetric strain, for the assembly with low parallel bond strength, it keeps dilating. Nevertheless, for the assembly with high parallel bond strength, it dilates during the first few cycles and then becomes stable.

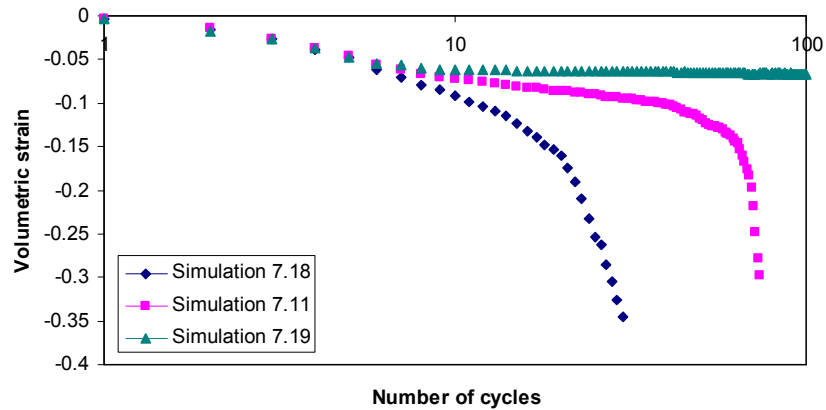
Figure 7.28(a) indicates that, for Simulations 7.18 and 7.11, when the axial strain is higher than 0.17, the rate of increase of axial strain increases sharply and the assemblies fail. However, for Simulation 7.19, where the parallel bond strength is the highest, axial strain and volumetric strain level off after 20 cycles. It appears that the assembly in Simulation 7.19 stabilises within 100 cycles.

Figure 7.29 shows the number of parallel bonds between clumps broken off during the 100 cycles. Figure 7.30 shows the number of asperities broken off during the 100 cycles. As expected, the lower the parallel bond strengths are, the more

parallel bonds between clumps are broken off. For the assembly with low parallel bond strength, the number of broken parallel bonds between clumps increases sharply. Similarly, the number of broken asperities increases with decreasing parallel bond strength and the number of asperities which break off rises sharply when the assembly approaches failure. This is due to large numbers of particles rotating when the assembly approaches failure and the angular corners and sharp asperities break off.



(a)



(b)

Figure 7.28. (a) Axial strain and (b) volumetric strain (contraction positive) against number of cycles.

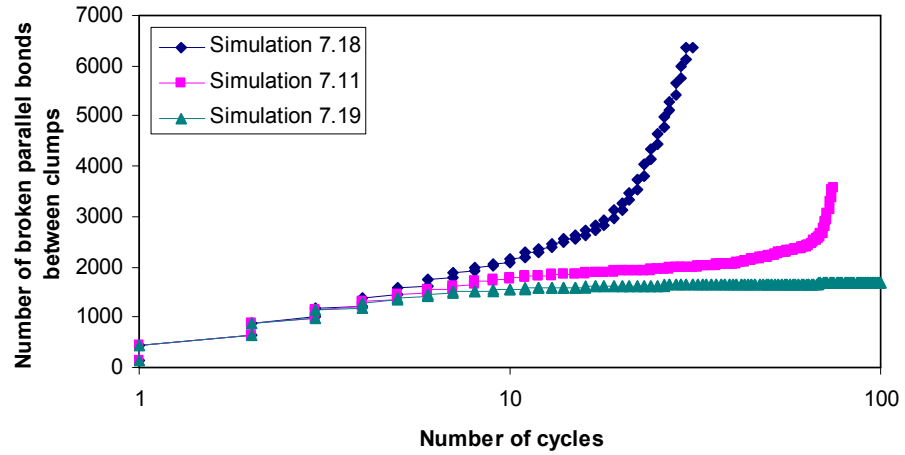


Figure 7.29. Number of broken parallel bonds between clumps against number of cycles.

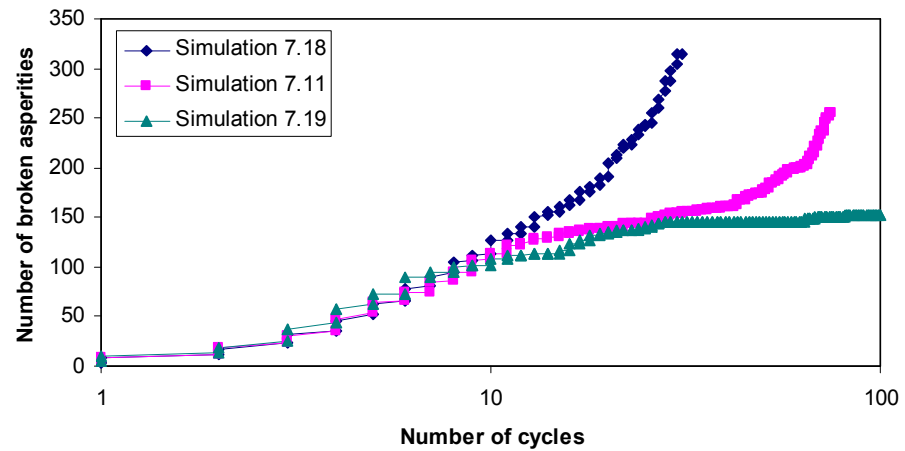


Figure 7.30. Number of broken asperities against number of cycles.

Figure 7.31 shows a plot of the number of broken parallel bonds between clumps for the assemblies with different parallel bond strengths against axial strain. It can be seen that the number of broken parallel bonds between clumps increases with increasing axial strain. As expected, fewer parallel bonds between clumps break at

the same level of axial strain, if the assembly stabilises rather than continues to failure.

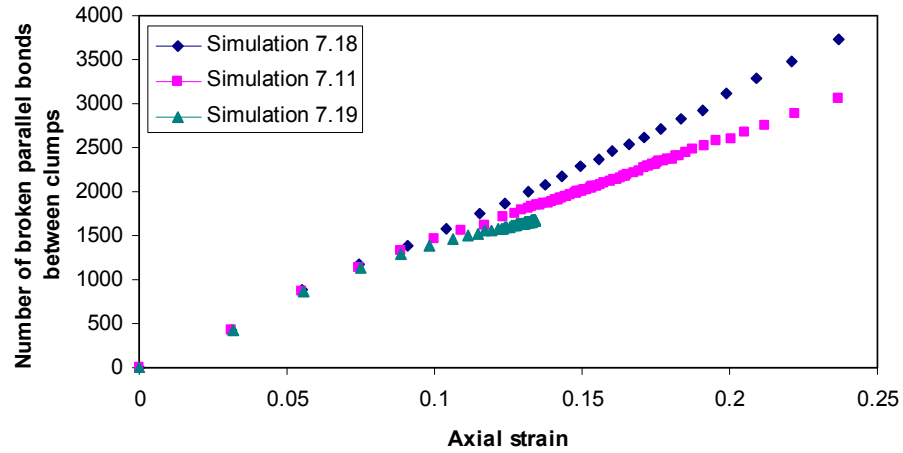


Figure 7.31. Number of broken parallel bonds between clumps against axial strain.

Particles rearrange towards stable positions under cyclic loading. For high parallel bond strength (providing high shear resistance at each contact between particles), after a number of cycles, the assembly stabilises and dilation stops. For the assembly with low parallel bond strength, the shear resistance at the contact is insufficient, particles keep sliding and rolling and the sample finally fails. The important finding here is that parallel bond strengths have an important effect on the mechanical behaviour of the assembly under cyclic loading. It affects the particle abrasion, the particle arrangement, and hence the stress-strain behaviour of the assembly.

7.6 Conclusions

The mechanical behaviour of an assembly of ten-ball triangular clumps, each bonded with eight small balls as asperities under cyclic triaxial loading conditions has been studied. The effect of particle abrasion under a confining pressure of 120 kPa has been investigated. It has been shown that particle abrasion affects both axial strain and volumetric strain, particularly under high maximum deviator stress and that ballast degradation under cyclic loading and permanent response of ballast can be simulated by modelling asperity abrasion. Crushable assemblies have been subjected to different cyclic loading conditions. The simulation results have been compared with the experimental results. The simulated assemblies stabilised within fewer cycles than the real ballast. Comparing with the experimental results, the permanent axial strain under different loading conditions was simulated effectively in the simulations using breakable assemblies. Higher dilation was observed in the simulations for assemblies with low confining pressure and high maximum deviator stress. As for the experimental data, the relationship between axial strain after 100 cycles and the ratio of maximum deviator stress for cyclic loading to the peak strength for static loading ψ is also confined within a narrow band in the simulations. The number of broken asperities under different loading conditions showed the same trend as the ballast breakage index in the experimental data. The degradation behaviour has been analysed at micro level. The number of broken asperities after 100 cycles can be determined, knowing values for any two of the following: axial strain, confining pressure or maximum deviator stress, since axial strain itself is a function of

confining pressure and maximum deviator stress. The effects of parallel bond strength between clumps have also been studied and it has been shown that the parallel bond strength between clumps affects particle abrasion (asperity breakage), particle arrangement and the stress-strain behaviour of the assembly. The main conclusion is therefore that the simulation results match well the experimental results over a large range of confining pressures and deviatoric stresses. The simulations are able to capture the behaviour of real ballast in terms of axial and volumetric strain and degradation under a range of confining pressures and cyclic deviator stresses.

CHAPTER 8

CONCLUSIONS AND SUGGESTIONS FOR FURTHER RESEARCH

8.1 Conclusions

Ballast particle shape plays a key role in the mechanical behaviour of railway ballast (e.g. stress-strain response and volumetric change behaviour). Modelling particle shape in a reasonable level is a key factor in discrete element modelling mechanical behaviour of railway ballast. Various particle shapes (e.g. sphere, irregular shaped clump, two-ball clump with two smaller spheres bonded, eight-ball cubic clump, ten-ball triangular clump and ten-ball triangular clump with eight smaller spheres bonded) have been investigated under various loading conditions. Under the same loading conditions and boundary conditions, particle shape plays a key role in determining the distribution and magnitudes of contact forces. Moreover, angular shaped particle provides interlocking and moment resistance. Particle shape, therefore, affects stress-strain response and volumetric change behaviour at macro level, and particle rolling, sliding and particle interlocking at micro level. Compared to other particle shapes, the ten-ball triangular clump with

eight smaller spheres bonded captures the main mechanical features effectively without increasing computational time significantly.

In order to model the correct response in terms of permanent deformation and volumetric strain, particle abrasion has been modelled in the simulations. According to the size of asperities, two types of particle abrasion have been modelled. Small-scale asperities which find their way into the voids and carry no load have been modelled by using weak parallel bonds; angular corners and projections have been modelled by bonding small balls to the clump.

Box test simulations have been carried out using spheres, irregular shaped clumps and two-ball clumps with two small spheres (asperities). The influence of particle shape on the heterogeneous stresses within an aggregate and on particle rotation and displacement has been investigated. The effect of particle breakage under cyclic loading has also been studied in the box test simulations.

Both monotonic and cyclic triaxial test simulations have been carried out. The effect of particle shape, interparticle friction and particle abrasion has been studied in the monotonic triaxial test simulations. The mechanical behaviour of railway ballast under monotonic loading with a range of confining pressures has been simulated using the ten-ball triangular clumps with eight smaller spheres bonded. The ten-ball triangular clumps with eight smaller spheres bonded have also been used in the cyclic triaxial test simulations with various loading conditions. The effect of particle abrasion (both parallel bond between clumps and asperity

breakage) on the mechanical behaviour of railway ballast under cyclic loading has been investigated.

The results of both monotonic and cyclic triaxial test simulations using the ten-ball triangular clumps with eight smaller spheres bonded have been compared with experimental results. For the monotonic triaxial test simulations, when the particle abrasion is modelled, the correct response of ballast in terms of shear stress and volumetric strain for a range of confining pressures can be obtained. The monotonic triaxial test simulations have shown that increasing the confining pressure does not sufficiently suppress the dilatancy without particle abrasion. However, when asperity breakage is simulated, the volumetric response under increasing confining stress is much more realistic. For the cyclic triaxial test simulations, the permanent axial strain and volumetric behaviour under different loading conditions has been simulated effectively in the simulations.

The effect of degradation of railway ballast has been studied using the breakable and unbreakable assembly in the box test simulations and both monotonic and cyclic triaxial test simulations. Asperity abrasion plays an important role in governing strength and volumetric strain under monotonic loading, and in permanent strains under cyclic loading. Particle abrasion leads to increasing number of contacts and decreasing mean contact force. Simulation results have been shown that modelling ballast degradation is important and necessary in the modelling mechanical behaviour of railway ballast.

8.2 Suggestions for Further Research

The simulations carried out in this research focus on simple shaped particles. Capturing the entire shape of real ballast particles in a discrete element model is a goal for further research. Under the same loading conditions and boundary conditions, particle shape determines the distribution and magnitudes of the contact forces, and therefore, it significantly affects particle crushing. In this research the size and location of asperities were arbitrarily fixed. However, it should be noted that the sizes and shapes of fragments from a natural ballast particle are determined by contact force distribution acting on the particle, the magnitudes of the contact forces and the distribution of flaws in the particle. Therefore, in further work, the particle model should also be able to capture more realistic particle fracture. Statistical variability in the bond strengths and the effect of fatigue (slow crack propagation) under repeated loading should be included by having more complex shapes with a larger number of bonded balls.

Since ballast is usually a reasonably uniformly graded material, the simulations carried out in this research assumed that the sample consisted of single sized particles. However, this approximation is aimed at reducing the complexity in the simulations and it may not represent entirely a real gradation of ballast. Therefore, future research could be aimed at investigating the effect of gradation on the stress-strain response and volumetric behaviour of a ballast assembly.

The contact mechanics between real ballast particles is not fully understood and experimental research may be a useful starting point. In this research, parallel

bonds and the linear contact stiffness model are used together to model the interaction of contacting ballast particles. Future research can study contact mechanics for real ballast particles and develop a more realistic and effective contact constitutive model in DEM.

For the clumps, when spheres overlap, the total volume of spheres in a clump is greater than the volume of the clump and the mass of the clump is therefore greater than the mass of an equivalent clump with a uniform density; such an entity is currently not available within PFC^{3D}. Where there is overlapping of spheres within a clump, there is a contribution to the mass in the overlapping region from each of the overlapping spheres. This also affects the inertia tensor of the clump since the mass is not uniformly distributed within the clump. A method which can produce clumps with uniform density and correct inertia tensor needs to be developed in the future.

The cylindrical wall was used to simulate a flexible membrane in the research. Although, it is possible to simulate a flexible membrane using a large number of bonded balls, this makes the computations much too time-consuming. Alternative methods should be developed in the future so that real flexible boundary conditions can be modelled.

REFERENCES

Allen, J. (1973). *The effect of non-constant lateral pressures of the resilient response of granular materials*. Ph.D. Thesis, University of Illinois at Urbana-Champaign, Urbana, Illinois.

Allen, J. J. and Thompson, M. R. (1974). Resilient response of granular materials subjected to time dependent lateral stresses. *Transp. Res. Rec.* **510**, Transportation Research Board, Washington, D.C., 1-13.

Alva-Hurtado, J. E. (1980). *A methodology to predict the elastic and inelastic behaviour of railroad ballast*. Ph.D. Thesis, University of Massachusetts, Amherst, Massachusetts.

Alva-Hurtado, J. E. and Selig, E. T. (1981). Permanent strain behaviour of railroad ballast. *Proceedings of the 10th International conference on soil mechanics and foundation engineering*, Stockholm, 543-546. Rotterdam: A. A. Balkema.

Aursudkij, B. (2007). *A Laboratory Study of Railway Ballast Behaviour under Traffic Loading and Tamping Maintenance*. Ph.D. Thesis, University of Nottingham, Nottingham, U.K.

Ashby, M. F. and Jones, D. R. H. (1980). *Engineering Materials 1*. Oxford: Pergamon Press.

Bardet, J. P. and Proubet, J. (1991). A numerical investigation of the structure of persistent shear bands in granular media. *Geotechnique* **41**, No. 4, 599-613.

Barksdale, R. D. (1972). Laboratory evaluation of rutting in basecourses materials. *Proceedings of the 3rd International Conference on Structure Design of Asphalt Pavements*, 161-174.

Barksdale, R. D. and Itani, S. Y. (1989). Influence of aggregate shape on base behaviour. *Transp. Res. Rec.* **1227**, Transportation Research Board, Washington, D.C., 173-182.

Barrett, P. J. (1980). The shape of rock particles, a critical review. *Sedimentology* **27**, 291-303.

Bathurst, R. J. and Rothenburg, L. (1990). Observations on stress-force-fabric relationships in idealized granular materials. *Mechanics of Materials* **9**, No. 1, 65-80.

Bishop, A. W. (1966), The strength of soils as engineering materials. *Geotechnique* **16**, No. 2, 91-128.

Boyce, J. R., Brown, S. F. and Pell, P. S. (1976). The resilient behaviour of a granular material under repeated loading. *Proceeding of the 8th ARRB Conference Material Construction and Maintenance*, Vol. 8, Part 3, 1-12.

British Standard: BS EN 13450 (2002). Aggregates for railway ballast.

Broadley, J. R., Johnston, G. D. and Pond, B. (1981). The dynamic impact factor. *Railway Engineering Conference*, Sydney, IEAust, Australia, 87-91.

Brown, S. F. (1996). Soil mechanics in pavement engineering. *Geotechnique* **46**, No. 3, 383-426.

Brown, S. F., Brodrick, B. V., Thom, N. H. and McDowell, G. R. (2007). The Nottingham Railway Test Facility. *Proceedings of the Institution of Civil Engineers: Transport* **160**, No. 2, 59-65.

Charles, J. A. and Watts, K. S. (1980). The influence of confining pressure on the shear strength of compacted rockfill. *Geotechnique* **30**, No. 4, 353-367.

Cheng, Y. P., Bolton, M. D. and Nakata, Y. (2004). Crushing and plastic deformation of soils simulated using DEM. *Geotechnique* **54**, No. 2, 131-141.

Cheng, Y. P., Nakata, Y. and Bolton, M. D. (2003). Discrete element simulation of crushable soil. *Geotechnique* **53**, No. 7, 633-641.

Collins, I. F. and Boulbibane, M. (2000). Geomechanical analysis of unbound pavements based on shakedown theory. *Journal of Geotechnical and Geoenvironmental Engineering* **126**, No. 1, 50-59.

Cui, L. and O'Sullivan, C. (2006). Exploring the macro- and micro-scale response of an idealised granular material in the direct shear apparatus. *Geotechnique* **56**, No. 7, 445-522.

Cundall, P. A. (1971). A computer model for simulating progressive large scale movements in blocky rock systems. *Proceedings of the Symposium of the International Society of Rock Mechanics*, Nancy, France, Vol. 1, Paper No. II-8.

Cundall, P. A. (1989). Numerical experiments on localization in frictional materials. *Ingenieur-Archiv* **59**, No. 2, 148-159.

Cundall, P. A., and Hart, R. D. (1992) Numerical Modelling of Discontinua. *Engineering Computations* **9**, No. 2, 100-113.

Cundall, P. A. and Strack, O. D. L. (1979). A discrete numerical model for granular assemblies. *Geotechnique* **29**, No. 1, 47-65.

Eisenmann, J., Leykauf, G. and Mattner, L. (1994). Recent development in German railway track design. *Proceedings of the Institution of Civil Engineers: Transport* **105**, No. 2, 91-96.

Favier, J. F., Abbaspour-Fard, M. H., Kremmer, M. and Raji, A. O. (1999). Shape representation of axi-symmetrical, non-spherical particles in discrete element simulation using multi-element model particles. *Engineering Computations* **16**, No. 4, 467-480.

Favier, J. F., Abbaspour-Fard, M. H. and Kremmer, M. (2001). Modelling nonspherical particles using multisphere discrete elements. *Journal of Engineering Mechanics* **127**, No. 10, 971-977.

Frossard, E. (1979). Effect of sand grain shape on interparticle friction: indirect measurements by Rowe's stress dilatancy theory. *Geotechnique* **29**, No. 3, 341-350.

Frederick, C. O. and Round, D. J. (1985). Vertical track loading Track technology for the next decade. *Vehicle system Dynamics Journal – Special Supplement*, No. 24, 222-233.

Fukushima, S and Tatsuoka, F. (1984). Strength and deformation characteristics of saturated sand at extremely low pressures, *Soils and Foundations* **24**, No. 4, 30-48.

Hardin, B. O. (1985). Crushing of soil particles. *Journal of soil mechanics and foundation division, ASCE* **111**, No. 10, 1177-1192.

Harireche, O. and McDowell, G. R. (2003). Discrete element modelling of cyclic loading of crushable aggregates. *Granular Matter* **5**, No. 3, 147-151.

Hicks, R. G. (1970). *Factors influencing resilient response of granular materials*. Ph.D. Thesis, University of California, Berkeley, California.

Hicks, R. G. and Monismith, C. L. (1971). Factors influencing the resilient properties of granular materials. *Hwy. Res. Rec.* **345**, 15-31.

Hossain, Z., Indraratna, B., Darve, F. and Thakur, P. K. (2007). DEM analysis of angular ballast breakage under cyclic loading. *Geomechanics and Geoengineering: An International Journal* **2**, No. 3, 175-181.

Indraratna, B., Ionescu, D. and Christie, H. D. (1998). Shear behaviour of railway ballast based on large-scale triaxial tests. *Journal of Geotechnical and Geoenvironmental Engineering, ASCE* **124**, No. 5, 439-449.

Indraratna, B., Khabbaz, H. and Salim, W. (2004). Ballast-formation-track interaction mechanism based on large-scale laboratory testing. *Conference on Railway Engineering (CORE 2004)*, Darwin, pp. 30.1-30.12.

Indraratna, B., Lackenby, J. and Christie, D. (2005). Effect of confining pressure on the degradation of ballast under cyclic loading. *Geotechnique* **55**, No. 4, 325-328.

Itasca, (1999). *Particle Flow Code in Three Dimensions*. Itasca Consulting Group, Inc., Minnesota.

Iwashita, K. and Oda, M. (1998). Rolling resistance at contacts in the simulation of shear band development by DEM. *Journal of Engineering Mechanics, ASCE* **124**, No. 3, 285-292.

Jaeger, J. C. (1967). Failure of rocks under tensile conditions. *International Journal of Rock and Mining Science* **4**, 219-227.

Janardhanam, R. and Desai, C. S. (1983). Three-dimensional testing and modelling of ballast. *Journal of Geotechnical Engineering, ASCE* **109**, No. 6, 783-796.

Jeffs, T. and Marich, S. (1987). Ballast characteristics in the laboratory. *Conference on railway engineering*, September, Perth, 141-147.

Knutson, R. M. (1976). *Factors influencing the repeated load behaviour of railway ballast*. Ph.D. Thesis, University of Illinois, Urbana, Illinois.

Kolisoja, P. (1997). *Resilient behaviour of granular materials for analysis of highway pavements*. Ph.D. Thesis, University of Nottingham, Nottingham, U.K.

Lade, P. V., Yamamuro, J. A. and Bopp, P. A. (1996). Significance of particle crushing in granular materials. *Journal of Geotechnical Engineering, ASCE* **122**, No. 4, 309-316.

Lackenby, J., Indraratna, B., McDowell, R. G. and Christie, D. (2007). Effect of confining pressure on ballast degradation and deformation under cyclic triaxial loading. *Geotechnique* **57**, No. 6, 527-536.

Lee, D. M. (1992). *The angles of friction of granular fills*. Ph.D. Thesis, University of Cambridge, U.K.

Lekara, F. (1997). *Permanent deformation behaviour of unbound granular materials*. Licentiate Thesis, Royal Institute of Technology, Stockholm.

Lekarp, F. and Dawson, A. (1998). Modelling permanent deformation behaviour of unbound granular materials. *Construction and Building Materials* **12**, No. 1, 9-18.

Lekarp, F., Isacsson, U. and Dawson, A. (2000a). State of the art. I: Resilient response of unbound aggregates. *Journal of Transportation Engineering, ASCE* **126**, No. 1, 66-75.

Lekarp, F., Isacsson, U. and Dawson, A. (2000b). State of the art. II: Permanent strain response of unbound aggregates. *Journal of Transportation Engineering, ASCE* **126**, No. 1, 76-83.

Lim, W. L. (2004). *Mechanics of Railway Ballast Behaviour*. Ph.D. Thesis, University of Nottingham, Nottingham, U.K.

Lim, W. L. and McDowell, G. R. (2005). Discrete element modelling of railway ballast. *Granular Matter* **7**, No. 1, 19-29.

Lim, W. L., McDowell, G. R. and Collop, A. C. (2004). The application of Weibull statistics to the strength of railway ballast. *Granular Matter* **6**, No. 4, 229-237.

Lin, X. and Ng, T.-T. (1997). A three-dimensional discrete element model using arrays of ellipsoids. *Geotechnique* **48**, No. 2, 319-329.

Liu, S. and Matsuoka, H. (2003). Microscopic interpretation on a Stress-dilatancy relationship of granular materials. *Soils and Foundations* **43**, No. 3, 73-84.

Lu, M. and McDowell, G. R. (2006). Discrete element modelling of ballast abrasion. *Geotechnique* **56**, No. 9, 651-656.

Lu, M. and McDowell, G. R. (2007). The importance of modelling ballast particle shape in DEM. *Granular Matter* **9**, No. 1, 69-80.

Lobo-Guerrero, S. and Vallejo, L. E. (2005). Crushing a weak granular material: experimental numerical analyses. *Geotechnique* **55**, No. 3, 243-249.

Lobo-Guerrero, S. and Vallejo, L. E. (2006). Discrete element method analysis of Railtrack ballast degradation during cyclic loading. *Granular Matter* **8**, No. 3-4, 195-204.

Luong, M. P. (1982). Mechanical aspects and thermal effects of cohesionless soils under cyclic and transient loading. *Deformation and Failure of Granular Materials, International Union of Theoretical and Applied Mechanics Symposium*. Delft, Netherlands, 239-246. Rotterdam: A. A. Balkema.

Marachi, N. D., Chan, C. K. and Seed, H. B. (1972). Evaluation of properties of rockfill materials. *Journal of the Soil Mechanics and Foundations, ASCE* **98**, 95-114.

Marsal, R. J. (1967). Large scale testing of rockfill materials. *Journal of Soil Mechanics and Foundations, ASCE* **93**, No. SM2, 27-43.

Marsal, R. J. (1973). Mechanical properties of rockfill. *Embankment Dam Engineering*, 109-200. New York: Wiley.

McDowell, G. R. (2002). On the yielding and plastic compression of sand. *Soils and Foundations* **42**, No. 1, 139-145.

McDowell, G. R. and Amon, A. (2000). The application of Weibull statistics to the fracture of soil particles. *Soils and Foundations* **40**, No. 5, 133-141.

McDowell, G. R. and Bolton, M. D. (1998). On the micro mechanics of crushable aggregates. *Geotechnique* **48**, No. 5, 667-679.

McDowell, G. R., Bolton, M. D. and Robertson, D. (1996). The fractal crushing of granular materials, *Journal of Mechanics and Physics of Solids* **44**, No. 12, 2079-2102.

McDowell, G. R. and Harireche, O. (2002a). Discrete element modelling of soil particle fracture. *Geotechnique* **52**, No. 2, 131-135.

McDowell, G. R. and Harireche, O. (2002b). Discrete element modelling of yielding and normal compression of sand. *Geotechnique* **52**, No. 4, 299-304.

McDowell, G. R., Harireche, O., Konietzky, H., Brown, S. F. and Thom, N. H. (2006). Discrete element modelling of geogrid-reinforced aggregates. *Proceedings of the Institution of Civil Engineers: Geotechnical Engineering* **159**, No. GE1, 35-48.

McDowell, G. R., Lim, W. L. and Collop, A. C. (2003). Measuring the strength of railway ballast. *Ground Engineering* **36**, No. 1, 25-28.

McDowell, G. R., Lim, W. L., Collop, A. C., Armitage, R. and Thom, N. H. (2005). Laboratory simulation of train loading and tamping on ballast. *Proceedings of the Institution of Civil Engineers: Transport* **158**, No. TR2, 89-95.

Mitchell, J. K. (1993). *Fundamentals of Soil Behaviour*. Wiley, New York.

Moore, W. M., Britton, S. C. and Schrivner, F. H. (1970). *A laboratory study of the relation of stress to strain for a crushed limestone base material*. Res. Rep. 99-

5F, Study 2-8-65-99, Texas Transp. Inst., Texas A&M University, College Station, Texas.

Morgan, J. R. (1966). The response of granular materials to repeated loading. *Proceedings of the 3rd ARRB Conference*, 1178-1192.

Nakata, Y., Hyde, A. F. L., Hyodo, M. and H. Murata, (1999). A probabilistic approach to sand particle crushing in the triaxial test. *Geotechnique* **49**, No. 5, 567-583.

Nakata, Y., Kato, Y., Hyodo, M., Hyde, A. F. L. and Murata, H. (2001). One-dimensional compression behaviour of uniformly graded sand related to single particle crushing strength. *Soils and Foundations* **41**, No. 2, 39-51.

Ng, T.-T. (2001). Fabric evolution of ellipsoidal arrays with different particle shapes. *Journal of Engineering Mechanics, ASCE* **127**, No. 10, 994-999.

Ng, T.-T. and Dobry, R. (1992). A non-linear numerical model for soil mechanics. *International Journal for Numerical and Analytical Methods in Geomechanics* **16**, 247-263.

Ng, T.-T. and Dobry, R. (1994). Numerical simulations of monotonic and cycled loading of granular soil. *Journal of Geotechnical Engineering, ASCE* **120**, No. 2, 388-403.

Ni, Q. (2003) *Effects of particle properties and boundary conditions on soil shear behaviour: 3-D numerical simulations*. Ph.D. Thesis, University of Southampton, Southampton, U.K.

Ni, Q., Powrie, W., Zhang, X. and Harkness, R. (2000). Effect of particle properties on soil behaviour: 3-D numerical modelling of shearbox tests. *Geotechnical Special Publication, Vol. 96, Reston, VA. ASCE*, 58-70.

Norman, G. M. and Selig, E. T. (1983). Ballast performance evaluation with box test. *AREA*, Bul. 692, Proceedings Vol. 84, 207-239.

O'Reilly, M. P. and Brown, S. F. (1991). *Cyclic loading of soils: from theory to design*, Glasgow: Blackie and Son Ltd.

O'Sullivan, C. and Bray, J. D. (2003). Relating the response of idealized analogue particles and real sands, *Numerical Modeling in Micromechanics via Particle Methods* (ed. H. Konietzky), 157-164. Rotterdam: A. A. Balkema.

Olowokere, D. O. (1975). *Strength and deformation of railway ballast subject to triaxial loading*, M.Sc. Dissertation, Queen's University, Kingston, Ontario, Canada.

Oda, M. and Iwashita, K. (1999). *Mechanics of granular materials, an introduction*. Rotterdam: A. A. Balkema.

Oda, M. and Kazama, H. (1998). Micro-structure of shear band and its relation to the mechanism of dilatancy and failure of granular soils. *Geotechnique* **48**, No. 1, 1-17.

Oda, M., Nemat-Nasser, S. and Konishi, J. (1985). Stress-induced anisotropy in granular masses. *Soils and Foundations* **25**, No.3, 85-97.

Ponce, M. and Bell, J. M. (1971). Shear strength of sand at extremely low pressures. *Journal of the Soil Mechanics and Foundations, ASCE* **97**, No. 4, 625-638.

Powrie, W. (2004). *Soil Mechanics: concepts and applications*. London: Spon Press.

Powrie, W., Ni, Q., Harkness, R. M. and Zhang, X. (2005). Numerical modelling of plane strain tests on sands using a particulate approach. *Geotechnique* **55**, No. 4, 297-306.

Rada, G. and Witczak, M. W. (1981). Comprehensive evaluation of laboratory resilient moduli results for granular material. *Transp. Res. Rec.* **810**, Transportation Research Board, Washington, D.C., 23-33.

Railtrack Line Specification (2000). RT/CE/S/006 issue 3, *Track Ballast*, London.

Raymond, G. P. and Davies, J. R. (1978). Triaxial tests on dolomite railroad ballast. *Journal of the Geotechnical Engineering, ASCE* **104**, No. 6, 737-751.

Raymond, G. P. and Diyaljee, V. A. (1979). Railroad Ballast Load Ranking Classification. *Journal of the Geotechnical Engineering, ASCE* **105**, No. 10, 1133-1153.

Robertson, D. (2000). *Numerical simulations of crushable aggregates*. Ph.D. Thesis, University of Cambridge, Cambridge, U.K.

Robinson, R. G. (1974). Measurement of the elastic properties of granular materials using a resonance method. *TRRL Supplementary Rep. No. 111UC*, TTRL.

Roner, C. J. (1985). *Some effects of shape, gradation and size on the performance of railroad ballast*. M.Sc. Degree project report, Report No. AAR85-324P, Department of Civil Engineering, University of Massachusetts, Amherst, Massachusetts.

Rothenburg, L. and Bathurst, R. J. (1992). Micromechanical features of granular assemblies with planar elliptical particles. *Geotechnique* **42**, No. 1, 79-95.

Seed, H. B., Chan, C. K. and Lee, C. E. (1962). Resilience characteristics subgrade soils and their relation to fatigue failures. *Proceedings of International Conference on Structural Design of Asphalt Pavements*, Ann Arbor, Michigan, 611-636.

Seed, H. B., Mitry, F. G., Monismith, C. L. and Chan, C. K. (1965). *Predictions of Pavement Deflection from Laboratory Repeated Load Tests*. Report No. TE-65-6, Soil Mechanics and Bituminous Material Research Laboratory, University of California, Berkeley, California.

Selig, E. T. and Waters, J. M. (1994). *Track geotechnology and substructure management*. London: Thomas Telford.

Shenton, M. J. (1974). *Deformation of railway ballast under repeated loading conditions*. British Railways Research and Development Division, Derby. U.K.

Skinner, A. E. (1969). A note on the influence of interparticle friction on the shearing strength of a random assembly of spherical particles. *Geotechnique* **19**, No. 1, 150-157.

Stewart, H. E. and Selig, E. T. (1984). Correlation of concrete tie track performance in revenue service and at the facility for accelerated service testing, *US Fed Railroad Adm. Off. Res. Dev. Rep. FRA ORD*, 131.

Suiker, A. S. J. and Fleck, N. A. (2004). Frictional collapse of granular assemblies. *Journal of Applied Mechanics* **71**, No. 3, 350-358.

Suiker, A. S. J., Selig, E. T. and Frenkel, R. (2005). Static and cyclic triaxial testing of ballast and subballast. *Journal of Geotechnical and Geoenvironmental Engineering* **131**, No. 6, 771-782.

Sweere, G. T. H. (1990). *Unbound granular bases for roads*. Ph.D. Thesis, Delft University of Technology, Holland.

Thom, N. H. (1988). *Design of road foundations*. Ph.D. Thesis, University of Nottingham, Nottingham, U.K.

Thom, N. H. and Brown, S. F. (1988). The effect of grading and density on the mechanical properties of a crushed dolomitic limestone. *Proceedings of the 14th ARRB Conference*, Vol. 14, Part 7, 94-100.

Thom, N. H. and Brown, S. F. (1989). The mechanical properties of unbound aggregates from various sources. *Unbound Aggregates in Roads*, (eds. R. H. Jones, and A. R. Dawson), 130-142. London: Butterworth.

Thomas, P. (1997). *Discontinuous deformation analysis of particulate media*. Ph.D. Thesis. University of California, Berkeley, California.

Thomas, P. A. and Bray, J. D. (1999). Capturing nonspherical shape of granular media with disk clusters. *Journal of Geotechnical and Geoenvironmental Engineering* **125**, No. 3, 169-178.

Thornton, C. (2000). Numerical simulations of deviatoric shear deformation of granular media. *Geotechnique* **50**, No. 1, 43-53.

Thompson, M. R. (1989). *Factors affecting the resilient moduli of soil and granular materials*, Rep. No. FHWA-TS-90-031, National Technical Information Service, Springfield, Va, pp. 15.

Ting, J. M., Corkum, B. T., Kauffman, C. R., and Greco, C. (1989). Discrete numerical model for soil mechanics. *Journal of Geotechnical Engineering, ASCE* **115**, No. 3, 379-398.

Trollope, E. H., Lee, I. K. and Morris, J. (1962). Stresses and deformation in two-layer pavement structures under slow repeated loading. *Proceedings of the ARRB conference*, Vol. 1, Part 2, 693-718.

Ueng, T. S. and Chen, T.-J. (2000). Energy aspects of particle breakage in drained shear of sands. *Geotechnique* **50**, No. 1, 65-72.

Vesic, A. S. and Clough, G. W. (1968). Behaviour of granular materials under high stresses. *Journal of Soil Mechanics and Foundations, ASCE* **94**, No. SM3, 661-688.

Vu-Quoc, L., Zhang, X. and Walton, O. R. (2000). A 3-D discrete-element method for dry granular flows of ellipsoidal particles. *Computer Methods in Applied Mechanics and Engineering* **187**, 482-528.

Weibull, W. (1951). A statistical distribution function of wide applicability. *Journal of Applied Mechanics* **19**, 293-297.

Zhang, X. and Vu-Quoc, L. (2000). Simulation of chute flow of soybeans using an improved tangential force-displacement model. *Mechanics of Materials* **32**, No. 2, 115-129.

APPENDIX

The Numerical Servo-control Mechanism

A servo-control algorithm was developed to achieve stress-controlled loading (Itasca, 1999). A wall velocity is adjusted to minimize the difference between the measured stress and target stress. The velocity of a wall $\dot{u}^{(w)}$ was calculated from a function of the measured stress $\sigma^{measured}$, the required stress $\sigma^{required}$ and a “gain” factor G , as follows:

$$\dot{u}^{(w)} = G(\sigma^{measured} - \sigma^{required}) = G\Delta\sigma \quad (\text{A.1})$$

The maximum increment in wall force arising from the movement of wall in one timestep can be calculated by

$$\Delta F^{(w)} = k_n^{(w)} N_c \dot{u}^{(w)} \Delta t \quad (\text{A.2})$$

where $\Delta F^{(w)}$ is the change in force on the wall, N_c is the number of contacts on the wall, and $k_n^{(w)}$ is the average stiffness of these contacts. Thus, the change in mean wall stress, $\Delta\sigma^{(w)}$, is computed by

$$\Delta\sigma^{(w)} = \frac{k_n^{(w)} N_c \dot{u}^{(w)} \Delta t}{A^{(w)}} \quad (\text{A.3})$$

where $A^{(w)}$ is the area of the wall.

For stability, the absolute value of the change in wall stress must be less than the absolute value of the difference between the measured stresses and required stresses. Therefore, a relaxation factor α ($\alpha < 1$) is applied and the stability requirement becomes

$$|\Delta\sigma^{(w)}| < \alpha|\Delta\sigma| \quad (\text{A.4})$$

Substituting Equations A.1 and A.3 into Equation A.4 gives

$$\frac{k_n^{(w)} N_c \dot{u}^{(w)} \Delta t}{A^{(w)}} < \alpha|\Delta\sigma| \quad (\text{A.5})$$

and the “gain” factor can be calculated by

$$G = \frac{\alpha A^{(w)}}{k_n^{(w)} N_c \Delta t} \quad (\text{A.6})$$

Therefore, by updating the velocity of a wall in each timestep using Equation A.1, the required stress can be achieved.